Doctoral Dissertation
Doctoral Program in Electrical, Electronics and Communications Engineering
(32.th cycle)

Multiphysics modelling of high-speed optoelectronic devices for silicon photonics platforms

Andrea Palmieri
* * * * * *

Supervisors
Michele Goano, Supervisor
Francesco Bertazzi, Co-supervisor

Politecnico di Torino
February 29, 2020

I hereby declare that, the contents and organisation of this dissertation constitute my own original work and does not compromise in any way the rights of third parties, including those relating to the security of personal data.

. . . . . .

Andrea Palmieri

Turin, February 29, 2020

Summary

In the present zettabyte era, the increasingly growing amount and quality of services provided to a worldwide audience leads to an incessant demand of computational resources for processing and transporting information. Already consolidated in both datacom and telecom contexts, on-chip optical communications are the Holy Grail towards Tbit/s transmission rates with negligible energy consumption. In a framework where scaling and integration are still the most sensitive terms silicon photonics appears as the most natural technological platform to realize low-cost and CMOS-compatible integration of electrical and optical systems.

Specifically, silicon photonics addresses the study and the technological applications of silicon and other group-IV semiconductors as optical medium for generation, transmission, modulation and detection of light.

The cost of production for the integrated circuits makes unfeasible a trial-and-error approach for the development of new devices. In fact, simulation-driven design has become a standard in the industry: it is a low-cost solution capable to provide insights on the inner workings of our device (i.e. carrier densities, electric field distribution). Thanks to such numerical insights new directions and choices can be swiftly explored in the design of the next semiconductor product.

In order to have a quantitative comparison against experimental measurements and/or other theoretical approaches, we require from our model to be an accurate depiction of the physical situation. All this should come at the cost of a reasonable amount of resources (i.e. execution time, RAM).

Drift-diffusion models and Monte Carlo techniques applied to the Boltzmann transport equation (BTE) are the standard approaches in semiconductor modelling. In the drift-diffusion model, the motion of our carriers is described as the sum of two component: a *drift* term describing the electrical current produced by the electrostatic potential $\phi(x)$ and a *diffusion* term proportional to the gradient of concentration of electrons and holes $n(x), p(x)$. Poisson's equation and charge continuity close the drift-diffusion model leading to an effective description of the physics in the semiconductor device based on differential equations. Even more challenging is the solution of multiphysics problems where two or more physical domains interact and must be solved selfconsistently. Consider the case of a photodetector: finite-difference time domain (FDTD) algorithms are employed to solve

Maxwell's equation from the illumination source up to the absorbing region of the detector; the presence of space dependent optical generation profile $G_{opt}(x, y, z)$ will produce a perturbation on the carrier distributions $n(x, y, z)$, $p(x, y, z)$ inducing a variation of refractive index seen by the optical problem. A self-consistent approach is mandatory in this case, unless we can ignore the eventual "feedback" mechanisms on the basis of experimental evidences or theorical proofs simplifying the solution of the multiphysics problem. In such a context, electro-optical simulations of high-speed waveguide-coupled detectors and optical modulators have been performed and presented in this work:

- in the first chapter, we introduce a few concepts on what is silicon photonics and what it can offer in terms of convergence between electrical and optical sub-systems. A brief introduction over two fundamental components of silicon photonics, photodetectors and optical modulators, is given.

- in the second chapter, we describe what a waveguide-coupled photodetector is and how it compares to vertically-illuminated ones. After a short excursus of the technological and technical achievements within scientific literature, results on the coupled optical and electrical simulation are presented. In particular, a more refined description of the Si/Ge heterointerface and a coupled electrooptical simulation of a pin photodetector illuminated using a lateral asymmetric waveguide are presented. On one hand, we discovered the introduction of a thin graded $Si_{1-x}Ge_x$ region to be fundamental to attain good agreement between simulations and experimental results of n-on-p photodetectors; on the other hand, multiphysics simulations confirm the advantage of lateral illumination with respect to butt-coupling solutions when exposed to high-level input optical power.

- in the third chapter, we focus on plasmonic-organic hybrid modulators detailing their advantages over standard implementations. Following a review of the available experimental results and numerical simulations, we present some results on the modelling of plasmonic modulators using commercial electromagnetic solvers. Specifically, simulations of plasmonic slot waveguides loaded with a linear electro-optic polymer and of a plasmonic Mach-Zehnder modulator have been performed. A parametric study of the slot waveguide's dimensions through a finite element method (FEM) modal solver gave us the possibility to leverage semi-analytical models that simplified the design of the Mach-Zehnder modulator. Such design was then validated by means of more complete numerical approaches such as finite difference time-domain (FDTD) or eigenmode expansion (EME).

List of publications

Journal papers

[**1**] M. Vallone, M. Goano, F. Bertazzi, G. Ghione, A. Palmieri, S. Hanna, D. Eich, H. Figgemeier, "Reducing inter-pixel crosstalk in HgCdTe detectors", *Optical and Quantum Electronics*, vol. 52, pp. 25, 2020, doi: 10.1007/s11082-019-2137-9.

[**2**] Y. Sharabani, A. Palmieri, A. Kyrtsos, M. Matsubara, E. Bellotti "Interfacial Charge Dynamics in Metal-Oxide-Semiconductor Structures: The Effect of Deep Traps and Acceptor Levels in GaN", *Physical Review Applied*, vol. 13, pp. 014007, 2020, doi: 10.1103/PhysRevApplied.13.014007.

[**3**] A. Palmieri, M. Vallone, M. Calciati, A. Tibaldi, F. Bertazzi, G. Ghione, M. Goano, "Heterostructure modeling considerations for Ge-on-Si waveguide photodetectors", *Optical and Quantum Electronics*, vol. 50, pp. 71, 2020, doi: 10.1007/s11082-018-1338-y.

[**4**] M. Vallone, A. Palmieri, M. Calciati, F. Bertazzi, F. Cappelluti, G. Ghione, M. Goano, M. Bahl, R. Scarmozzino, S. Hanna, D. Eich, H. Figgermeier, "Non-Monochromatic 3D Optical Simulation of HgCdTe Focal Plane Arrays", *Journal of Electronic Materials*, vol. 50, pp. 5742-5751, 2017, doi: 10.1007/s11664-018-6424-1.

Conference proceedings

[**1**] A. Tibaldi, M. Ghomashi, F. Bertazzi, M. Vallone, A. Palmieri, M. Goano, G. Ghione, "Modeling of plasmonic organic hybrid E/O modulators: towards a comprehensive 3D simulation framework", submitted to the *European Conference on Integrated Optics (ECIO)*, Paris, 2020.

[**2**] A. Palmieri, A. Shafiee, M. G. C. Alasio, A. Tibaldi, G. Ghione, F. Bertazzi, M. Goano, M. Vallone, "Enhanced dynamic properties of Ge-on-Si mode-evolution waveguide photodetectors", submitted to the *International Conference on Numerical Simulation of Optoelectronic Devices (NUSOD)*, Turin, 2020.

[**3**] M. Vallone, M. Goano, F. Bertazzi, G. Ghione, A. Palmieri, S. Hanna, D. Eich,

H. Figgemeier, "Reducing inter-pixel crosstalk in HgCdTe detectors", *Proceedings of the International Conference on Numerical Simulation of Optoelectronic Devices (NUSOD)*, pp. 83-84, 2019, doi: 10.1109/NUSOD.2019.8806849.

[**4**] M. Calciati, A. Tibaldi, C. D. Santi, A. Palmieri, L. Avataneo, M. Meneghini, F. Bertazzi, F. Cappelluti, M. Vallone, G. Ghione, G. Meneghesso, E. Zanoni, M. Goano, "Enhanced semiclassical simulation of InGaN/GaN multi-quantum-well solar cells", *Proceedings of the International Conference on Numerical Simulation of Optoelectronic Devices (NUSOD)*, pp. 93-94, 2019, doi: 10.1109/NUSOD.2019.8806934.

[**5**] A. Palmieri, M. Vallone, M. Calciati, F. Bertazzi, M. Goano, G. Ghione, "Effect of Saturation Velocity in Germanium p-i-n Photodetectors", *19th Italian National Conference on Photonic Technologies (Fotonica 2017)*, 2017, doi: 10.1049/cp.2017.0190.

[**6**] A. Palmieri, M. Calciati, M. Vallone, G. Ghione, A. Tibaldi, F. Bertazzi, M. Goano, "Energy balance modeling of Ge-on-Si waveguide avalanche photodetectors", *Proceedings of the International Conference on Numerical Simulation of Optoelectronic Devices (NUSOD)*, pp. 211-212, 2017, doi: 10.1109/NUSOD.2017.8010066.

[**7**] M. Vallone, A. Palmieri, M. Calciati, F. Bertazzi, F. Cappelluti, G. Ghione, M. Goano, S. Hanna, D. Eich, H. Figgemeier, R. Scarmozzino, E. Heller, M. Bahl, "Broadband 3D optical modeling of HgCdTe infrared focal plane arrays", *Proceedings of the International Conference on Numerical Simulation of Optoelectronic Devices (NUSOD)*, pp. 205-206, 2017, doi: 10.1109/NUSOD.2017.8010063.

[**8**] M. Vallone, A. Palmieri, M. Calciati, F. Bertazzi, M. Goano, G. Ghione, F. Forghieri, "3D physics-based modelling of Ge-on-Si waveguide p-i-n photodetectors", *Proceedings of the International Conference on Numerical Simulation of Optoelectronic Devices (NUSOD)*, pp. 207-208, 2017, doi: 10.1109/NUSOD.2017.8010064.

Book chapters

[**1**] M. Vallone, F. Bertazzi, A. Tibaldi, A. Palmieri, G. Ghione, M. Goano, S. Hanna, D. Eich, and H. Figgemeier, "Next-generation long-wavelength infrared detector arrays: competing technologies and modeling challenges", to appear in *Integrated optics: recent advances and prospects*, M. Ferrari, Institution of Engineering and Technology (IET), 2020.

Be prepared

Sir Robert Baden-Powell of Gilwell

Contents

1 Notions on silicon photonics 1
- 1.1 Why silicon photonics? . . . 1
- 1.2 Components for silicon photonics . . . 4
  - 1.2.1 Waveguide-coupled photodetectors . . . 4
  - 1.2.2 Modulators . . . 5
- 1.3 Trends and perspectives . . . 6

2 Waveguide-coupled photodetectors 11
- 2.1 Fundamentals . . . 11
- 2.2 Review of the state of the art . . . 14
- 2.3 Novel contributions . . . 30
  - 2.3.1 Review of the material parameters . . . 32
  - 2.3.2 Effects of saturation velocity . . . 33
  - 2.3.3 Realistic description of the Si/Ge heterostructure . . . 35
  - 2.3.4 Drift-diffusion vs. energy balance transport . . . 38
  - 2.3.5 Innovative optical coupling . . . 44
- 2.4 Conclusions . . . 49

3 Electro-optic plasmonic-organic hybrid modulators 51
- 3.1 Basic concepts . . . 51
- 3.2 Review of the state of the art . . . 53
- 3.3 Numerical modelling of plasmonic modulators . . . 81
  - 3.3.1 Investigation of the plasmonic slot waveguides through modal solver . . . 82
  - 3.3.2 Design of a plasmonic Mach-Zehnder modulator . . . 86
- 3.4 Conclusions . . . 90

A Modelling of the electron transport 91
- A.1 Drift-diffusion equations . . . 91
  - A.1.1 Derivation of the transport model . . . 91
  - A.1.2 Physical models . . . 93
- A.2 Multiphysics coupling between optical and transport solver . . . 95

Bibliography 97

Chapter 1

Notions on silicon photonics

In this chapter, silicon photonics is presented as the most natural technological platform to realize low-cost and CMOS-compatible integration of electrical and optical systems in a time where scaling and integration are of the utmost importance. Together with a brief introduction on essential components for the design of photonic integrated circuits, we report on some new research directions.

1.1 Why silicon photonics?

The unstoppable bandwidth demand is a consequence of the incessant growth of social media, high-quality streaming, VoIP, cloud computing, analytics and many other services, provided to a worldwide audience. All of this is possible thanks to the presence of large- to hyper-scale datacenters composing the backbone of the Internet. According to the Cisco Global Cloud Index report (updated in November 2018) [30], datacenters will see a strong evolution in their dimensions and their traffic topping 21 ZB in 2021. Of the whole projected traffic, 75 % is located to the internal premises of the data center due to the internal traffic (i.e. authentication services, data storage, hardware virtualization). On an economical level, it implies that major savings may come from the adoption of low cost and low power interconnects.

While copper cables still provide a cost-effective solution for intra-rack communications, for data rates higher than 25 Gbit/s and distances of several tens of meters the electrical signal can experience high propagation losses. Optical links can replace traditional solutions thanks to their potential reduction in energy consumption while maximizing bandwidth and reliability, in this context, one of the bottlenecks is the lack of an effective integration strategy between optical and electrical sub-systems. In Fig. 1.1, a notable example of the monolithic integration between the electronic and the optic circuits has been reported by a collaboration between MIT, University of California and University of Colorado [6]. Using a

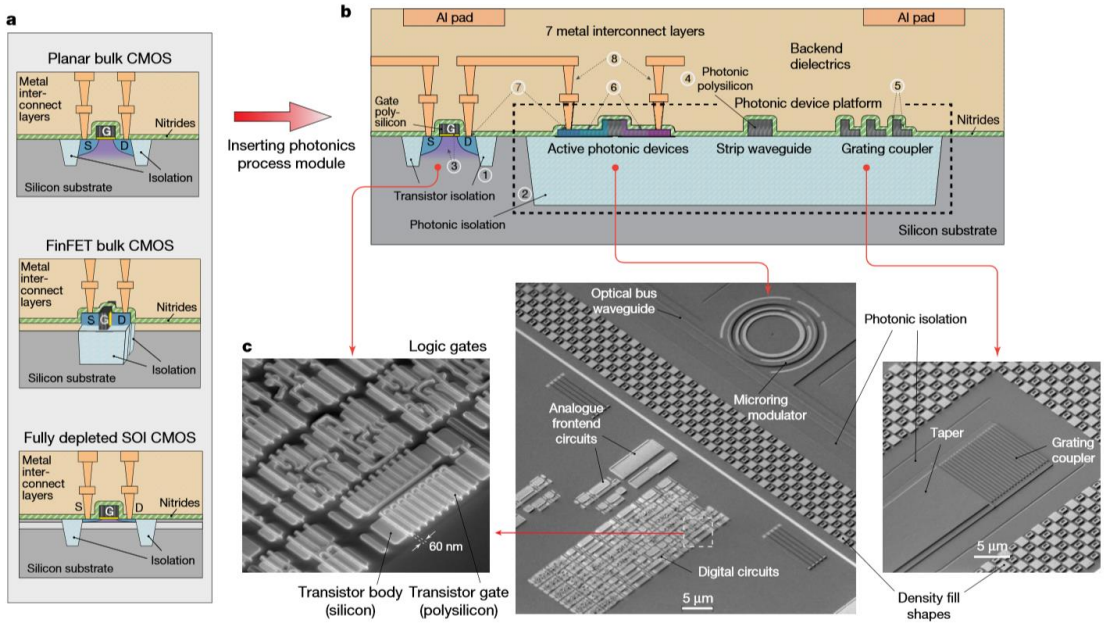

Figure 1.1: (a) Illustration of three major deeply scaled CMOS processes: planar bulk CMOS, FinFET bulk CMOS, and fully depleted SOI CMOS. (b) Integration of a photonics process module into planar bulk CMOS with photonic devices implemented in an optimized polysilicon film (220 nm) deposited on a photonic trench filled with silicon oxide (about 1.5 μm). The numbers indicate major fabrication steps in the order appearing in the process: (1) and (2), transistor and photonic isolation fabrication; (3) transistor frontend fabrication up to source/drain implant, including gate definition; (4) deposition, annealing and polishing of photonic polysilicon film; (5) polysilicon full and partial etching for forming strip and ridge photonic structures; (6) doping implants (P and N) for active photonics; (7) high doping implants (P++ and N++) and salicidation for both electronic and photonic devices; and (8) metallization. (c) Scanning electron micrographs of different photonic and electronic blocks in our monolithic platform. From [6, Fig. 1].

65 nm bulk CMOS process inside a 300 mm wafer, the authors start from a polycrystalline silicon layer to realize a high-bandwidth wavelength division multiplexing (WDM) transceiver and receiver circuits. For the photonic section, modulators and avalanche photodetectors have been realized using a resonant ring geometry. On the transceiver side, a full digital backend has been integrated including generation of pseudo-random sequences and an inverter chain driving the microring modulators. On the receiver side, a complete analog frontend composed of transimpedance amplifiers and data samplers complete the optical links. Experimental characterization of the realized optical channels reveals 10 Gbps operation.

However, the thicknesses of the silicon (0.2–0.5 μm) and silicon oxide ($> 0.5\mu$m)

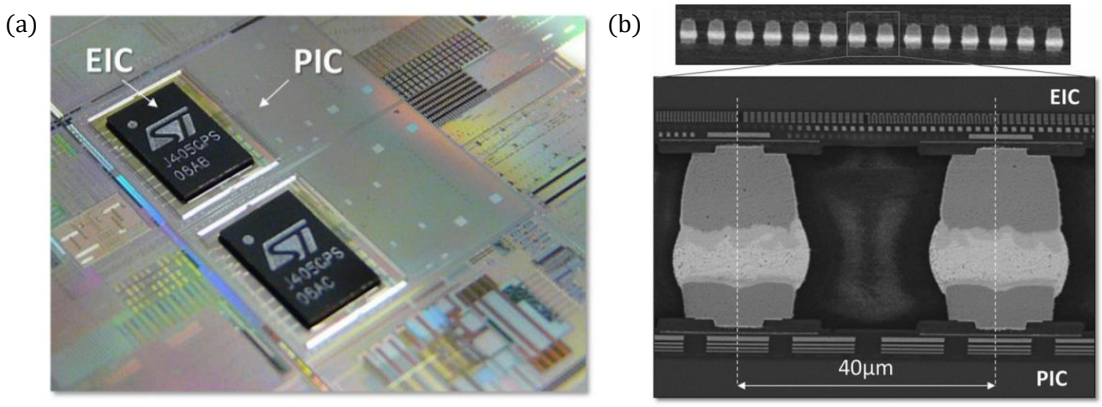

Figure 1.2: (a) Picture of a 3D assembly of an electronic IC (die) over a photonic IC (wafer) defining the OIC sub-system; (b) SEM cross-section of the 40 μm pitch Cu micropillars with SnAg solder capping. From [15, Fig. 1, 2].

layers necessary for a good optical confinement within the photonic layer greatly differ from the dimensions typical of advanced logic technologies (e.g. FinFET), hindering their adoption. A solution is offered by heterogeneous integration where we can employ suitable technological processes for each sub-systems at the expenses of a more complicated packaging. As an example, consider the three-dimensional integration of electrical and photonic ICs presented in a collaboration between Luxtera and ST Microelectronics [15] where the electrical interconnections are realized through a dense array of Cu micropillars on top of the optical modulators and detectors to minimize the signal path length (Fig. 1.2). Within heterogeneous integration, thermal management is the main issue since the dissipated heat from the electronic layer may adversely affect the silicon photonic circuit.

Still challenging is the coupling of light sources with the Si-based photonic circuits. Owing to theirs indirect bandgap, silicon and germanium are not efficient light emitters pushing the research on native group-IV lasers sources. Nevertheless several solutions, from laboratory to industrial scale, are available at present:

- heteroepitaxial growth of III-V materials on Si for the realization of quantum wells (QWs) or quantum dots (QDs) lasers [28];
- heterointegration of III-V on silicon via wafer-bonding [63, 51] or transfer printing [120] techniques for wafer-level integration of a fully processed laser;
- hybrid integration of a packaged laser on the chip (i.e. Luxtera's LaMP [36]);
- adoption of grating couplers and/or spot-size converters to feed light from an optical fiber array.

Any of the above options come with their technological (i.e. capabilities of the silicon foundry to process III-V semiconductors) or economical constraints, such as the use of a packaged laser chip where electrical testing can be easily performed and where the most apt laser technology for our design can be easily integrated.

1.2 Components for silicon photonics

Within photonic integrated circuits (PICs), there are several components allowing to implement the desired functions on chip: from passive components, like waveguides, to active ones such as light sources or photodetectors. The limits of our design are mainly posed by the material system we use (i.e. an electrically-pumped group-IV laser is one of the main *desiderata* in silicon photonics) and by the manufacturer's processing capability (i.e. heteroepitaxial growth of III-V materials on Si require expertise on both semiconductors' technology).

Focusing on the silicon photonics platform, we will briefly introduce what a photodetector and a modulator are and what is their role in PICs.

1.2.1 Waveguide-coupled photodetectors

Once the desired information is encoded in the intensity variation of the guided light, it is possible to employ a photodetector to convert the optical signal in an electrical one. Since we leverage Si transparency at telecom wavelengths for the transmission, we have to look for other semiconductor materials sensitive to the infrared light. In this regard, several factors make Ge appealing for the realization of integrated photodetectors: the availability of CMOS-compatible Ge-on-Si heteroepitaxy (potentially less expensive than III-V/Si integration), a strong absorption at standard telecom wavelengths (i.e. at 1.31 μm, absorption is around 7400 cm^{-1}) and the possibility to exploit strain and Ge-based alloys (e.g. $Ge_{1-x}Sn_x$). However, the large mismatch between Si and Ge lattice constants results in the presence of lattice misfits and threading dislocations which may be cured during the growth process through cyclic thermal annealing steps [73, 33] or via aspect-ratio trapping [14, 93].

Several highly performant Ge-on-Si photodetectors had been realized since then with bandwidth of the order of tens of GHz [59, 64]. However, such structures often rely on vertical illumination schemes where a trade-off between high-speed operation and high responsivity exists constraining the thickness of the absorbing Ge region.

A promising implementation for integrated optics is represented by the waveguide-coupled photodetector where exploiting the "orthogonality" between the electrical

and optical path it is possible to tune almost indipendently the electrical bandwidth and the responsivity of the photodiode. Possible classification of these devices includes how the waveguide feeds the light to detector (i.e. butt-coupling or evanescent coupling) and how electrical current flows across the semiconductor structure (i.e. vertical or lateral). Another separation can be drawn looking at the doping scheme employed the detector is: on one hand, we could employ *pin* photodetectors to target through a careful design high-speed and CMOS-compatible operation; on the other hand, avalanche photodiodes (APDs) had been extensively adopted in noisy enviroments thanks to their enhanced sensitivity but they pose several challenges in the design (e.g. charge layer doping in separate absorption and multiplication APDs) and integration (e.g. APDs need dedicated high-voltage lines which are not compatible with digital operating voltage).

1.2.2 Modulators

Once light has been fed to the photonic integrated circuit, we need the ability to encode and transmit information by modulating the signal's amplitude or phase. To do so, several modulation formats are available but for simplicity we will concentrate on amplitude modulation. One approach consists of modulating directly the instantaneous electrical bias of the laser (internal or direct modulation). Directly modulated vertical cavity surface-emitting lasers (VCSELs) have emerged as a viable and compact solution for high-speed optical communications in data centers [50, 95], but the presence of chirp in the modulated signal may result in the signal degradation for long optical fibers. A second possibility is to use a continuous-wave light source by the introduction of an additional device called modulator (external modulation): in this case, we obtain less stricter requirements on the laser performances shifting all those aspects to the design and optimization of the modulator, at the cost of additional insertion losses.

Modulators can be divided in amplitude or phase modulators whether they act on the intensity or the phase of the optical carrier through variations of the absorption or the refractive index. Still, Kramers-Krönig relations establish that variations in the absorption leads to variations in the refractive index resulting into spurious phase modulation known as chirp. Thus, phase modulators are preferred to absorption ones due to the lower amount of chirp in the output signal. It is possible to attain intensity modulation from pure phase modulation using interferometric techniques where constructive and destructive interference are used to have or suppress the output signal. One of the most common implementation is the Mach-Zehnder interferometer. In its simplest realization, a Mach-Zehnder interferometer starts with an input Y-junction splitter used to distribute the optical field along two equal arms. Here, split fields undergo to a phase variation depending on the chosen physical mechanism and governed by an external (electrical) signal. At last, split fields are recombined at the output Y-junction where depending on the

total phase difference they interfere constructively or not.

Several solutions, relying on different expressions of the electro-optic effect, are readily available for integration in planar lightwave circuit:

- Si-based modulators exploiting free-carriers dispersion, as the one proposed by University of Paris Sud based on interleaved diodes [76];
- Si/Si_xGe_{1-x} multi-quantum well structures based on quantum-confined Stark effect [71, 72];
- thin-film $LiNbO_3$ layers hetero-integrated on Si [116, 16].

Still, dense integration of modulators for the realization of high-capacity optical communication links is hampered by the large modulator's footprint. In this regard, hybrid integration of Si slot waveguides and polymer matrices loaded with chromophores characterized by a large electro-optic coefficient [66, 65, 67] had proven a successful step in the design of next-generation phase modulators. As can be seen in Fig. 1.3, very intense electric fields are found within the capacitive structure defined by the Si walls that, together with the tight confinement of the optical mode, leads to a strong interaction and enhance the modulation process. Same considerations may be extended to the field of plasmonics where important contributions to the development of high-speed compact phase modulators based on MIM slot waveguides have been experimentally demonstrated [40].

1.3 Trends and perspectives

While in this work we focus on photonic devices for telecom applications, research in silicon photonics has opened to several new directions also beyond its native field to span applications from sensing to all-optical computing. A first line of research revolves around the application of Si not only as guiding element, but as detection medium leveraging non-linear effects (i.e. two-photon absorption) or surface states absorption. Consider the so-called CLIPP probes shown in Fig. 1.4 where defect states at the Si/SiO_2 interface of the waveguide make possible to detect the light through a non-invasive conductance measurement [84, 29].

Another possibility revolves around the extension of silicon photonics to the mid-IR range opening the doors to enviromental and biomedical sensing [103]. Photonic building blocks for such spectral range have evolved to include other CMOS-compatible materials (e.g. Ge-based guiding elements [86]), to leverage new phenomena (e.g. photodetection at longer wavelengths using intentional lattice defects [1]) or to integrate new on-chip functionalities like compact Fourier transform spectrometers [94].

More recently, researchers are exploring the use of photonic components to realize optical neural networks (ONNs). Such architectures may outperform their

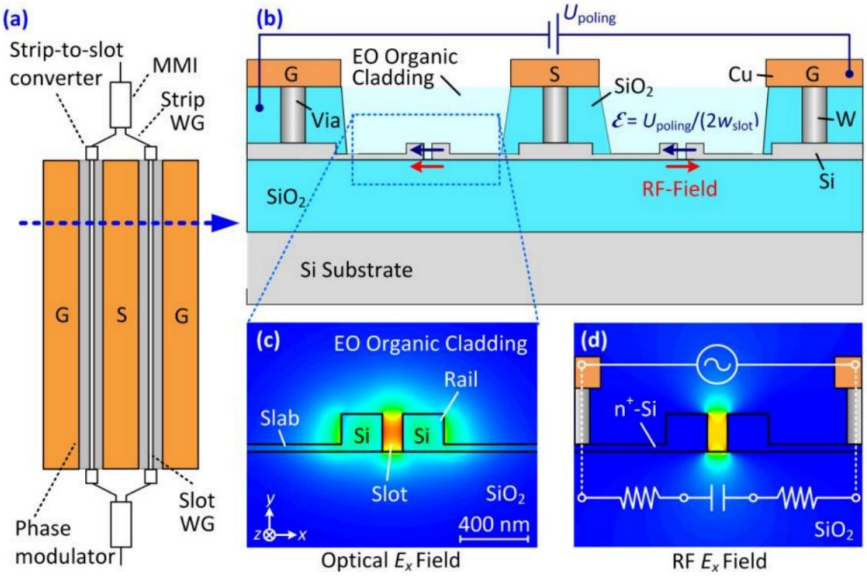

Figure 1.3: Silicon-organic hybrid (SOH) Mach-Zehnder modulator (MZM). (a) Schematic of the MZM. The device consists of two slot waveguide (WG) phase modulators, driven in push-pull operation by a single coplanar ground-signal-ground (GSG) transmission line. (b) Crosssection of an SOH MZM based on tungsten vias that connect the GSG transmission line to the Si slot waveguide. Push-pull operation is obtained by an appropriate choice of poling directions (blue arrows) of the electro-optic (EO) cladding in both arms with respect to the direction of the local RF field (red arrows). (c) Cross-sectional view and simulated optical mode of a single phase modulator (slot width 160 nm, rail width 210 nm). The light is strongly confined to the slot due to electric-field discontinuities at the slot sidewalls. (d) Simulated RF mode field of the slot waveguide. The modulation voltage drops across the narrow slot resulting in a high modulation field that has a strong overlap with the optical mode. From [66, Fig. 1].

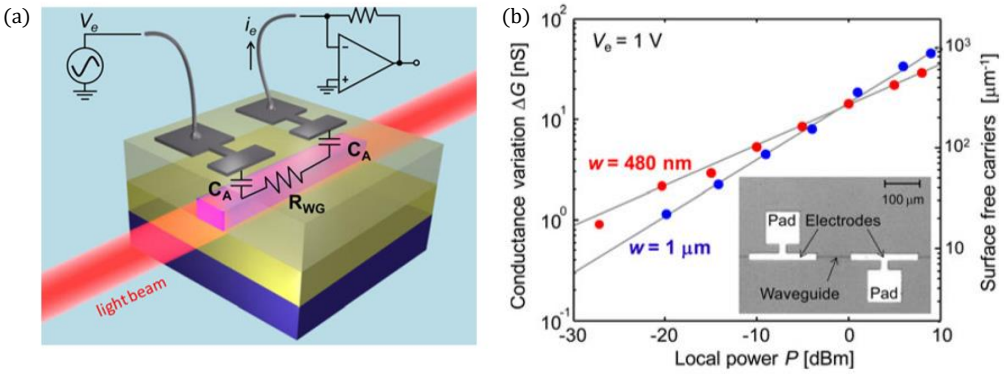

Figure 1.4: (a) Illustration of the CLIPP device consisting of two metal electrodes deposited onto the electrically-insulating upper cladding and capacitively coupled to the electrically-resistive silicon waveguide; (b) Optical power monitoring performed with a CLIPP. Measured conductance variation ΔG versus the optical power P for a single mode (red) and a multimode (blue) silicon waveguide. From [84, Fig. 1, 2].

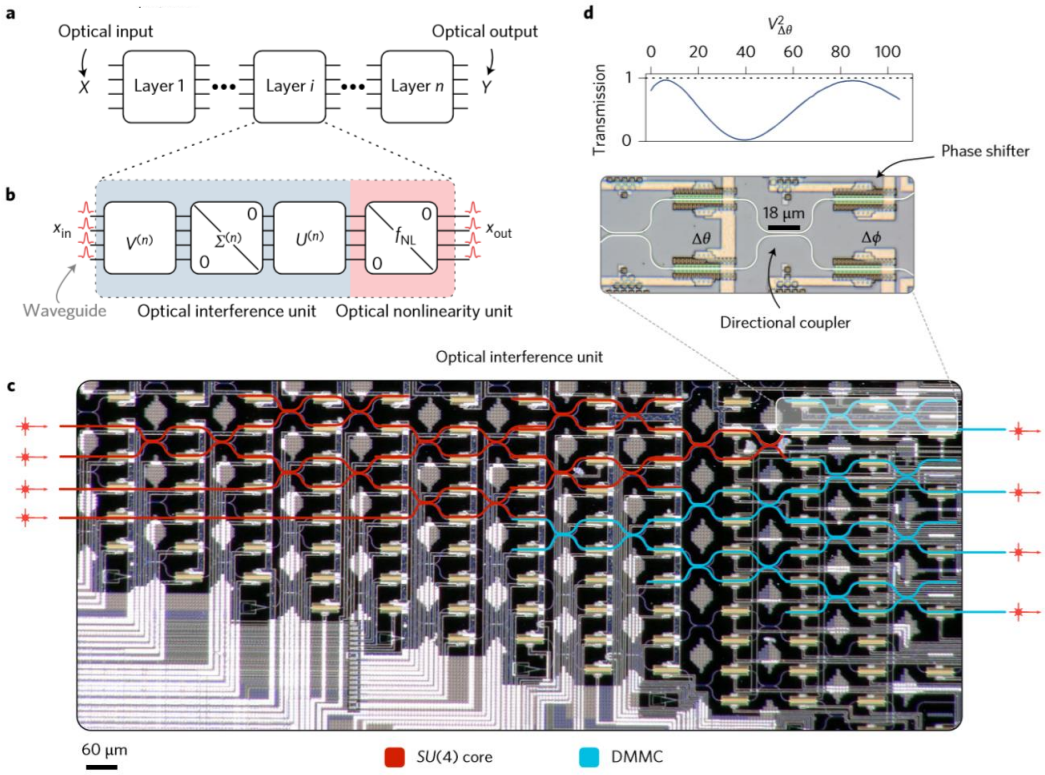

Figure 1.5: (a) Optical neural networks decomposed into individual layers; (b) Optical interference and nonlinearity units that compose each layer of the neural network; (c) Optical micrograph illustration of the demonstrated optical interference unit which realizes both matrix multiplication (red) and attenutation (blue) fully optically; (d) Schematic illustration of a single phase shifter in the MZI and the transmission curve for tuning the interal phase shifters. From [101, Fig. 1, 2].

electrical counterparts in terms of speed and energy consumption especially during the more intensive training phase. As an example, meshes of Mach-Zehnder interferometers can implement the inference process while saturable absorbers cover the non-linear behaviour [101].

Chapter 2

Waveguide-coupled photodetectors

This chapter is focused on the computer-aided design of the waveguide photodetectors, both *pin* and avalanche (APD) versions, starting with a review on the current state of the art. After a brief discussion on the open research questions, we introduce some novel results on the multiphysics simulation of those devices, presented in [91, 92].

2.1 Fundamentals

Photodetectors enable the connection between optical and electrical sub-systems, allowing to receive information from the optical channel and/or to process the output electrical signal. Typically, such connection is realized through the optical generation of electron-hole pairs from incoming light. This physical phenomenon depends on the optical absorption $\alpha(\lambda)$ of the active semiconductor, which determines the spectral range of operation, and on the optical power P_{opt}, which determines the amount of photocurrent i_{opt} produced at the contacts.

If we identify with the symbol $I(V, \lambda, P_{opt})$ the constitutive law of the photodetector, we can identify the main figures of merit for these devices:

- in absence of light, the dark current i_d is the current produced from the detector while operating at a certain bias point. It determines the static power consumption of the device and it is strongly affected by imperfections in the fabrication, such as traps and defects, thus making the dark current an useful indicator of the process' quality.

$$I(V, \lambda, 0) = i_d \tag{2.1}$$

- the photocurrent i_{opt} is the contribution to the total current due to the incident light.

$$I(V, \lambda, P_{opt}) = i_{opt} + i_d \tag{2.2}$$

  A strictly related quantity is the responsivity $\mathcal{R}(V, \lambda)$ which express, for low-level input optical power, the relation between photocurrent and input optical power.

$$i_{opt} = I(V, \lambda, P_{opt}) - i_d \approx \mathcal{R}(V, \lambda) P_{opt} \tag{2.3}$$

  Responsivity may be considered independent from the applied voltage when operated at low reverse bias. This is not the case, for example, with avalanche photodetectors where the enhancement in the responsivity from the multiplication gain is a voltage-dependent phenomenon.

- in the small-signal regime, we look at the electrical AC analysis to retrieve information on the frequency behaviour of our device (i.e. cut-off frequency f_{-3dB}). Also of interest for high-speed optical applications, such as the ones found in photonics, is the computation of the electro-optical transfer function which relates the small-signal output electrical response to the sinusoidally-varying optical signal.

From an electrical standpoint common geometries exploits junction-based devices, such as *pin* [2, 35] or Schottky structures [4, 5], operated in reverse bias where the strong electric field helps in sweeping off the carriers from the absorption region. Through a careful design, it is possible to reach cut-off frequencies on the order of tenths of GHz [55] while keeping the dark current on the nA scale.

On the other side of the spectrum we find the so-called avalanche photodetectors (APD) where the phenomena of impact ionization provides an internal gain mechanisms capable to boost the photocurrent, improving the detector's sensitivity in noisy environment.

A conventional APD design requires an absorption and a multiplication region: the former provides photo-generated electron-hole pairs; the latter sustains the avalanche generation phenomena thanks to the high electric field. Those regions may coincide as in a *pin* detector where the applied bias is high enough to trigger the impact ionization or they may differ as in SAM-APD (separate absorption and multiplication APD) [78, 115]. A key element for the proper functioning of SAM APDs is the so-called charge layer. In its simplest realization, it consists of a relatively thin doped layer separating the absorption and multiplication regions. Its duty is two-fold: confine the electric field in the multiplication region so that no impact ionization processes are triggered in the absorption region while guaranteeing an electric field high enough to saturate the carrier velocities so to minimize the transit-time in the absorption region.

In both cases, APDs tends to be noisier and slower than their *pin* counterpart due to the avalanche generation phenomena.

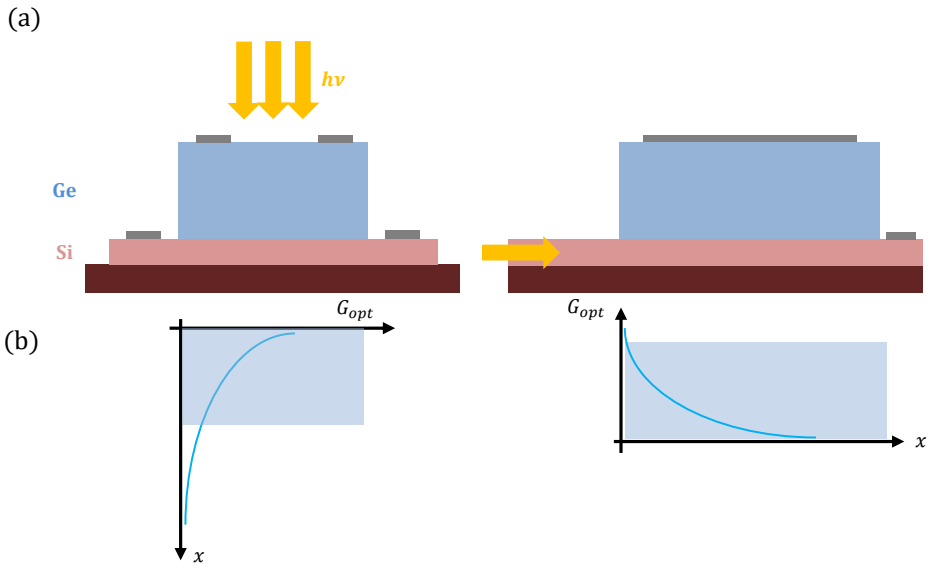

Figure 2.1: (a) Schematic of a conventional vertically illuminated photodiode (left) and of a waveguide-coupled detector (right); (b) comparison of the optical generation profiles against the propagation direction for the two illumination strategies. Height of the Ge area is kept equal to highlight the advantage of the waveguide illumination scheme.

Beyond the quantities already listed for non-avalanching photodetectors, we are interested in the computation of the multiplication gain from which we can obtain the gain-bandwidth product and the enhancement in the detector's responsivity. Also of interest is the breakdown voltage since it determines the operating point of the device.

Another fundamental aspect to keep in mind is how the photodetector is illuminated. As shown in Fig. 2.1, in conventional devices an intrinsic region W_i much greater than the inverse of the absorption $L_\alpha = 1/\alpha$ is required to maximize the light absorption. However, the cut-off frequency varies with the thickness of the intrinsic layer: for small (big) values of W_i, the maximum bandwidth is limited by the RC (transit-time) effects. In the end, longing for high-speed devices may drastically reduce the amount of photocurrent extracted. A valid alternative is represented by the waveguide-coupled photodetector in which the semiconductor absorbing region composes or is grown on top of the optical guiding element. In this way, the incoming photon flux and the electron flux have 'orthogonal' paths making possible to optimize separately the requirements on responsivity (long devices to completely absorb the optical signal) and frequency response (thin regions to minimize the carrier's transit time).

The incoming light from the waveguide can be coupled to the Ge region either directly by butt-coupling or by evanescent coupling. While both illumination schemes make possible to realize an almost total absorption of the incoming light, some of the highest bandwidths-efficiency products reported nowadays are for butt-coupled devices [35, 112], which offer high confinement of the optical mode and very compact devices. Evanescent coupling, on the other hand, proved to be an efficient coupling solution to handle high-level input optical power [20].

It is also possible to refine our classification of waveguide-coupled photodetectors using the direction of the electrical current in the transverse plane to distinguish between lateral and vertical devices. Both approaches yield similar performances although lateral designs exhibit an higher responsivity thanks to the removal of metallic elements and highly-doped regions nearby the Ge active region [98, 121, 25].

2.2 Review of the state of the art

The development of Ge-on-Si waveguide-coupled photodetectors had to face a strong competition with the InP-based platform. On one hand, there was no suitable process to grow monocrystalline Ge on the Si wafer, despite most of the efforts were concentrated on the $Si_{1-x}Ge_x$. On the other hand, III-V semiconductors and their alloys (i.e. InP, $In_{1-x}Ga_xAs_{1-y}P_x$) provide a whole set of optoelectronic devices operating at 1.55 μm which are largely employed in long-haul optical communications but they lack of a cheap heterointegration technology. With the advent of low-temperature buffer Ge-on-Si heteroepitaxy [34, 73, 33], high-quality germanium layers can be grown despite the large lattice mismatch with the silicon substrate. The deposition technique is composed by two steps: first, a thin layer of $\approx$ 50 nm is grown at an initial temperature of about 330° C; second, the temperature is increased up to 500° C to increase the quality of the grown material and to reduce the total deposition time. Since its introduction, there was a boost in the field producing in few years some incredible results in terms of responsivity and electro-optical cut-off frequencies for *pin* and high gain-bandwidth products for APDs.

In 2007 Ahn et al. [2] presented a vertical *pin* photodetector where the optical coupling is realized through a silicon nitride (SiN) or silicon oxynitride (SiON) waveguide. About the realization of the electronic device, Ge volume was grown on the Si substrate through two-temperature heteroepitaxy. A poly-Si layer is deposited on top to serve as top contact and as reference surface for the waveguide placement. The device, operated at 1.55 microns, shows a responsivity of 1.08 (0.96) A/W for the SiN (SiON) waveguide. Such difference is mainly due to the higher refractive index in SiN (2.2) compared to SiON (1.8) which makes possible to a have a better light confinement. Regarding the small-signal analysis, experiments

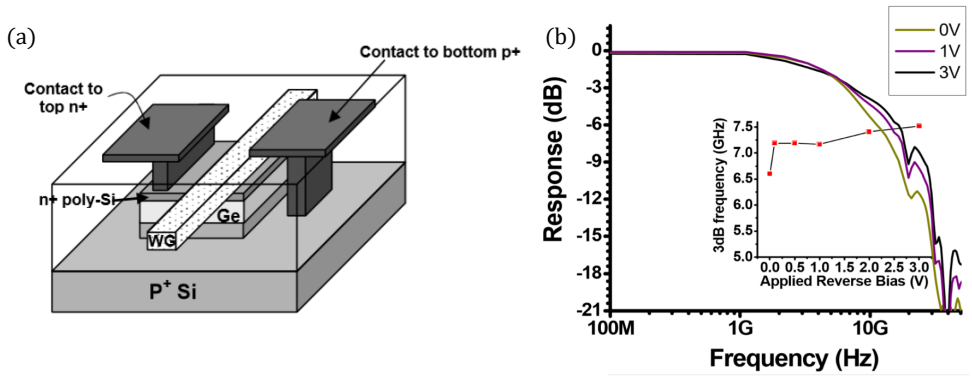

Figure 2.2: (a) Schematic structure of a waveguide-integrated Ge *pin* photodetector; (b) Electrooptical transfer function obtained by impulse response measurement showing a ≈7.5 GHz 3dB frequency. The inset shows the dependence of 3 dB frequency on applied reverse bias. From [2].

report a cut-off bandwidth around 7.5 GHz with a reverse bias of 3 V.

Still another vertical structure was presented by Vivien et al. [113], offering low dark current, high responsivity and cut-off bandwidth at 1.55 μm. The footprint of the grown Ge region is 3 μm × 15 μm with a height of 340 nm , buffer region included. Light is fed to the device in a butt-coupled approach using a rib waveguide, allowing for a good overlap between the input field and the Ge cross-section. Experimental characterization report a dark current of 60 nA at 1 V reverse bias which is attributed to the dislocation and surface roughness in the Ge region, while responsivity is found to be 0.9 (1.0) A/W at 0.9 (4.0) V reverse bias. Regarding the dynamic response, characterization showed a record high 42 GHz −3 dB bandwidth at 4.0 V.

A group from Sandia National Laboratory presented in 2011 a butt-coupled vertical *pin* photodiode [35] with a compact footprint (1.3 μm × 4 μm) resulting in large cut-off bandwidth of 45 GHz at 1.0 V reverse bias. For the fabrication the authors followed a different path regarding the growth of the germanium region. In a typical process, the Si platform is blanket-covered during the Ge deposition and the device is shaped through successive lithography and etching steps. Here the authors shaped the Ge region through a selective area growth by opening a window in the field oxide and exposing the Si platform. Germanium deposition thus proceeds with the two-temperature process letting the semiconductor to overgrow the trench. Excess germanium is later planarized through a chemical-mechanical polishing (CMP) step. This solution mitigates the phenomenon of misfit dislocations because they terminate on the oxide surface without further damage to the Ge region. Illumination is provided with a Si rectangular waveguide coplanar to

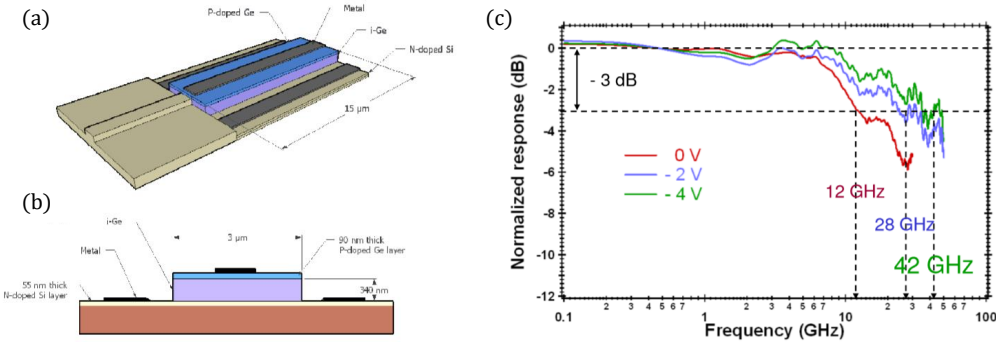

Figure 2.3: Perspective view (a) and cross-section (b) of *pin* germanium photodetector integrated in SOI waveguide. The photodetector length and width are 15 µm and 3 µm, respectively. (c) Normalized optical responses versus frequency for *pin* diode integrated in SOI rib waveguide under 0 V, -2 V, and -4 V biases at the wavelength of 1.53µm. From [113].

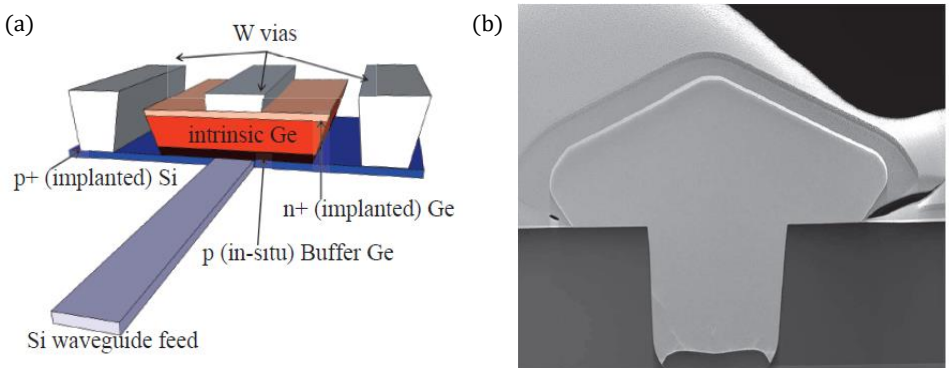

Figure 2.4: (a) Schematic of germanium waveguide *pin* photodiode (b) TEM cross-section of selective area epitaxially grown Ge structure showing overgrowth before CMP and low threading dislocation defect density. From [35].

the platform supporting the Ge detector. The experimental structures were realized for few values of width and length of the Ge region and were characterized in terms of dark current, responsivity and cut-off frequency. It is possible to appreciate from the measurements in Fig. 2.5 a linear dependence between the total dark current of the detector for growing widths. This behaviour highlights how effective the selective area growth is in the reduction of the misfit density especially for narrower devices. The responsivity increases for longer devices while showing a slight dependence on the diode width thanks to a better coupling between the input waveguide's mode and the detector's modes. The electrooptical characterization, realized with an optical heterodyne measurement whose data were fitted to a one-pole model, reveals a bandwidth of 45 GHz with 300 μA output current at 1 V reverse bias for the smallest device beating the previous record of 42 GHz [113]. Furthermore, the structure produces a bandwidth of 37 GHz at zero bias applied, demonstrating the possibility of low-voltage operation.

In a successive iteration, Vivien and his collaborators proposed a butt-coupled lateral structure entirely realized in Ge [114] working at 1.55 micron and capable to operate at 40 Gb/s with no applied bias. In the fabrication, the germanium was selectively grown in a 10 μm $\times$ 10 μm cavity obtained from the Si platform through etching. As with the Sandia structure, Ge overgrowth is desired to suppress the dislocation density. After a cyclic thermal annealing to heal the defects and a CMP step to remove the excess semiconductor, a self-aligning process is used to define an intrinsic Ge region of 500 nm. From heterodyne measurements the authors estimated the -3 dB-bandwidth in 120 GHz, a value almost twice the predicted one of 53 GHz obtained for a 500 nm intrinsic region. To explain this result, the authors indicate dopant drift caused by the thermal annealing as main culprit leading to a reduction of the intrinsic region.

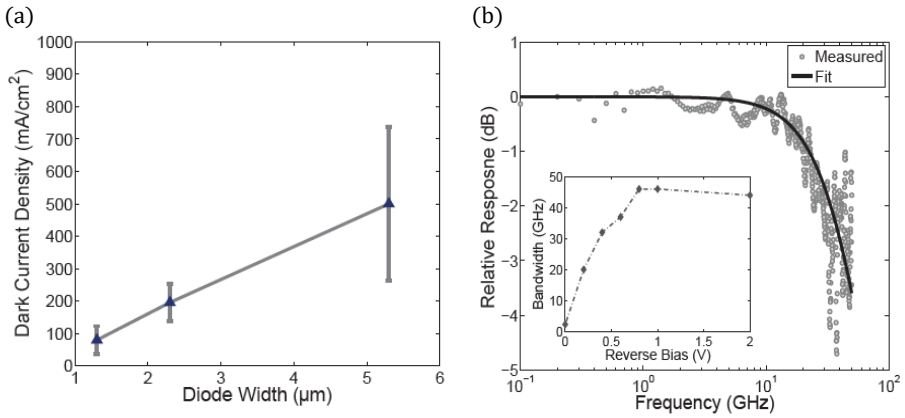

Figure 2.5: (a) Measured linear trend between dark current density at 1 V reverse bias and photodiode width. Bandwidth of 1.3 × 4.0 μm^2 Ge photodiode at 2 V reverse bias, measured using an optical heterodyne technique showing a 3-dB roll off frequency of 45 GHz. Inset shows saturation of bandwidth at 0.8 V reverse bias for a photocurrent of 300 μA. From [35].

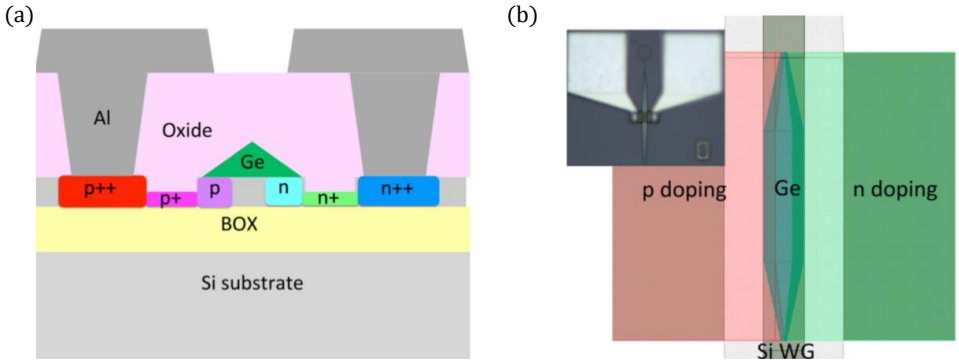

Figure 2.6: (a) Schematic cross-section and (b) layout and a photo of the floating germanium detector. Only silicon, germanium, p and n doping layers are shown. From [121].

In 2014, researchers started investigating some Ge-on-Si lateral structures characterized by a floating Ge region. In these structures the contacts are moved away from the germanium region simplifying the process flow and reducing the optical losses from the associated metallizations and highly doped regions. Since there is no reverse bias applied to the intrinsic region, the extraction of photogenerated carriers is mainly due to the fringing field across the Si junction. A first example was produced by Zhang et al. [121] where a Ge region 1.50 μm wide had been grown on top of a Si *pin* junction. To maximize the coupling between the Si rib waveguide and the Ge detector, a 3 μm long taper had been employed to adiabatically couple the two elements. Once operated at -4 V, the device exhibits an electrooptical bandwidth of about 20 GHz with a responsivity of 1.14 A/W while sacrificing the compatibility with CMOS electronics.

An improvement on this design arrives from Ghent University and IMEC [25, 22] where the authors present a comparison of lateral and vertical structures performed by means of TCAD simulations and experiments. In Fig. 2.7 the cross sections of the lateral and vertical structures are reported. This comparison highlights how the metallization and the doping scheme for the lateral structure shares many features with the one employed in silicon modulator. Experimental characterization of the lateral and vertical designs had been carried out using slightly different width of the Ge regions (0.50 vs. 0.80 μm). Static characterization shows for the lateral structure a dark current lower than 10 nA over the range [-3, 0] V where the vertical one report values three times higher. Such difference is explained looking at the electric field profiles obtained with simulations: while the lateral design reports an almost uniform field crossing the Ge section, in the vertical one the majority of the electric field is peaked at the heterointerface where the large concentration of defects increases the current leakeage under high-electric field. Responsivity

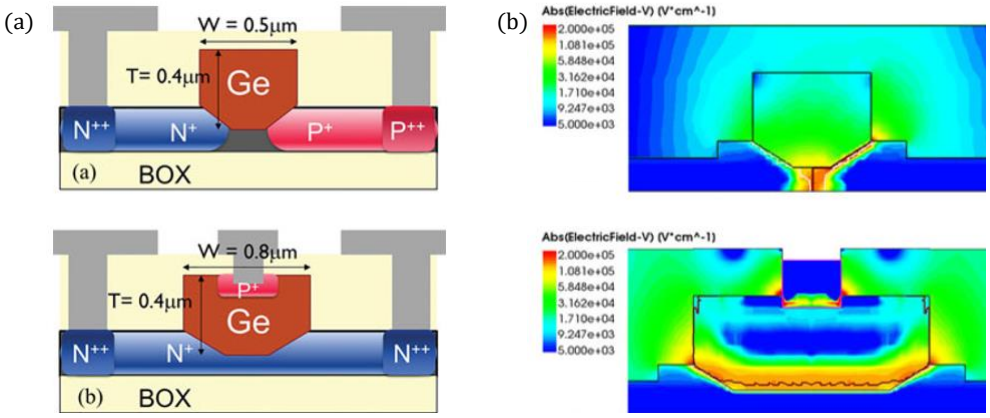

Figure 2.7: (a) Schematic cross-section with germanium dimensions of a lateral (top) and vertical (bottom) Si *pin* photodetectors; (b) Electric field distribution in lateral (top) and vertical (bottom) Si *pin* photodetector at -1 V. From [24].

in the wavelength range between 1505 and 1580 nm had been measured for both devices: the lateral structure produce a responsivity higher than 1 A/W over the whole range with the vertical ones set around 0.4-0.6 A/W. Then, data-transmission experiments were carried out using a 1.55 μm light source modulated with a 28 Gb/s non-return to zero pseudo random sequence via an external $LiNbO_3$ modulatorù. -3 dB bandwidths as a function of applied bias were measured showing a rather low bandwidth at zero bias for the lateral structure (2.7 GHz) if compared to the vertical design (36 GHz). This is partly due to the low field strength which increase the transit time in the lateral device. Same measurements were repeated on lateral structures with different widths of the intrinsic Ge region showing a transit time limited bandwidth which increase for narrower devices and increasing voltage.

To enhance the cut-off frequency of the lateral structures, the authors propose a thinner Ge layer to reduce (i) the weak-field region where the carriers do not drift at their saturation velocity and (ii) the maximum distance travelled by the carriers to reach the contacts. In a successive paper [22], the authors adopts a thinner Ge region compared to the previous reports (0.16 μm vs. 0.40 μm). Responsivity have been measured at 1310 and 1550 nm with a mean wafer-scale value of 0.74 A/W and 0.93 A/W. Measured electrooptical bandwidth for both wavelengths are 45 GHz and >50 GHz at -1 V while at higher voltages it increases to 67 GHz and 50 GHz. This asymmetry is explained in terms of the higher germanium absorption coefficient at 1310 nm where the strong optical generation screens the electric field reducing the drift velocity and the total bandwidth. For the devices operating at 1550 nm, the impact of input optical power on the electrooptical bandwidth had been evaluated where a roll-off of the bandwidth was observed especially at low biases due to the screening effects.

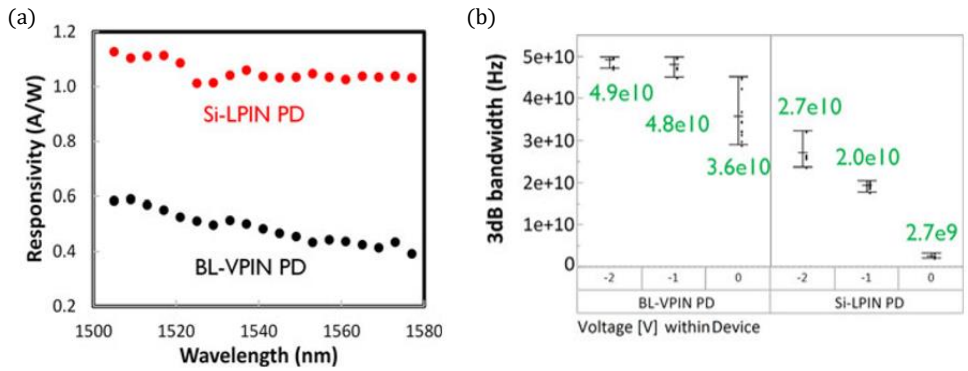

Figure 2.8: (a) Responsivity versus wavelength for the lateral and vertical Ge photodetector; (b) Wafer-scale electrooptical 3 dB bandwidth of the lateral and vertical photodetector at 0, -1 and -2 V. The mean of the wafer-scale data is annotated explicitly in the graph. From [24].

Another line of research focused on the handling of high-level of input optical power. Standard butt-coupling strategies delivered some of the most performing devices, but for increasing input optical power they experience current saturation and a reduction of the total bandwidth due to the intense photogeneration in the Ge region. In a proposal from MIT [110, 19, 20], the light from the Si had been coupled to a vertical detector through an asymmetric tapered lateral waveguide coplanar with the Si base. In this way, the optical power can be gradually transferred to the Ge region reducing the strong absorption encountered in butt-coupling solutions through a broad-band approach. Experimental realizations included in the fabrication both the butt-coupled both the proposed lateral coupler to limit the detector's variability from the Ge growth. Static characterization over the bias range [-3, 1] V show a a dark current on the nA level. Measured responsivity at 1550 nm and -1 V for narrower Ge diodes (1.20 μm) show a small difference between the butt-coupled and lateral solution (0.80 vs. 0.70 A/W) which reduces to almost zero for larger devices (1.0 A/W for 1.20 μm wide devices). Then, in a second experiment photocurrent was measured while varying the amount of optical power: both coupling strategies present a linear dependence up to 6 mW where the butt-coupled diodes show some saturation limiting the photocurrent to 9.1 mA for 28 mW in input. The lateral coupler, instead, continues to produce photocurrent up to 15.5 mA at 28 mW showing how from a better distribution of input power it is possible to reduce the saturation effects. A similar behaviour is observed in the dynamic electrooptical response where for low-level optical power there is no evident advantage between the two coupling strategies: the detector shows a transit-time limited cut-off frequency of 40 GHz with 20 μW. For an input power of 4 mW, the bandwidth of the butt-coupled detector drops to 0.7 GHz while the lateral one stands at 31 GHz.

Turning our attention to APDs, most of the implementations in literature adopt a separate absorption and multiplication (SAM) design with Ge for the absorption region while Si is usually adopted as multiplication layer thanks to its lower ionization coefficient. There are also few notable examples of hybrid III-V/Si SAM APD detectors where an $In_{1-x}Ga_xAs$ region is used as optical absorber [43, 42], but the challenge on the integration of III-V in a silicon CMOS process is still open.

Despite being a conventional mesa-type SAM APD, in 2008 Kang et al. [62] introduced one of the first monolithically grown Ge-on-Si avalanche detector to attain a record high gain-bandwidth product of 340 GHz. To realize the device, the authors start from a SOI wafer with a low-doped Si substrate on top of which is grown the Si multiplication region and the Ge absorption region via the usual two-temperature process. Thus, the device is shaped into circular mesa via a successive etching phase and its sidewalls are passivated using amorphous Si. In the end, the whole detector is covered with silicon nitride and it is contacted using Al pads. With respect to the initial results of 46 GHz and 153 GHz reported in [61, 60], the large improvement in performance is linked to mainly two factors: a stronger doping

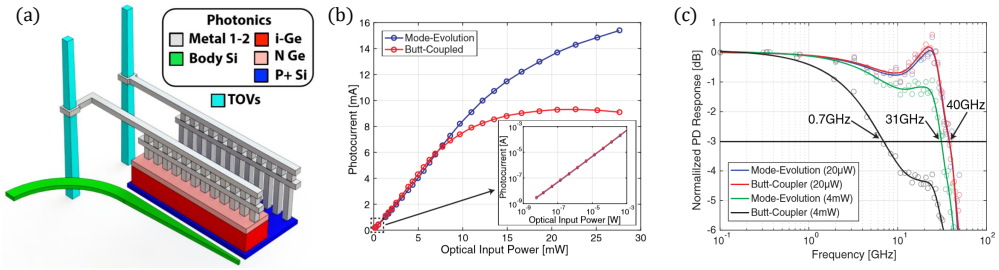

Figure 2.9: (a) 3D depiction of the Ge detector; (b) Electric field distribution in lateral (top) and vertical (bottom) Si *pin* photodetector at -1 V. (b) Measured photocurrent as a function of 1550 nm TE-polarized input power to the 1.5 × 12 μm^2 detector for both butt- and mode-evolution-based couplers; (c) Measured frequency response of a 1.5 × 12 μm^2 detector with each coupler at 20 μW (red and blue curves) and 4 mW total input power (black and green curves). From [110, Fig. 3], [20, Fig. 4, 5].

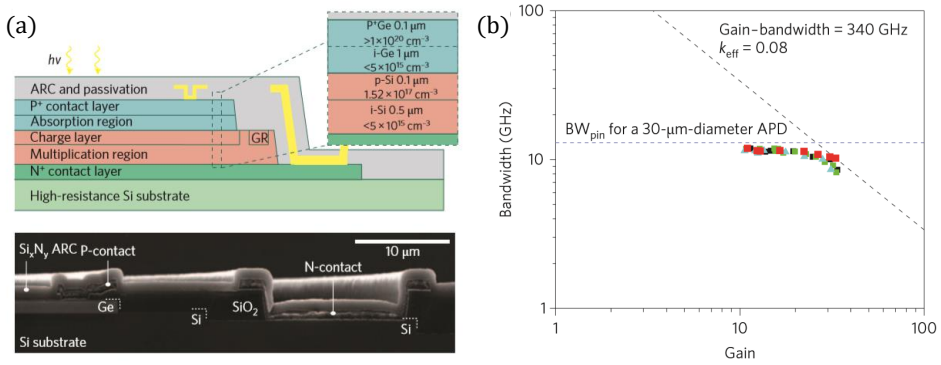

Figure 2.10: Schematic (a) and SEM (b) cross-sections of a germanium/silicon APD. Doping concentrations and layer thicknesses were confirmed by secondary ion mass spectrometry (SIMS). The floating guard ring (GR in a) design was used to prevent premature breakdown along the device perimeter. ARC, anti-reflection coating; (c) Measured 3-dB bandwidth versus gain of 30-mm-diameter germanium/silicon APDs at a wavelength of 1300 nm. The coloured symbols are measured bandwidths from four devices. The blue line is the calculated bandwidth assuming carrier transit time and RC time constant are the limiting factors for the device bandwidth. The black line is a calculated result considering the avalanche build-up effect with $k_{eff} = 0.08$. The corresponding gain-bandwidth product is 340 GHz, which fits the measured values. From [62, Fig. 2, 4].

profile in the charge layer to better confine the electric field in the silicon region and a lowered annealing temperature for the germanium temperature to reduce the interdiffusion of silicon and germanium. The dilution of the Ge composition near the heterointerfaces reduces the absorption of the active region, spoiling the responsivity especially at longer wavelengths [85].

However, when transposing a Ge-on-Si stack as the one proposed to a waveguide-integrated geometry the thick Si multiplication layer may worsen the coupling with the Ge absorbing region. In 2009, researchers from the A-STAR institute in Singapore [122] proposed a SAM structure where the charge layer and the multiplication region are embedded in the Si base. In Fig. 2.11 a complete schematic of the device is reported. If the i- and p-Si regions are all n^+-doped, the device is a conventional vertical Ge/Si *pin* photodiode. Experimental characterization was carried using two photodiodes with the same geometry but different in the doping scheme so to have a *pin* and an APD version to be compared. Under illumination at 1.55 μm, measured photocurrent from the *pin* diode is around 70 μA at 5 V reverse bias where the APD outputs a current 26 times larger (1.8 mA) with a responsivity value of 7.2 A/W and a gain of approximately 6. On the dynamical response, we find a

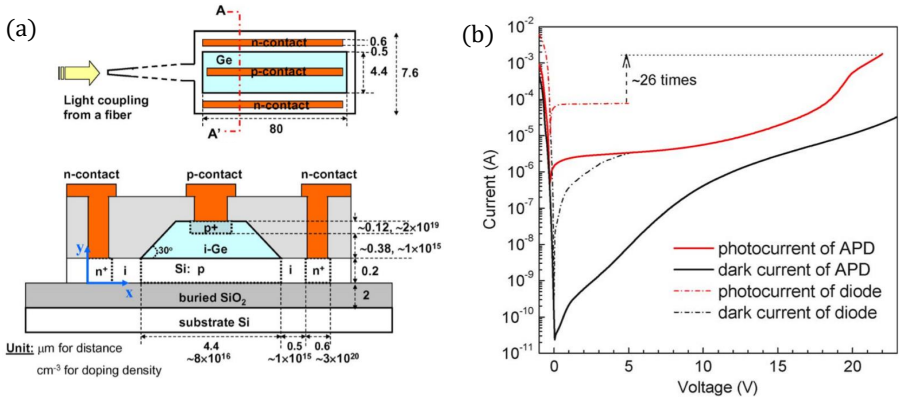

Figure 2.11: (a) Top and cross-sectional views of the waveguide Ge/Si SACM APD; the dimensions and approximate doping densities are also defined. The waveguide has a 0.2-μm-width inverted taper at the facet and is 2 μm wide near the device region. The Ge active layer is selectively grown on the rectangle p-Si region with a width of 4.4 μm and a length of 80 μm, centered in the 7.6-μm-wide device region; (b) Dark current and photocurrent of the waveguided APD and the corresponding Ge/Si *pin* diode under an illumination of 1550-nm/0.25-mW light coupled into the waveguide. The APD provides around 26 times larger photocurrent than its *pin* counterpart. From [122, Fig. 1, 3].

measured 3 dB bandwidth slightly smaller than the one from the *pin* structure (3.3 vs 5.5 GHz) but the design has still space for optimizations.

A similar structure was then considered by the research team from Sandia National Laboratory which presented their interpretation of a linear mode APD [78, 77] and a Geiger-mode APD [79]. Experimental devices had been realized through the same process flow of the previous *pin* diode [35], but an additional mask had been employed to shape the charge layer using the Ge width as reference and a positive overlap parameter with respect to the Ge sidewalls: in this way, we can pack a nominally higher charge by keeping the same wafer. In the experimental realizations the authors explore the design varying the multiplication width and the overlap parameter such that their sum is kept constant. Static and dynamic response had been measured for detectors with length of the detector's arm in the range [0.3, 1.0] μm, while the reference *pin* result comes from the past design by DeRose et al. [35]. Looking at the devices with zero overlap parameter, at the highest applied bias the detectors with a multiplication width of 1.0 (0.5) μm have a gain of 69.3 (14.3) and a bandwidth of 6.24 (9.81) GHz leading to a gain-bandwidth product of 432 (140) GHz. Such gain-bandwidth product is one of the best results obtained with a waveguide-coupled structure and it is comparable to previously reported values obtained from vertically illuminated detectors.

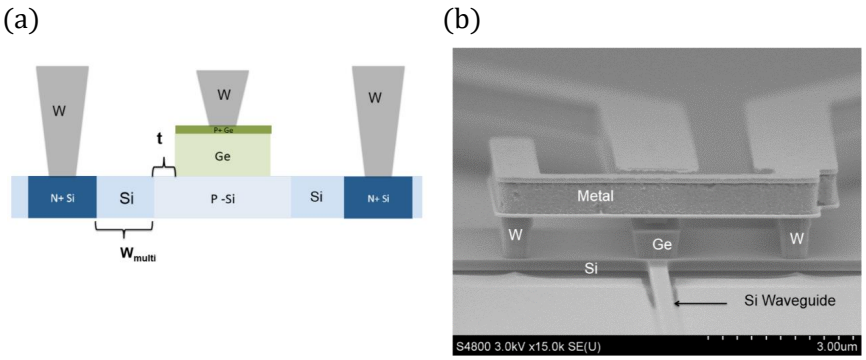

Figure 2.12: (a) Schematic cross-section of waveguide-coupled linear mode APD with p-charge layer overlap t relative to Ge and the multiplication width W_{multi}, indicates width of intrinsic Si multiplication region; (b) Angled SEM image of Ge on Si device structure with oxide cladding removed. From [78].

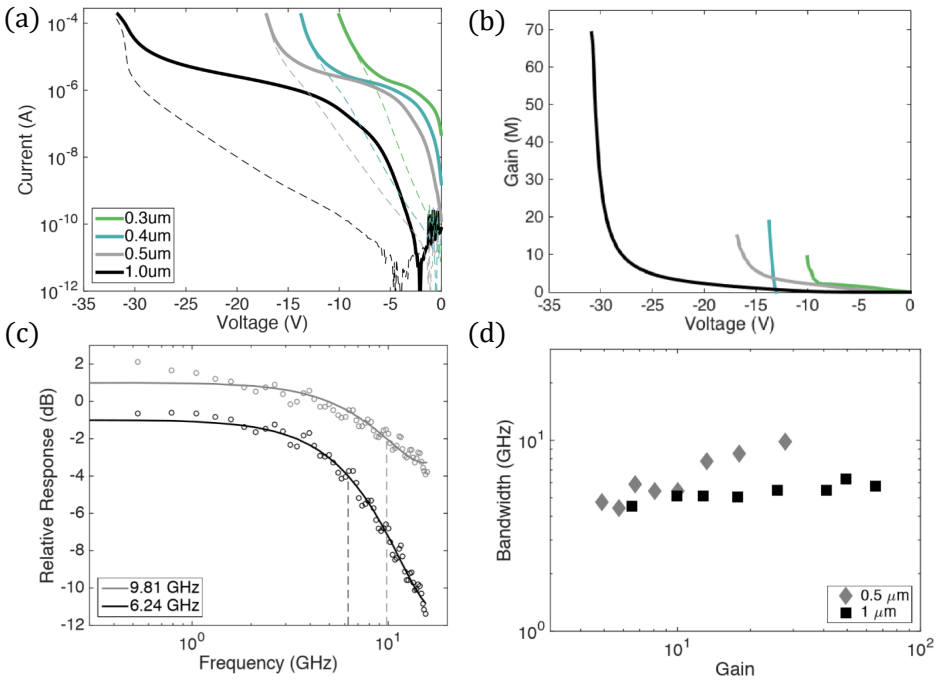

Figure 2.13: Device characteristics for the no-overlap device for various multiplication widths. (a) I(V) characteristics for each APD where solid (dashed) lines are under illumination (dark); (b) Gain obtained from the I(V) curves under illumination; (c) Measured frequency response at bias voltage corresponding to highest gain; (d) Bandwidth vs. gain for each device. From [78].

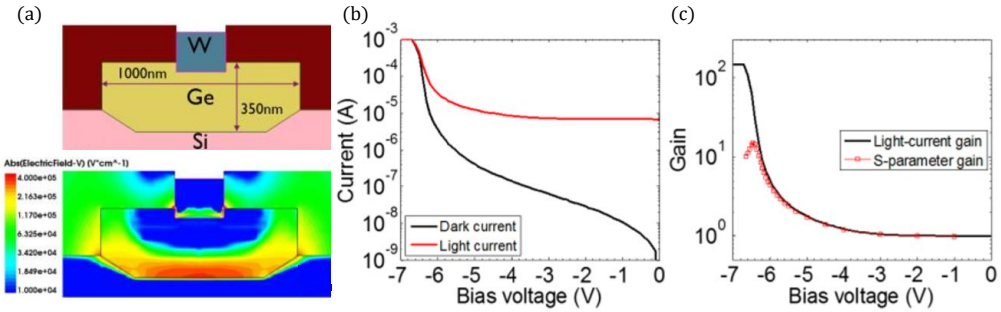

Figure 2.14: (a) Schematic cross-section of the Ge waveguide APD (top) and simulated electric field distribution at -3 V applied voltage (bottom); (b) I(V) characteristics of a 10.4 μm long Ge APD; (c) Static light-current avalanche gain and small-signal avalanche gain. From [26].

A considerable effort was poured in the design of APDs with low operation voltage, removing the need for a dedicated high-voltage supply and making possible to drive the APD with standard CMOS circuitry.

The photonic research group from IMEC and Ghent University proposed in 2014 a Ge/Si vertical *pin* structure [26] where a non-uniform electric field as high as $3 \cdot 10^2$ kV/cm at -3 V is tightly confined producing a strong avalanche generation at moderate bias. Multiplication gain is extracted from the measured photocurrent at 1550 nm normalized to the photocurrent at -2 V where the device operate as a standard photodetector with a responsivity of 0.53 A/W. Fig. 2.14 reports the avalanche multiplication gain against the applied bias: in the range [-3.5, 0] V the Ge photodiode has a *pin*-like behavior while it operates as a linear APD for higher bias till the breakdown voltage with a gain of 14.8. Electrooptical dynamic response reveal a gain-bandwidth product of 88 GHz with a gain of 7.2 obtained at -6.2 V, making possible 10 Gb/s operation at low voltage. In a successive iteration, the authors review the *pin*-APD's design to operate in the 1.31 μm window demonstrating operation at 10 and 25 Gb/s [27, 23].

Between 2016 and 2017, HP researchers presented two variations on the low-voltage SAM APDs theme. Huang and collaborators [52, 53] propose an evanescently-coupled SAM APD design where, on top of an epitaxially regrown Si layer optically coupled to the input waveguide, the Ge absorbing region is moderately doped. Although the doping may increase the dark current, it actually helps in concentrating the electric field in the intrinsic Si multiplication region loosening the constraints on the charge layer doping. To further reduce the bias necessary to trigger the impact generation the detector employs a Si multiplication region approximately 100 nm thick. DC measurements indicates exponential increase of the photocurrent from the -2 V with breakdown occuring around -10 V. From electrooptical impulse

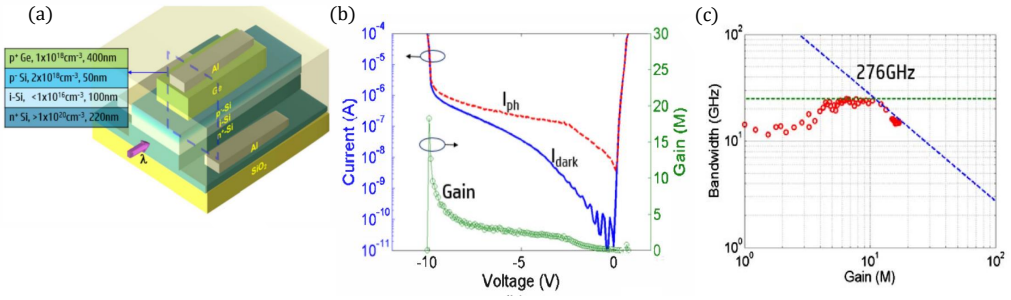

Figure 2.15: (a) Schematic of the waveguide APD structure. The inset shows the layer thickness and doping concentrations for each layer for design; (b) Current-voltage plot for a 4 μm × 10 μm APD in dark (blue) and under illumination (red). In green, calculated APD gain assuming the unity gain at -2 V; (c) The bandwidth versus the gain for the same device. The red circles are the measured bandwidth at various gains; the green dashed line shows the highest bandwidth of 25 GHz, and the blue dashed line shows a constant gain-bandwidth product of 276 GHz. From [52, Fig. 1, 2].

response measurements, the authors measure the cut-off bandwidth for different values of the multiplication gain obtaining a GBP of 276 GHz where this value accounts for RF losses.

In the second proposal the absorption and multiplication region are actually decoupled by means of a third contact which make possible to tune independently the voltage drop on each section [54, 118, 119]. While the first voltage drop sweeps the photogenerated carrier out the Ge region, the second applied bias controls the Si multiplication process across a series of interdigitated n, p-doped regions 300-700 nm wide and separated by 200-600 nm. Voltage required to trigger the avalanche generation can be reduced by shrinking the separation of the doped fingers: with a reverse applied bias of 6 V it is possible to have an electric field as high as $6.5 \cdot 10^2$ kV/cm with the threshold in Si at around $3.0 \cdot 10^2$ kV/cm. Static characterization of the three-terminal diode had been performed applying equal bias across the two sections. Fig. 2.16 (d) show a breakdown voltage of -6 V, but also a large dark current due to the leakage current from the resistive doped fingers in the multiplication region. This effect is mainly due to misalignment in the doping process and dopant diffusion during the successive epitaxial growth of the Si volume. Regarding the electrooptical characterization, light impulse measurement reveal a 3 dB bandwidth of 18.9 GHz at -6.4 V.

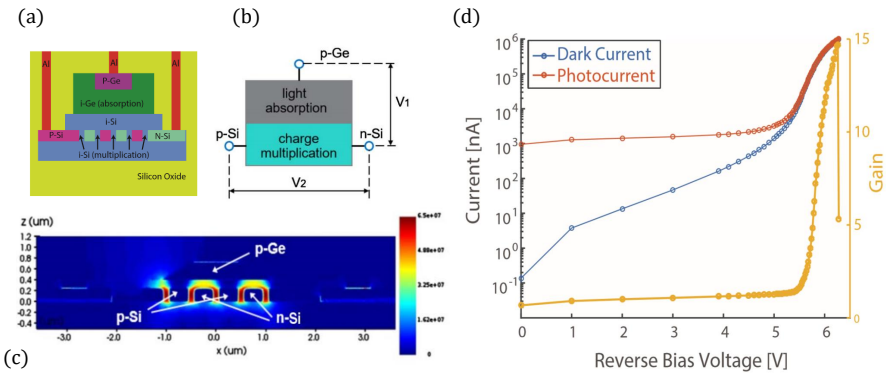

Figure 2.16: (a) Diagram of the low-voltage three-terminal SiGe waveguide APD; (b) Simplified schematic of the three-terminal APD driven by two independent voltage drops across two separate regions; (c) Simulated electric field at the central vertical cross section of the three-terminal APD, with 6 V reverse bias voltages across both the absorption and multiplication regions; (d) Photocurrent and avalanche gain versus reverse bias voltage, showing a breakdown voltage of about 6 V. From [119].

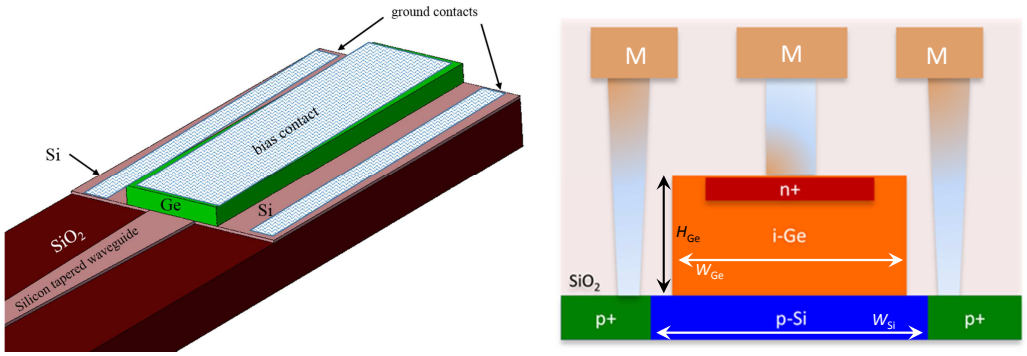

(a) (b)

Figure 2.17: Geometry of a Ge-on-Si waveguide photodetector. (a): 3-D sketch. (b): 2-D cross-section of an n-on-p configuration.

2.3 Novel contributions

In this section, we will present our contributions to the study of Ge-on-Si waveguide-coupled photodetectors. For all the numerical experiments we considered a typical *pin* structure as the one presented in 2011 by DeRose et al. [35]. Briefly, a bulk germanium absorption region is grown on top of a doped silicon layer. Implantation on top of the Ge bulk provides a good ohmic contact. Light is then fed through butt-coupling using an adiabatic tapered waveguide made out of undoped Si, coplanar to the Si layer of the detector. Looking at common values used in literature, the intrinsic Ge layer is 4.0 μm wide and it has a height of 0.8 μm. Regarding the doping levels, a concentration of $N_{A,D} = 10^{18}\,\mathrm{cm}^{-3}$ is used as background doping in the Si n,p-region while a doping level of the order of $10^{19}\,\mathrm{cm}^{-3}$ has been used in the contact regions n^+, p^+; Ge region had been considered intrinsic. At the moment, the Si/Ge heterojunction has been modeled as metallurgically abrupt.

Several ways had been attempted to tackle the simulation of waveguide-coupled photodetectors where the presence of both optical and electrical domains demands for a multiphysics approach. It is common practice to decompose the solution of the whole problem in its constituent sub-problems in order to simplify its treatment: the final solution is going to account for the effects of both domains, but it misses eventual couplings between the two domains (e.g. refractive index variations due to the presence of free-carriers).

In a typical application to waveguide-coupled detectors, optical problem is solved using a properly discretized version of Maxwell's equations with initial condition set to the fundamental mode of the input waveguide. After the simulation, electric and magnetic fields are post-processed to obtain the main quantities of interest:

- power flow of electromagnetic power across the whole guiding structure obtained from the real part of the time-averaged Poynting vector. Looking at its distribution, we gain few insights on the actual propagation, highlighting eventual weaknesses of the coupling solution;

- amount of electromagnetic power deposited in the absorption region computed from the divergence of the Poynting vector. The distribution of absorbed power is strictly related to the optical generation rate $G_{opt}(x, y, z)$: from it a series of "compact" informations can be extracted like integral averages across the transverse direction $\tilde{G}_{opt}(z)$ to easily compare different coupling strategies.

Dealing with optoelectronic devices, the information about the optical generation from the optical solver is passed down to the electrical simulator where all the static and dynamic characterizations, in dark and under illumination, can be performed. Further degrees of freedom can be explored including the transport model adopted (e.g. Monte Carlo transport) and the actual description of the semiconductor detectors (e.g. physical simulation of the detector's growth).

Across literature reports, finite-difference time domain (FDTD) technique is the preferred tool for the solution of the electromagnetic propagation problem thanks to its flexibility and the ease of interpretation being a time domain technique. Such technique had been largely used to study the transfer of light to the absorption region both as an exploration or as validation tool in case of analytical/semi-analytical approaches as coupled mode theory [20].

If we look to the electrical problem, drift-diffusion is the mainstream approach with few exceptions involving Monte Carlo simulation to study single-photon avalanche photodiodes (SPADs) [117]. Another not-so-rare option is the use of process simulation to include realistic doping profiles using a Monte Carlo ion implantation technique calibrated through experiments like secondary ion mass spectroscopy (SIMS) [24, 78].

Following literature, finite-difference time domain (FDTD) technique is adopted to study the propagation of the fundamental TE mode from the rectangular input waveguide. Boundary conditions includes perfectly-matched layers (PMLs) on the computational box while all the materials in the box are treated as dispersive, metals included. Drift-diffusion had been employed to describe the electronic transport. To model the semiconductor materials, Fermi-Dirac statistics had been employed together with Shockley-Read-Hall (SRH), radiative and Auger recombination processes. Velocity saturation and doping-dependent mobility have been accounted including Canali and Masetti models: the former describes in a monotonic way (i.e. no velocity overshoot) the transition between low-field mobility and the high-field saturated velocity; the latter fits the reduction in the carrier mobility for increasing values of the dopant concentrations. Heterointerfaces are treated by inclusion of additional thermionic current contributions. Multi-physics coupling between the

two systems is achieved through a one-way linking strategy: from the solution of the optical problem, we obtain the optical generation profile G_{opt} which is passed down to the drift-diffusion electrical solver where it appears in the charge continuity equations for electrons and holes.

2.3.1 Review of the material parameters

Table 2.1 reports the most relevant physical parameters used in the simulations: the energy gap E_g, the electron affinity χ and the relative dielectric permittivity ϵ of silicon and germanium, along with the parameters governing the field- (Canali) and doping-dependence (Masetti) of electron and hole mobility $\mu_{n,p}$.

Together with a review of the electrical parameters, we revised the absorption spectrum of common materials in integrated optics with particular care for germanium. While there is a general agreement between the bulk and thin-film absorption profile of Ge at 1.31 μm, it is observed experimentally a much higher absorption at 1.55 μm in the thin-film Ge compared to the bulk semiconductor [56, 32, 106]. Such enhancement especially at longer wavelengths in the absorption is often explained in terms of the residual tensile strain, from to the Si/Ge lattice mismatch, cumulated typically in the cooling phase of the Ge-on-Si heteroepitaxy.

Table 2.1: Material parameters of Si and Ge used in the present simulations [100]

Parameter	Si		Ge	
E_g, eV	1.12416		0.6638	
χ, eV	4.0727		4.0	
ϵ	11.7		16.2	
	n	p	n	p
$\mu_{0,i}$, cm^2/s/V	1417	470.5	3900	1900
β	1.109	1.213	1.109	1.213
$v_{sat,0}$, 10^7 cm/s	1.0700	0.837	0.743	0.743
$\mu_{min,1}$, cm^2/s/V	52.2	44.9	60	60
$\mu_{min,2}$, cm^2/s/V	52.2	0	0	0
μ_1, cm^2/s/V	43.4	29	20	40
P_c, cm^{-3}	0	9.23×10^{16}	10^{17}	9.23×10^{16}
C_f, cm^{-3}	9.68×10^{16}	2.23×10^{17}	8×10^{16}	2×10^{17}
C_s, cm^{-3}	3.34×10^{20}	6.10×10^{20}	3.34×10^{20}	10^{16}
α	0.68	0.719	0.55	0.55
γ	2.0	2.0	2.0	2.0

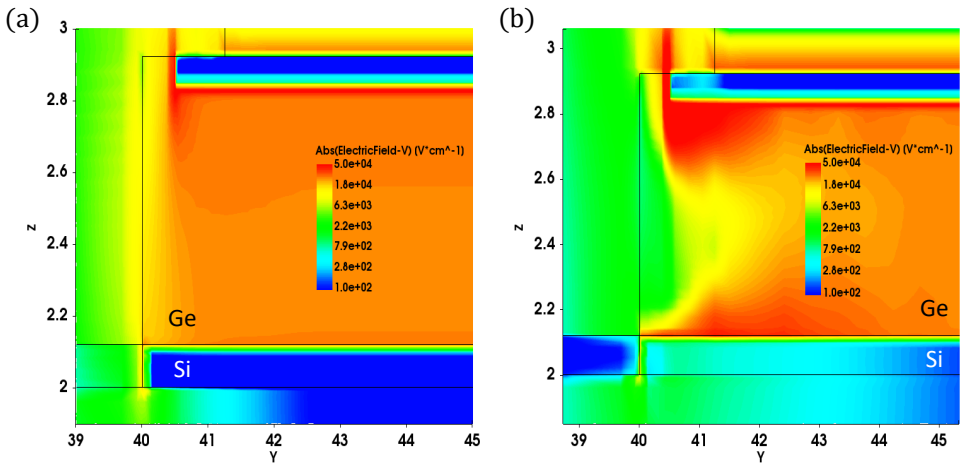

Figure 2.18: Map in a longitudinal cross-section of the magnitude of the electric field E at 1.5 V bias voltage and under illumination at 1 μW (left) and 2 mW (right) of input optical power.

2.3.2 Effects of saturation velocity

Owing to the micrometer dimension of the germanium region, it is possible to develop electric fields on the order of several tens of kV/cm even for small applied bias. Such fields may easily drift the free carriers at their saturation velocity where the usual proportionality between electric field and carriers' velocity condensed by a constant mobility may be an over-simplification.

Using three-dimensional numerical simulations, we simulated a *p*-on-*n* *pin* photodetector under illumination at 1.31 μm input wavelength and two extremal values of input optical power (1 μW and 2 mW) in order to evaluate the impact of field-dependent mobilities on its dynamic response.

Fig. 2.18 report maps of the magnitude of electric field in a longitudinal cross section computed at 1.5 V reverse bias in dark and under illumination. A corresponding map for the carrier velocities obtained had been reported in Fig. 2.19.

What we observe under illumination, owing to the strong absorption of germanium at 1.31 μm, is an abundant optical generation which is concentrated in the first few microns. These carriers screen the electric field resulting from the applied bias, reducing the extraction efficiency and thus limiting the response.

From the knowledge of the DC operating point, electrooptical small-signal analysis of the photodiode is performed comparing the results from constant and field-dependent mobility models. In Fig. 2.20 the results are compared for different input optical power. A constant mobility will produce unphysically high carrier velocities resulting in extremely large bandwidths (i.e. $\approx$ 220 GHz). On the other hand, by using an high-field correction accounting for the velocity saturation of carriers in the Ge absorber, a realistic values of the cut-off frequency can be attained (i.e.

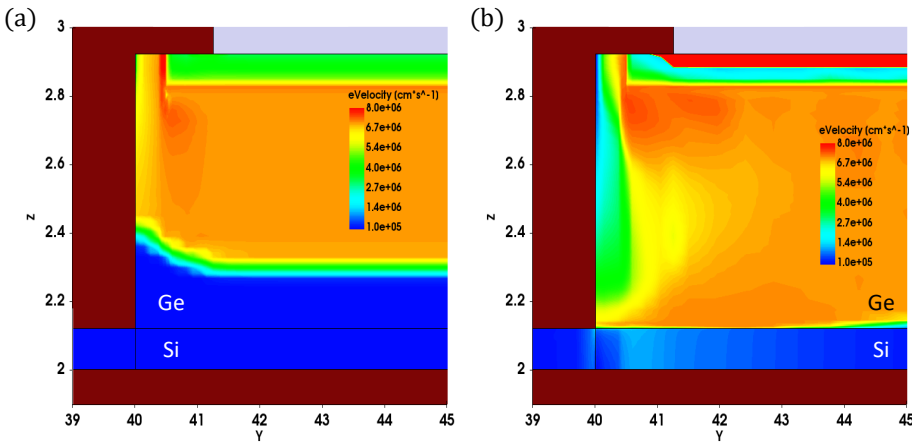

Figure 2.19: Map in a longitudinal cross-section of the magnitude of the electron velocity $v(E)$ at 1.5 V bias voltage and under illumination at 1 μW (left) and 2 mW (right) of input optical power.

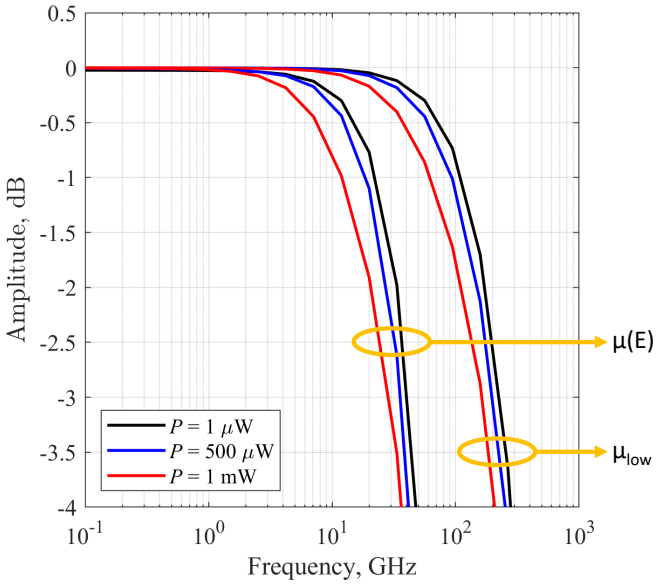

Figure 2.20: Calculated electro-optical bandwidth of the reference *pin* structure at 1.5 V reverse bias and at 1.31 μm for different values of input optical power using a constant and a field-dependent model for the carrier mobilities

$\approx$ 40 GHz).

2.3.3 Realistic description of the Si/Ge heterostructure

The computer-aided design and optimization of Ge-on-Si *pin* waveguide photodetectors is usually performed in a multiphysics fashion. Main metric in the evaluation of such high-speed devices is the electrooptical cut-off bandwidth which may range in the range of tenths of GHz [55].

Fig. 2.21 compares the calculated electrooptical response of the geometry described above in the *n*-on-*p* (solid curves) and *p*-on-*n* (dashed curves) configuration for three different values of optical power at 1.5 V reverse bias. The numerical results relative to the *p*-on-*n* detector are compatible with experiments; e.g., the 3 dB cut-off frequency reported in [113] is 28 GHz at 2 V and 42 GHz at 4 V. On the other hand, the cutoff frequency of the *n*-on-*p* response is significantly lower even for very low optical power, and degrades dramatically for increasing illumination intensity. This is in clear disagreement with the literature, where *n*-on-*p* devices having bandwidths larger than 35 GHz at 1.5 V have been demonstrated [35], and suggests the presence of modelling issues in the *n*-on-*p* configuration.

Deeper insights on these problems can be gained from a comparison between the *n*-on-*p* and *p*-on-*n* band diagrams at thermodynamic equilibrium, which are reported in Fig. 2.22.

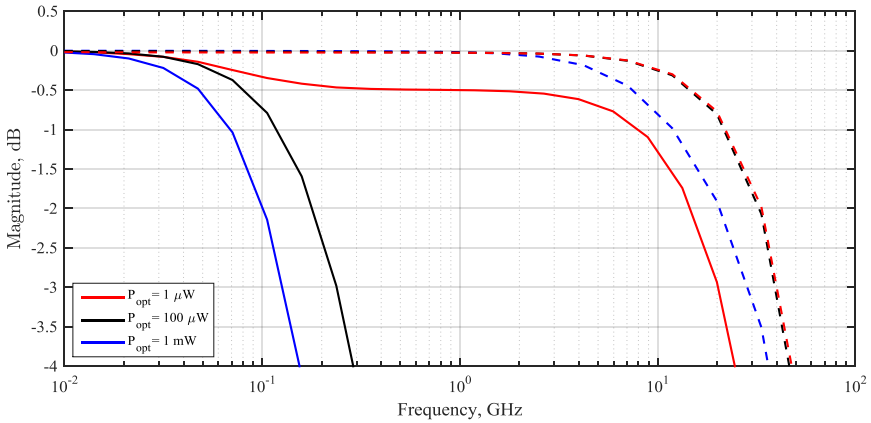

Figure 2.21: Electrooptical response of a n-on-p (solid curves) and a p-on-n (dashed curves) waveguide photodetector reverse-biased at 1.5 V. Red, black and blue curves were obtained with $P_{\mathrm{opt}} = 1\,\mu\mathrm{W}$, $10\,\mu\mathrm{W}$ and 1 mW, respectively.

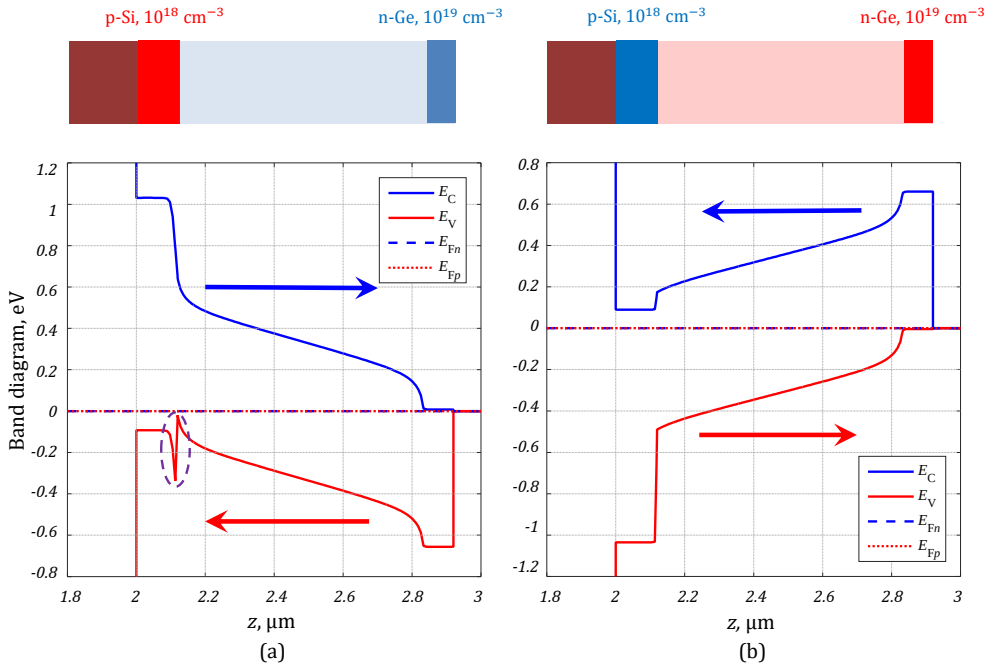

Figure 2.22: Band diagrams of the n-on-p (a) and p-on-n (b) waveguide photodetectors at thermodynamic equilibrium. The arrows show the flow directions of photogenerated electrons (blue) and holes (red). On top of each plot, a schematic representation with materials and doping levels of the vertical cross-section is shown.

As previously stated, a large valence band discontinuity at the Si/Ge heterointerface can be noticed, which can be estimated as $\Delta E_{\mathrm{V}} \simeq -0.533\,\mathrm{eV}$ through the electron affinity rule [3]. This discontinuity has a very different impact on the two doping configurations, as suggested in Fig. 2.22 by the arrows showing the flow directions of the photogenerated electrons (blue) and holes (red) in reverse bias. In fact, the valence band discontinuity affects transport only in the n-on-p case, where it acts as a barrier preventing holes from leaving the absorption region and determining a carrier build-up that may eventually screen the electric field.

This observation suggests that the n-on-p simulation issues can be addressed by a more realistic modeling of the Si/Ge heterointerface. By recalling that the Ge layer is grown through the two-step epitaxial process, two technological details neglected in the abrupt heterojunction approximation are the prime candidates towards an enhanced structural description. First, the abrupt Si/Ge heterointerface can be replaced with a thin linearly graded $\mathrm{Si}_{1-x}\mathrm{Ge}_x$ transition layer, as shown in Fig. 2.23(a). Second, since the low-temperature Ge buffer layer is usually doped in-situ [35] with an acceptor density comparable to that present in the Si substrate, it may be important to consider that the p doping extends also above the metallurgical Si interface. By comparing the band diagram reported in Fig. 2.23(b) with Fig. 2.22(a) it is clear that this more realistic heterostructure model leads to a mitigated band-offset discontinuity.

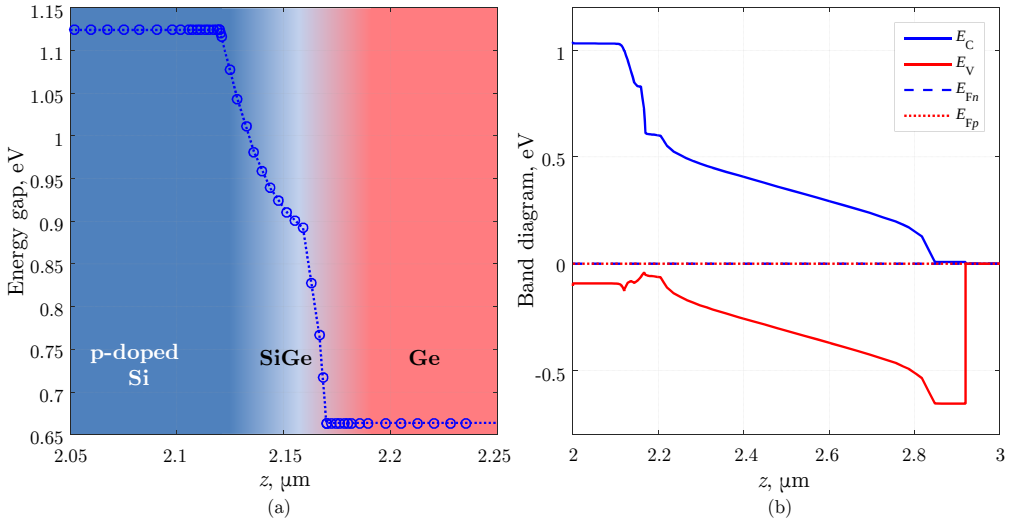

Figure 2.23: (a) Energy gap of the n-on-p waveguide photodetector featuring the enhanced Si/Ge heterojunction model, which includes a thin graded $\mathrm{Si}_{1-x}\mathrm{Ge}_x$ transition layer and takes into account the in-situ p-doping of the Ge buffer. (b) Band diagram of the device described in (a) at thermodynamic equilibrium in dark.

Figs. 2.24 and 2.25 demonstrate that both the graded transition and the p doping must be included in the Ge buffer model under illumination. These figures compare

the band diagrams and the electrooptical bandwidths obtained at 1.5 V reverse bias and $P_{\text{opt}} = 200\,\mu\text{W}$ for different descriptions of the Si/Ge interface region, where t is the thickness of the $Si_{1-x}Ge_x$ layer and d is the extension of the p-doped region in the buffer, both measured from the p-Si top edge. Case (a) corresponds to no model enhancement, i.e., abrupt Si/Ge heterojunction and nominally intrinsic Ge. Its band diagram is almost flattened by carrier build-up and field screening effects, which prevent proper photodetection operation. Similar results are obtained in case (b) for a device with a doped Ge buffer ($d = 100\,\text{nm}$) without any compositionally-graded transition layer ($t = 0$). The electrooptical bandwidths corresponding to cases (a) and (b) in Fig. 2.25 have frequency cutoff lower than 1 GHz. In case (c), the graded transition layer is used ($t = 50\,\text{nm}$), but without doping above Si ($d = 0$). Finally, case (d) includes both enhancements, with $t = 50\,\text{nm}$ and $d = 100\,\text{nm}$. The results of cases (c) and (d) are quite close, as expected, to those of the p-on-n device (see Fig. 2.25 for its frequency response and Fig. 2.24(e) for the corresponding band diagram under illumination).

It should be pointed out that the doped Ge buffer, which may seem to play a rather small role with respect to the graded transition layer from the results of Figs. 2.24(c)–(d) and Fig. 2.25, has an important effect in limiting the sensitivity of the cutoff frequency with respect to the illumination intensity.

As shown in Fig. 2.26(a), the alternative descriptions of the Si/Ge heterointerface do not have a significant impact on the calculated dark current of the n-on-p structure, which are similar to those of the p-on-n device. (Experimentally observed dark currents [113, 57] are likely dominated by trap-assisted recombination and tunneling mechanisms [7, 75, 111], whose inclusion requires a detailed knowledge of the specific technological processes.) The simulated photocurrents reported in Fig. 2.26(b) as a function of the input optical power demonstrate a substantial agreement in the responsivity between the two doping schemes (0.759 A/W and 0.713 A/W for the p-on-n and the n-on-p case, respectively). However, field screening severely limits the calculated photocurrent of the n-on-p structures if a graded transition layer is not included, since saturation occurs for optical power levels larger than $200\,\mu\text{W}$.

Owing to our interest in reproducing the detector's behaviour under illumination, inclusion of band-to-band tunnelling and/or trap-assisted tunnelling in the simulations has been neglected. Clearly, these effects must be considered when trying to reproduce the dark current characteristics, a task notoriously difficult to perform.

2.3.4 Drift-diffusion vs. energy balance transport

One of the challenges in the simulation of Ge-on-Si avalanche photodetectors is about the accurate modelling of impact ionization phenomena. From literature, we know the functional form for impact ionization is:

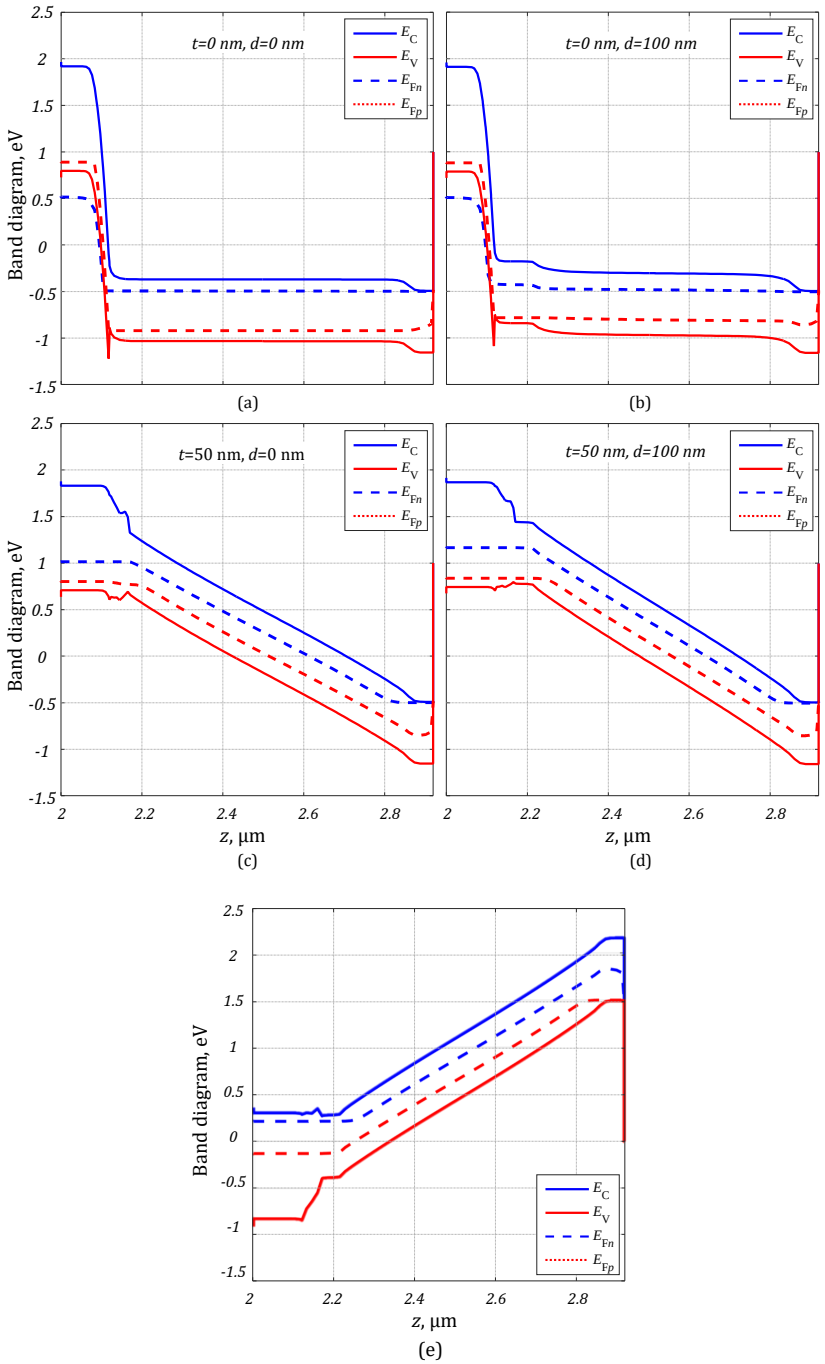

Figure 2.24: Band diagrams obtained at 1.5 V reverse bias with $P_{\text{opt}} = 200\,\mu$W on n-on-p waveguide photodetectors with different descriptions of the Si/Ge heterointerface (a)–(d) and on a p-on-n device (e).

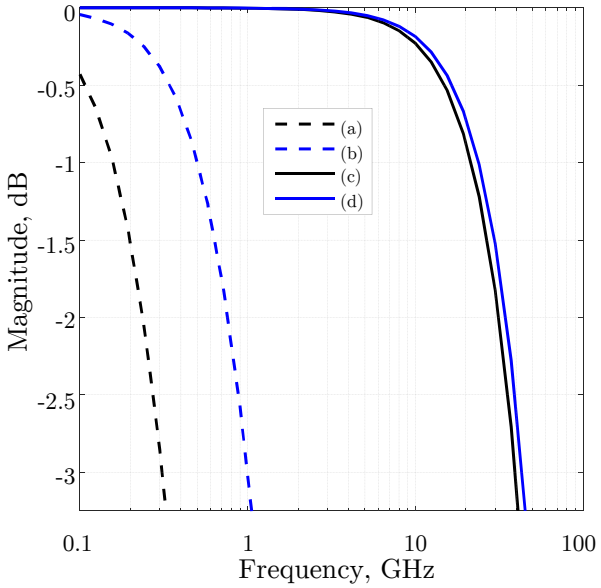

Figure 2.25: Electrooptical response for n-on-p waveguide photodetectors with different descriptions of the Si/Ge heterointerface.

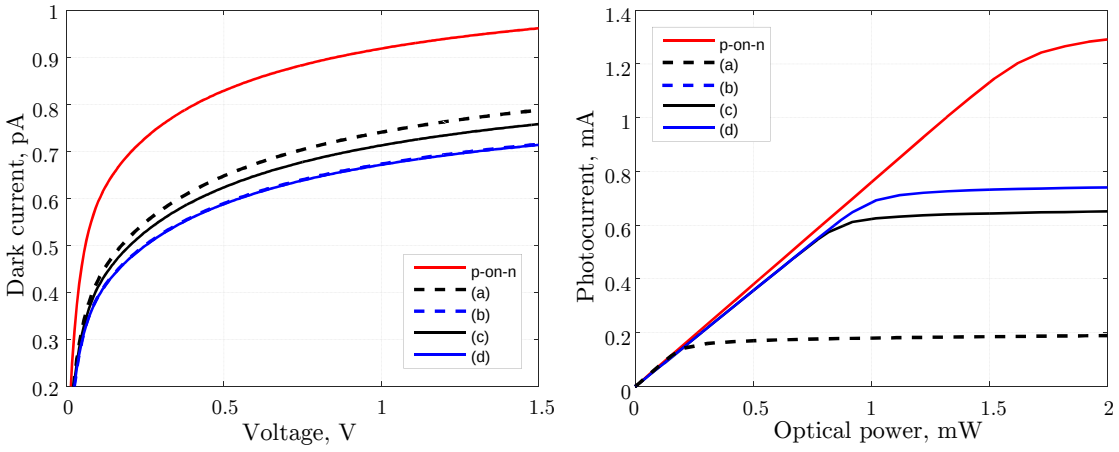

(a) (b)

Figure 2.26: Dark current characteristics (left) and photocurrent vs. input optical power at 1.5 V bias (right) for photodetectors with different descriptions of the Si/Ge heterointerface. The curves (a) and (b) on the right panel are superimposed.

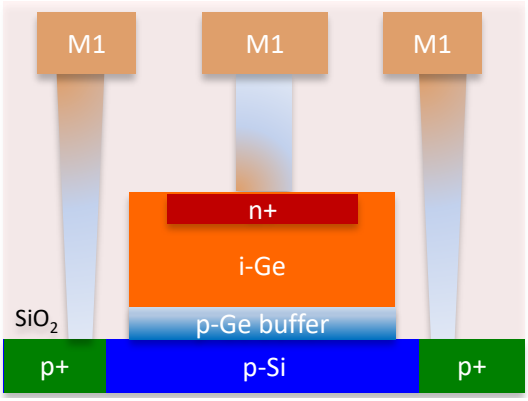

Figure 2.27: Schematic diagram of the n-on-p Ge-on-Si detector under study, including the graded buffer layer.

$$G_{ii} = \frac{1}{q}(\alpha_{\mathrm{n}}(x)|J_{\mathrm{n}}(x)| + \alpha_{\mathrm{p}}(x)|J_{\mathrm{p}}(x)|) \tag{2.4}$$

where $J_{\mathrm{n,p}}(x)$ are the electron and hole current density and $\alpha_{\mathrm{n,p}}(x)$ is the electron and hole ionization coefficient. This last quantity expresses the probability, per unit length, of triggering an ionization event. These coefficients show an exponential dependence on the local electric field which is reported in Chynoweth's law [89], however what they disregard is the actual energy of the carriers. Since impact ionization requires a certain threshold energy, we know from experiments and simulations that carriers may travel for distances on the order of fractions of microns without any multiplication of carriers [87, 88]. With the term *dead space* we refer to the minimum distance needed by the carriers to draw enough energy from the electric field in order to trigger an impact ionization event (on similar consideration, it is possible to define a dead time) [108, 107].

To treat in a natural way the dead spaces in simulations, we could resort to a device simulation based on a Monte Carlo method: what we would gain is a complete picture of the transport problem, but at the cost of an increased computational burden. Another possibility consists in enriching our drift-diffusion model through the higher-order moments of the Boltzmann transport equation (BTE). Beyond Poisson equation and the charge continuity equations (0^{th} moment) from the usual drift-diffusion scheme, these additional equations includes a vector conservation equation for the linear momentum density (1^{th} moment, one equation for each cartesian component) and a scalar conservation equation for the energy density (2^{nd} moment) for the electron and hole gases. Together with the proper closure relations, such a system of equations constitutes the hydrodynamical transport model. In hydrodynamical simulations, mobility and diffusivity are no longer instantaneous local functions of the electric field, but become functions of the spatial distribution

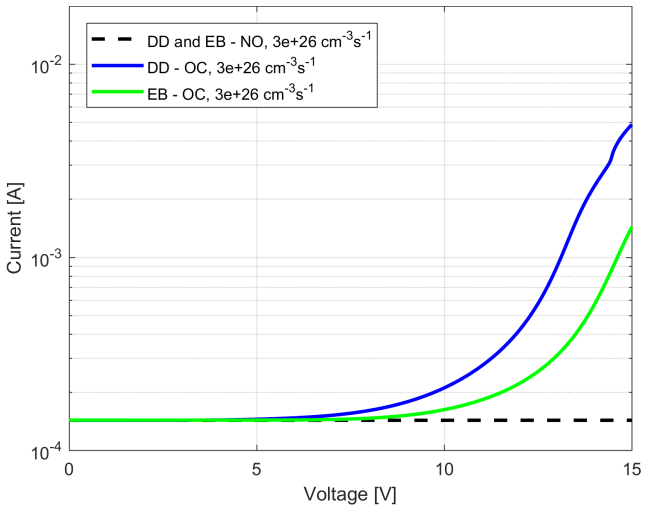

Figure 2.28: Predicted I(V) characteristics for a *pin* waveguide photodetector under illumination using the drift-diffusion (DD, blue) or the energy balance (EB, green) model against a simulation of a non-avalanching device

of the carrier energy. In many cases, this enormous non-linear system of equations may be simplified by considering that the energy of our carriers is much greater than their actual thermal velocity:

$$E_n = \frac{3}{2}k_B T_n + \frac{1}{2}m_n^* v_n^2 \approx \frac{3}{2}k_B T_n \tag{2.5}$$

From this ansatz, we may discard the equations associated to the linear momentum density while retaining the one pertaining to the energy density: such a model is called energy balance. Despite its simplicity, energy balance is probably not a good choice for compound semiconductors such as GaAs or GaN, but has been widely used for Si and Ge (indirect gap, large electron masses) and all its model parameters are reasonably well-established [17].

We performed few simulations of a Ge-on-Si *pin* waveguide photodetector under increasingly high voltage to explore the avalanche behaviour of the device. From the global I(V) characteristic reported in Fig. 2.28, we can notice how energy balance predicts a lower ionization rate with respect to drift-diffusion.

On the microscopic scale, we can observe how the impact generation rate predicted by drift-diffusion is higher than the one from energy balance simulations (Fig. 2.29).

What we observe is also an increase in the current density flowing in the device which results from the applied bias and from the avalanche ionization processes. From the results reported in Fig. 2.30, we can appreciate how different the ionization coefficients are. In fact, assumption of local equilibrium in drift-diffusion leads to

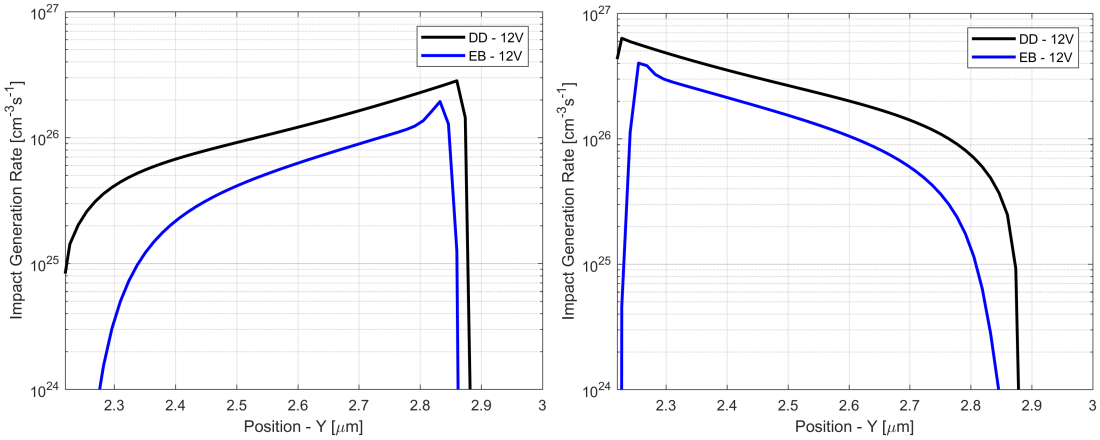

Figure 2.29: Impact generation rate for electron (left) and holes (right) under 12 V of reverse bias

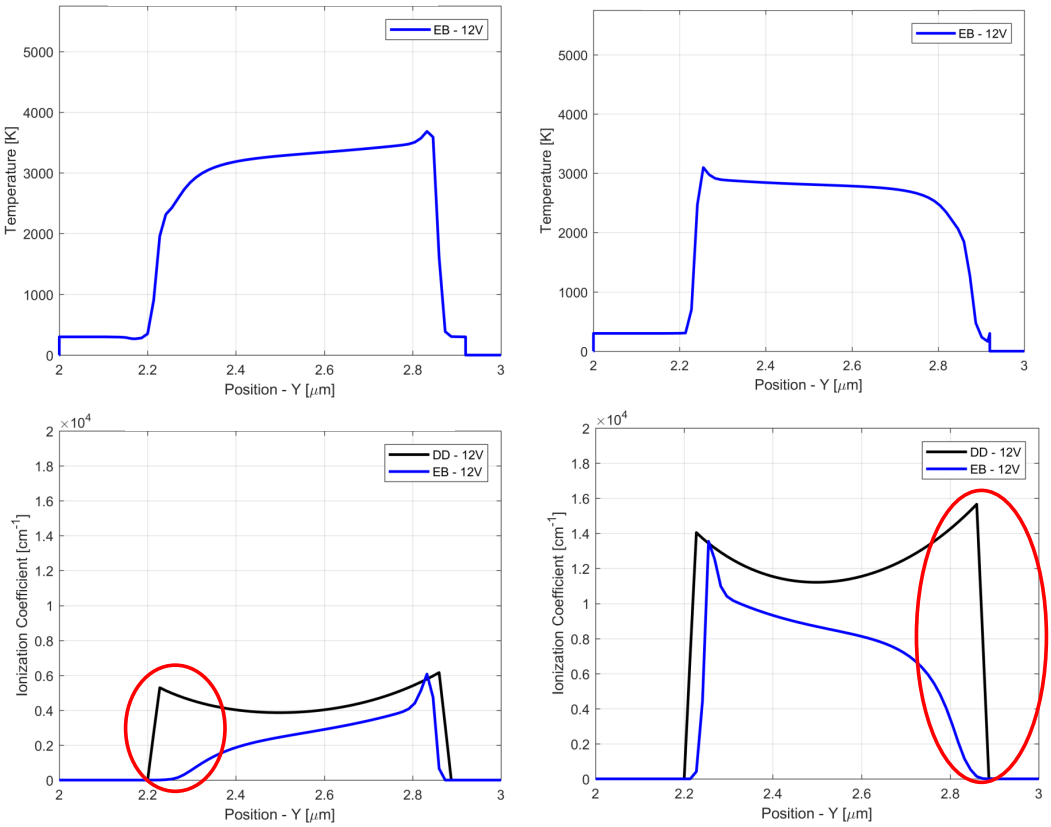

Figure 2.30: Top: electron (left) and hole (right) temperatures from energy-balance simulations. Bottom: comparison of electron (left) and hole (right) ionization coefficient obtained from drift-diffusion and energy balance.

an higher ionization coefficient with a profile resembling the one from the local electric field. On the other hand, with the energy balance model we account for the necessary build-up of the energy that together with the exponential dependence of the ionization coefficient with respect to the carrier temperature, result in a lower avalanche generation.

2.3.5 Innovative optical coupling

As already mentioned in the literature review, a butt-coupling solution as the one employed in the previous *pin* structure may give rise to a large amount of photo-generated carriers. These, in turn, may screen the electric field from the applied bias spoiling the detector's responsivity and the electrooptical bandwidth of our device.

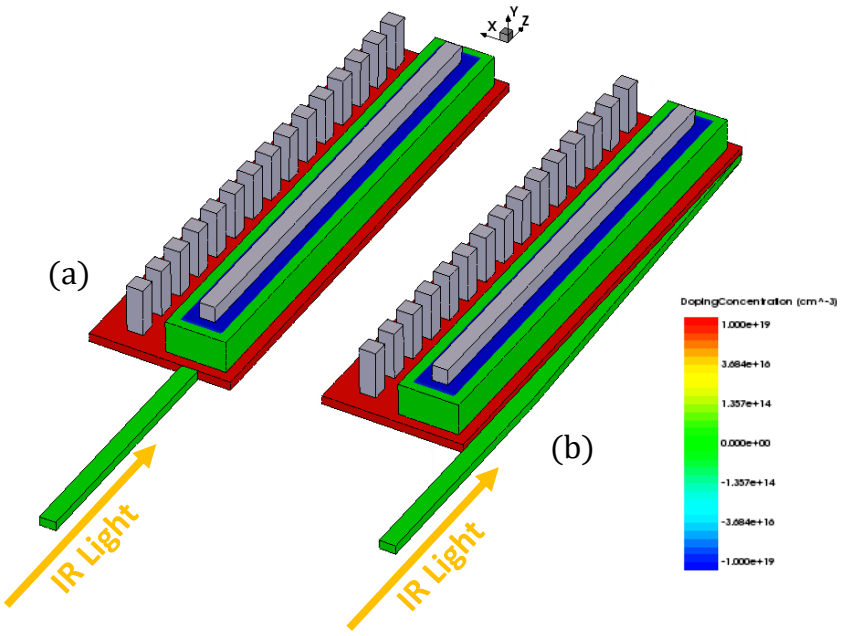

Figure 2.31: Perspective view of the reference photodetector using a butt-coupled (a) and an asymmetric lateral waveguide (b).

Both experiments and simulations suggest to look for a different coupling strategy to better distribute the input optical power in the germanium region. Looking at few examples from literature, we study the effect of an asymmetric coupling structure composed by a triangular tapered waveguide in Si placed sideways the Si base [20]. In Fig. 2.31 we report a perspective view of the two illumination strategies obtained from Sentaurus' geometric modeller.

To assess the efficiency of the new optical coupling solution we perform a series of finite-difference time domain (FDTD) simulations at telecom wavelengths (i.e. 1.31 μm, 1.55 μm) to compute the amount and the distribution of optical power coupled to the Ge region and a drift-diffusion solution for the electrical problem to obtain the relevant figures of merit of the *pin* photodetector (i.e. responsivity, electro-optical bandwidth). Compared to previous optical simulations, we consider an absorption profile measured from epitaxial Ge-on-Si films at 1.55 μm which is almost twice the bulk value [106].

As shown in the colormaps reported in Fig. 2.32 and Fig. 2.33, the butt-coupling solution presents a strong optical generation "plume" in the first few microns of the Ge absorber which is especially evident at 1310 nm. On the other hand, the proposed lateral coupler gives the possibility to distribute more evenly the input optical power to the detector leading to a more uniform distribution of the optical generation rate.

All these considerations may be repeated when looking at the integral mean

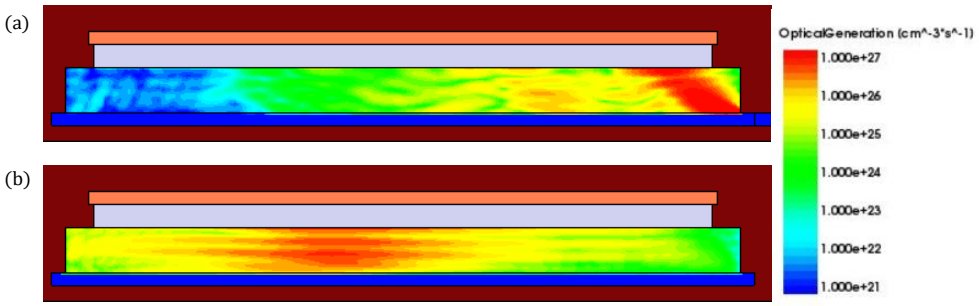

Figure 2.32: Comparison of the optical generation G_{opt} profiles from FDTD simulations at a wavelength of 1.31 μm and input optical power of 200 μW extracted at the middle of the Ge detector region for a butt-coupled (a) and lateral (b) solutions.

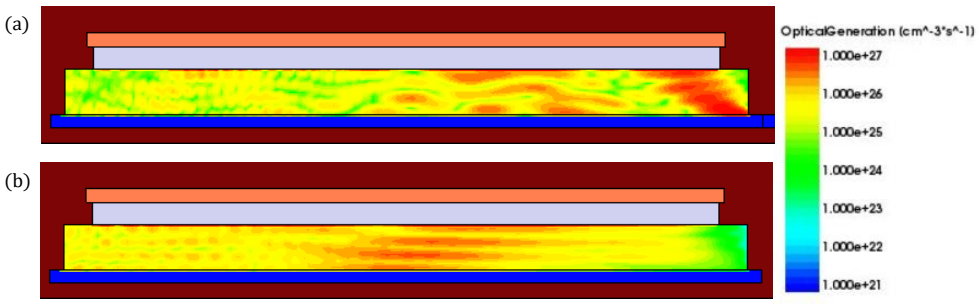

Figure 2.33: Comparison of the optical generation G_{opt} profiles from FDTD simulations at a wavelength of 1.55 μm and input optical power of 200 μW extracted at the middle of the Ge detector region for a butt-coupled (a) and lateral (b) solutions.

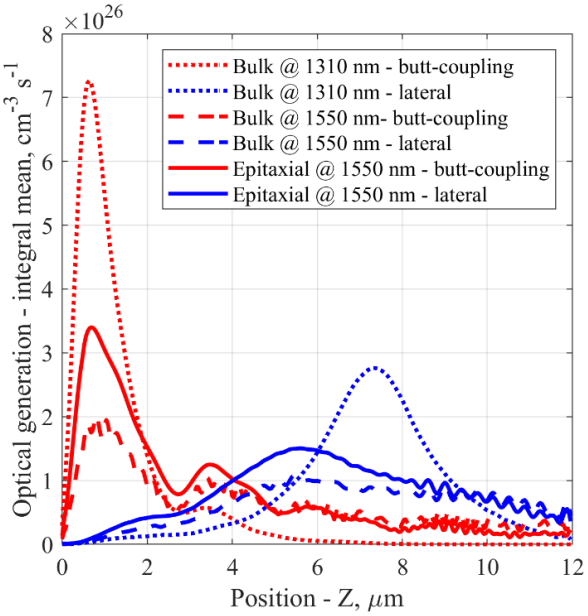

Figure 2.34: Comparison of the computed integral mean optical generation profiles $\tilde{G}_{opt}$ for butt-coupling and lateral solution at 1.31 (reference) and 1.55 μm.

optical generation profile $\tilde{G}_{opt}$ in Fig. 2.34. These profiles have been obtained by integrating the three-dimensional distributions in the detector region in the transverse direction and normalizing the results by the Ge cross-sectional area, with the same spirit of the integral mean theorem. Looking at the curves at 1.31 μm it is easy to appreciate how the lateral coupler shifts the maximum of the distribution toward the middle of the detector, simplifying the collection of carriers. Same behaviour is seen at 1.55 μm despite the distributions are less sharp, being the absorption coefficient for Ge lower.

Talking about the electrical simulations, Fig. 2.35(a) shows a simple comparison of the photocurrents obtained from the computed illuminations with two wavelengths and two optical coupling solutions. Much more interesting is the behaviours of the curves reported in Fig. 2.35(b), where we plot the simulated photocurrent versus the input optical power. At 1.31 μm and for increasing level of the optical power, lateral coupling shows its advantage over traditional solutions by giving to the detector a much higher saturation level. A similar trend is present within the simulation results at 1.55 μm adopting a thin-film absorption. However, such behaviour is in stark contrast with our literature reference where experimental characterizations suggets saturation happens at lower power (e.g. 6 mW for butt-coupling and 18 mW for the asymmetrical coupler). This is also an indication of possible physical aspects, like strain or other defects, which are now missing in our description and that should be kept into account.

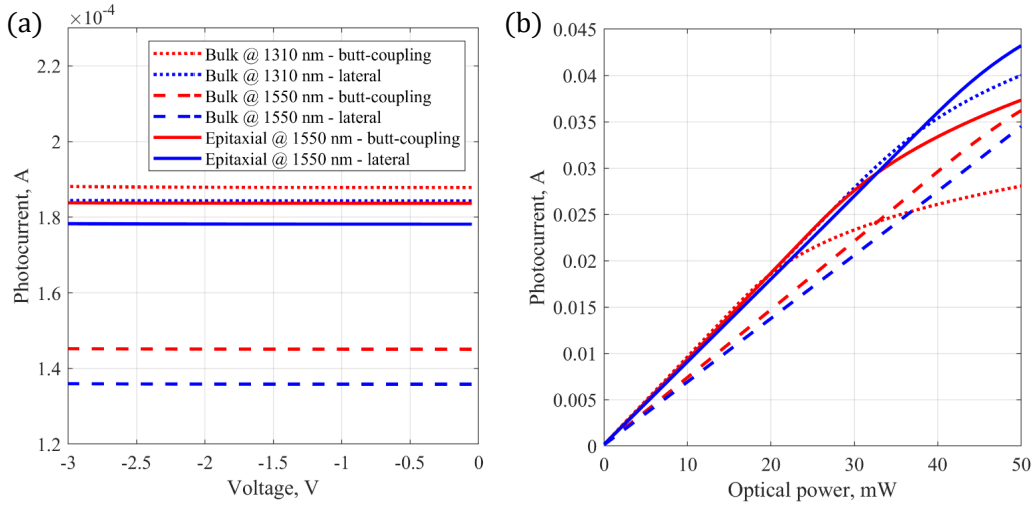

Figure 2.35: (a) Photocurrent vs. applied bias obtained at 200 μW of input optical power and 1.31, 1.55 μm input wavelengths for butt- and lateral coupling strategies (b) Photocurrent vs. input optical power from the same photodetectors lit through a butt- and lateral coupling strategy obtained at 1.5 V applied bias and 1.31, 1.55 μm input wavelength.

2.4 Conclusions

In this chapter, we presented some concepts on photodetectors introducing the different electrical structures such as *pin* and APD with their relative pros and cons. Waveguide-coupled avalanche photodiodes (APDs) are interesting for their enhanced sensitivity but they pose several challenges in the design (e.g. in SAM devices, design of the dose in the charge layer is fundamental for the appropriate shaping of the electric fields) and the simulation (e.g. convergence issues due to avalanche generation since it depends exponentially on the local electric field).

With the aid of a reference structure, we explored the physics governing such devices and gained some insights into their simulations:

- One of the main bottlenecks in the simulation of waveguide-coupled photodetectors is the computation of the optical generation profile. Standard approaches include the finite-difference time domain (FDTD) technique, an accurate but computationally intensive approach: under monochromatic illumination at $\lambda = 1.31\,\mu$m ($1.55\,\mu$m), optical simulation was split over 8 nodes and required about 2h 35m (6h 30m) and around 30 GB of RAM memory. In particular, computational burden easily grows when performing parametric studies (i.e. optimization of the input waveguide). Being the waveguide photodetector an almost longitudinal structure, beam propagation method (BPM) [31, 48, 69] could be an interesting alternative for the solution of the optical problem in order to speed-up the design of the optical coupling structure while leaving FDTD as a design validation tool.

- Despite the results obtained with the energy-balance model, there are some uncertainties on the nature of the derivation and of the closure relations to be used [37], undermining the theoretical framework. Adopting a Monte Carlo technique for the solution of the Boltzmann transport equation would give us deeper insights on the avalanche ionization properties of Ge-based materials and optoelectronic devices.

- It would be of great interest to refine our knowledge on the Si/Ge heterointerface by means of experimental data (e.g. SIMS profile) or semi-empirical models. In fact, the inclusion of technological details such as traps and/or defects is fundamental for an accurate modelling of the dark current.

Chapter 3

Electro-optic plasmonic-organic hybrid modulators

Plasmonics has been defined as the art of generating, processing, transmitting, detecting and sensing signals at optical frequencies along metallic surfaces much smaller than the wavelengths they carry [70]. Since its introduction in the field of integrated optics, plasmonics ushered in new designs for electrooptic modulator characterized by small footprints (total length around 10 μm), high bandwidths ($>$ 100 GHz) and sub-fJ bit energy consumptions. In this chapter we introduce what a modulator is and how it works and, after a brief review of the current state of the art, we show some results on the electromagnetic simulation of a compact plasmonic Mach-Zehnder modulator. Part of the work presented in this chapter will appear in [109].

3.1 Basic concepts

Optical modulators give us the ability to store information within the optical carrier's amplitude and/or phase by means of an electrical signal through a variation of the material's complex refractive index.

Depending on the principle of operation, we may distinguish between electro-absorption and electro-optic modulators. With electro-absorption modulators we act directly on the amplitude of the signal through the optical absorption resulting in intensity variation. On the other hand, electro-optic modulators produces ideally pure phase variation exploiting changes in the refractive index. Eventual intensity modulation in electro-optic modulators may be obtained using interferometric techniques. In both cases, variations of refractive index and absorption are tied together by the causality requirements of the Kramers-Krönig relations.

Absorption modulation can occur in bulk semiconductors exploiting the Franz-Keldysh effect (photon-assisted band-to-band tunneling) or the quantum-confined

Stark effect in design based on quantum wells. In particular, such structures exhibit an higher extinction ratio compared to bulk modulators owing to the more abrupt absorption edge and to the ability to tailor the quantum well's optical properties (through thickness, composition and strain). Common realization within silicon photonics includes Ge/SiGe multi-quantum well, often realized via low-energy PECVD on virtual substrate Si_xGe_{1-x} [68].

Electro-optic modulators may be realized using so-called electro-optic materials in which the applied electric field induces a variation of the refractive index. This phenomenon is directly related to the material's crystalline structure and it can be classified according to the dependence of the variation with the field. We thus find the Pockels effect (linear electro-optic effect) or the Kerr effect (quadratic electro-optic effect). Pockels effect can be found in any crystalline material lacking of the inversion symmetry (i.e. unstrained Si exhibits no electro-optic effect) in the lattice or in poled polymers. Another phenomenon which may ascribed to electro-optic effects is the plasma dispersion [105, 104] obtained through injection or depletion of carriers in the active region of a junction-based device or through carrier accumulation in a MOS structure, making possible the realization of Si-based modulators.

We identify as main figure of merits characterizing the modulator the following quantities:

- static electrooptic response or transmission characteristics $T(V_{in})$ defined as the ratio between the output optical power with respect to the input power as a function of applied voltage

$$T(V_{in}) = \frac{P_{output}(V_{in})}{P_{input}} \tag{3.1}$$

  Typical static response for an electro-absorption modulators is ideally monotonic decrescent, while the response from electro-optic modulators exhibits a periodic behaviour with respect to input voltage and it is minimum in the off-state.

- insertion losses IL defined as the ratio between the input optical power and the output optical power in the on-state

$$IL = 10 \log_{10} \frac{P_{output}(V_{ON})}{P_{input}} \tag{3.2}$$

  It quantifies the penalty due to the presence of the external modulator in the optical system.

- extinction ratio ER which is the ratio between the optical power in the on-state and the optical power in the off-state

$$ER = 10 \log_{10} \frac{P_{output}(V_{ON})}{P_{output}(V_{OFF})} \tag{3.3}$$

- modulation bandwidth which is connected to the maximum bandwidth achievable in the modulation process. Few aspects may reduce the maximum modulation speed: the driving electronics, the velocity mismatch between the electronic and the optical signal and the speed of the physical phenomenon behind the modulation process play.

Aiming to a dense integration of the modulation elements, a lower bound for miniaturization of the external modulator is represented by the total footprint of the device. On one hand, the modulator may be several microns long to ensure proper operation; on the other hand, optical diffraction limits the smallest feature of the guiding elements.

A solution is currently provided by the use of surface plasmon polaritons (SPPs). SPPs are electromagnetic surface waves carried by the interface between a material of negative permittivity and one of positive permittivity; due to this surface wave feature, SPPs can exist independent from the size of the guiding system vs. the operating wavelength, making plasmonic waveguides not diffraction limited.

Despite such promising properties, however, plasmonic waveguides have been for many years in search of a possible killer application. In fact, their use in photonic integrated circuits is fraught with a number of difficulties: from a technological standpoint, most typical IC metals (like Al) have unsatisfactory performances and must be replaced by noble metals like Au or perhaps Ag; even with the best metals, losses are huge (of the order of 0.2-0.8 dB/μm, and therefore long components (interconnects included) are hardly feasible. Electro-optic modulators, however, may be a field where the potential of plasmonics can be conveniently exploited, since the nanometer cross section of plasmonic waveguides allows large electric fields to be obtained also with moderate applied voltages, thus leading to the ability to obtain significant phase modulations over an interaction length of a few μm, not incompatible with the requirements on attenuation.

During the last few years, both Mach-Zehnder and resonant-ring plasmonic modulators have been proposed by a few research groups, with impressive performances in terms of modulating bandwidth but, for the moment, with on-state optical insertion losses that still are too high for practical exploitation (well above 6 dB, against 4 dB of lithium niobate modulators). Last but not least, the use of electro-optic polymers in Plasmonic Organic Hybrid (POH) modulators seems to pave the way to the integration of this component into a Si photonic platform, with expected huge performance advantages compared to all-Si modulators based on the plasma effect.

3.2 Review of the state of the art

Before dwelling into the literature review, it is useful to introduce a couple of key parameters often encountered in the descripton of electro-optic phase shifters and

Mach-Zehnder modulators. A first parameter is related to the materials' electro-optic properties. Altough those effects can be described in terms of second- and third-order nonlinear susceptibilities, mathematical treatment of the electro-optic effect has hystorically relied upon the index ellipsoid which simplifies the treatment of optical anisotropies by parametrizing the electrical energy density U_E in terms of the dielectric displacement vector $\mathbf{D}$ and the inverse of the dielectric tensor ϵ:

$$U_E = \frac{1}{2}\mathbf{E}\cdot\mathbf{D} = \frac{1}{2}\sum_{ij=1}^{3}\frac{1}{\epsilon_{ij}}D_iD_j = \frac{D_x^2}{2\epsilon_{xx}} + \frac{D_y^2}{2\epsilon_{yy}} + \frac{D_z^2}{2\epsilon_{zz}} \tag{3.4}$$

Last equation, which holds in a coordinate system where the dielectric tensor is diagonal, highlights the ellipsoidal shape of these constant energy surfaces. Denoting the elements of the inverse dielectric tensor as $\eta_{ij} = [\epsilon^{-1}]_{ij}$ and and assuming that these values can be expanded as a power series in terms of the applied electric field, we have

$$\eta_{ij}(\mathbf{E}) - \eta_{ij}(0) = \sum_{k=1}^{3} r_{ijk}E_k + \sum_{kl=1}^{3} s_{ijkl}E_kE_l + ... \tag{3.5}$$

where r_{ijk}, s_{ijkl} are the tensors encoding the linear and quadratic electro-optic effect. Focusing on the linear contribution, it is convenient to contract the indexes and to represent the third-order tensor r_{ijk} as a two-dimensional matrix r_{ik}. In fact, being the dielectric tensor symmetric due to recirpocity, also its inverse η and the related electro-optic tensors are found to be symmetric in the first two indexes. The elements of the matrix r_{ik}, the electro-optic coefficients, still depend on the crystal symmetry, further reducing the number of independent elements. In the contracted notation, the variation of the refractive index Δn_i can be expressed as

$$\Delta\left(\frac{1}{\epsilon_i(\mathbf{E})}\right) = \Delta\left(\frac{1}{n_i^2}\right) \approx -2\frac{\Delta n_i}{n_i^3} = \sum_{k=1}^{3} r_{ik}E_k \tag{3.6}$$

where the refractive index variation, approximated with its derivative, is directly proportional to the local electric electric field through the electro-optic coefficients. Consider as a reference the electro-optic properties of lithium niobate ($LiNbO_3$), a material widely employed in electro-optic modulators for long-haul communication systems characterized by a Pockels effect with a linear electro-optic coefficient r_{33} of 30 pm/V. Such value is often used to compare the electro-optic properties of different materials. A second set of parameters characterizes the electro-optic modulators on a device level. Consider for simplicity a symmetric Mach-Zehnder structure, where at the end of the output combiner total phase difference $\Delta\phi$ between the two arms can be expressed in terms of the variation of refractive index

Δn and applied voltage V_{in}

$$\begin{aligned}
\Delta n &= -\frac{1}{2}n^3 r_{33} E \approx -\frac{1}{2}n^3 r_{33}\frac{V}{d}\Gamma_{ovp} \\
\Delta\phi_L &= \frac{2\pi}{\lambda}\int_0^L [\Delta n(V_{in}) - \Delta n(0)]_{L,R}\,\mathrm{d}z = -\frac{1}{2}n^3 r_{33}\frac{V_{in}}{d}\Gamma_{ovp}L = -\Delta\phi_R \\
\Delta\phi &= \Delta\phi_L - \Delta\phi_R \propto \frac{V_{in}}{d}L
\end{aligned}$$

where L is the arm's length, d is the distance between the signal and ground electrodes and Γ_{ovp} is the mode overlap integral between the optical carrier E_{opt} and the electrical RF field $E_{RF|z}$ over the cross-section of the arm's waveguide

$$\Gamma_{ovp} = \frac{d}{V_{in}}\frac{\int\int |E_{opt}(x,y)|^2 E_{RF|z}\mathrm{d}x\mathrm{d}y}{\int\int |E_{opt}(x,y)|^2\mathrm{d}x\mathrm{d}y} \tag{3.7}$$

At this point, we can identify the on-state (off-state) whenever there is a phase difference of 0 (π) radians inducing constructive (destructive) interference phenomena

$$\begin{aligned}
\Delta\phi = 0 &\propto \frac{V_{ON}}{d}L \rightarrow V_{ON} = 0\,\mathrm{V} \\
\Delta\phi = \pi &\propto \frac{V_{OFF}}{d}L = \frac{V_\pi}{d}L
\end{aligned}$$

Of the two expressions, we can see how the $V_\pi L$ product enters the definition of the off-state voltage. This quantity is a useful indicator of the modulator's performance where highly-performant devices are characterized by small V_π (low voltage drive and low-energy consumption) and small L (area occupation). At this point, we are now ready to review the results presented over the past years.

The main research line on plasmonic electro-optic modulators leading to experimental realizations was initiated in 2014 through the cooperation of a number of research groups (from the Karlsruhe Institute of Technology - KIT, ETH Zurich, IMEC and GigOptix). In the seminal paper [81] published in 2014, the first block of a plasmonic Mach-Zehnder modulator was presented, i.e. a plasmonic phase modulator based on an electro-optic linear polymer (Pockels effect with maximum estimated EO coefficient of 70 pm/V after poling) integrated into a SOI platform with a 2 μm SiO_2 thick layer.

The phase modulating device proposed in [81] was developed in two generations, denoted as 1stG and 2ndG. The 1stG device has a length of 34 μm and a slot width of 140 nm, with a signal-ground-signal configuration; the 2ndG device has a length of 29 μm and a slot width of 120 nm, with a signal-ground configuration. The operating wavelength is 1550 nm and stable operation has been demonstrated up to 85°C . The structure is shown in Fig. 3.1 while a photograph of the realized phase modulator is presented in Fig. 3.2 (1stG device). The $V_\pi L$ product is not specified

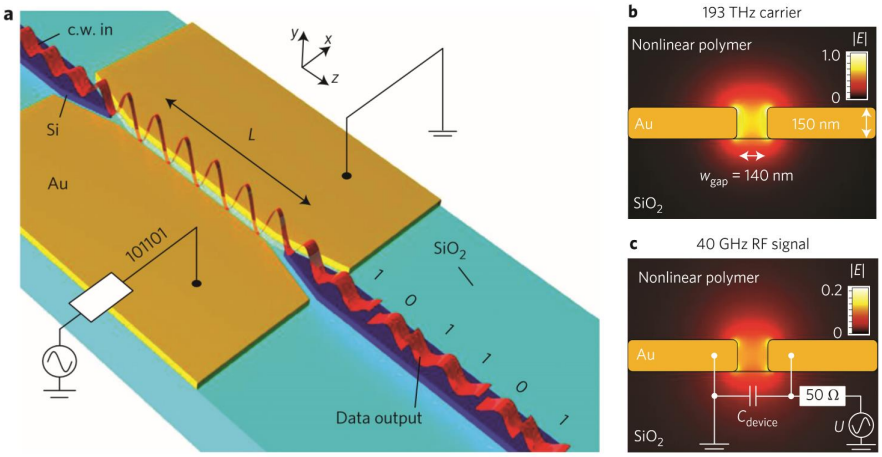

Figure 3.1: (a) Schematic of the Plasmonic Phase Modulator in [81]. A continuous-wave (c.w.) infrared beam guided by the upper-left silicon waveguide (in blue) is coupled through a metal taper to the plasmonic slot waveguide. The slot between the metal sheets is filled with an electro-optic polymer; the phase of the surface plasmon polariton (SPP), which propagates in the slot, is changed by applying a modulating voltage. A second taper transforms the plasmonic mode back to a photonic mode in the lower-right waveguide. (b) and (c) Mode profiles of the plasmonic (b) and RF (c) signals, showing the colour-coded modulus of the complex electric-field vector. The slot width is 140 nm. From [81, Fig. 1].

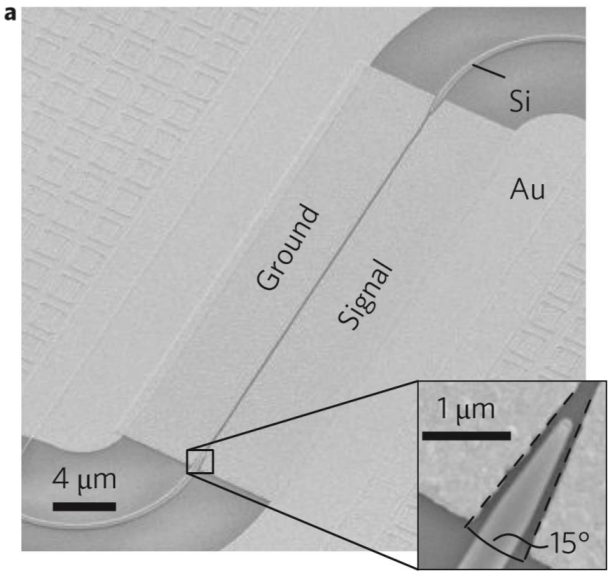

Figure 3.2: Photograph of the Plasmonic Phase Modulator in [81]. From [81].

but it is stated that enough phase modulation can be obtained with modulator lengths lower than 50 μm. The structure was experimentally demonstrated showing BPSK modulation up to 40 Gbps.

Starting from 2015, a number of papers were published by the research groups at ETH Zurich, sometimes with KIT researchers, IMEC researchers and University of Washington researchers in chemistry. On the basis of the phase modulation plasmonic strategy in [81], a number of Mach-Zehnder polymer-based plasmonic modulator designs were proposed, realized and characterized. The results obtained are quite outstanding in terms of modulation bandwidth and energy efficiency per bit, while optical insertion losses appear to be significantly larger than in other modulation solutions, at least with devices designed for integration within a photonic platform (i.e., fed by a photonic integrated waveguide).

A first MZ modulator design was proposed in [82] including two parallel phase modulators in a Ground-Signal-Ground configuration, see Fig. 3.3. The Si photonic platform was based on a SOI system with a 220 nm silicon layer on top of a 2 μm dioxide layer. To access the modulator Si photonic waveguides were used with a 450 $\times$ 220 nm cross section. The MZM exploits a symmetrical configuration with plasmonic slots of width equal (nominally) to 150 nm; the electrode width is 7 μm and the modulator is electrically fed through a coplanar waveguide taper, somewhat similar to a traveling wave configuration but in fact loaded by an open circuit, so that the modulator can be electrically modelled by a capacitor with a capacitance between 1.5 and 3 fF, depending on the device length (L = 19, 29, 39 μm). The input splitter is a waveguide Y junction while a multi-mode interferometer (MMI) output combiner is used. The metal exploited is Au, while the slots are filled by an EO poled polymer. In the POH PMs, the slot is filled with YLD124/PSLD41(25:75 wt.%) mixture which has been shown to provide a record EO coefficient of $r_{33} = 230$ pm/V [90]. In the POH MZM, the EO material SEO100 (from Soluxra, LLC) was exploited because of its excellent thermal stability up to 85 °C. Concerning performances, the 29 μm device was shown to allow for the best compromise between insertion loss and extinction ratio, with a $V_\pi L$ product of 450 V$\cdot\mu$m (notice however that no quantitative result on the ER is given); the device is shown to generate 30, 35 and 40 Gbps OOK modulation with energy in the range 75 - 225 fJ/bit and BER $< 6\times10^{-4}$. As already recalled, a problem of the device is the insertion loss, amounting to 27...34 dB according to device length; 14 dB of this loss are caused by the silicon grating couplers, MMIs, and waveguides; the on-chip insertion loss of the phase shifter (PS) hence amounts to 13...20 dB, depending on its length. The PS frequency and wavelength response is shown in Fig. 3.4; a modulation bandwidth in excess of 60 GHz can be observed. Some interesting comments in [82] concern the asymmetry effects in the modulator structure arising from the slot disuniformity and the possible different alignment of the input and output optical tapers.

A different, more compact layout was presented in August 2015 by Haffner et

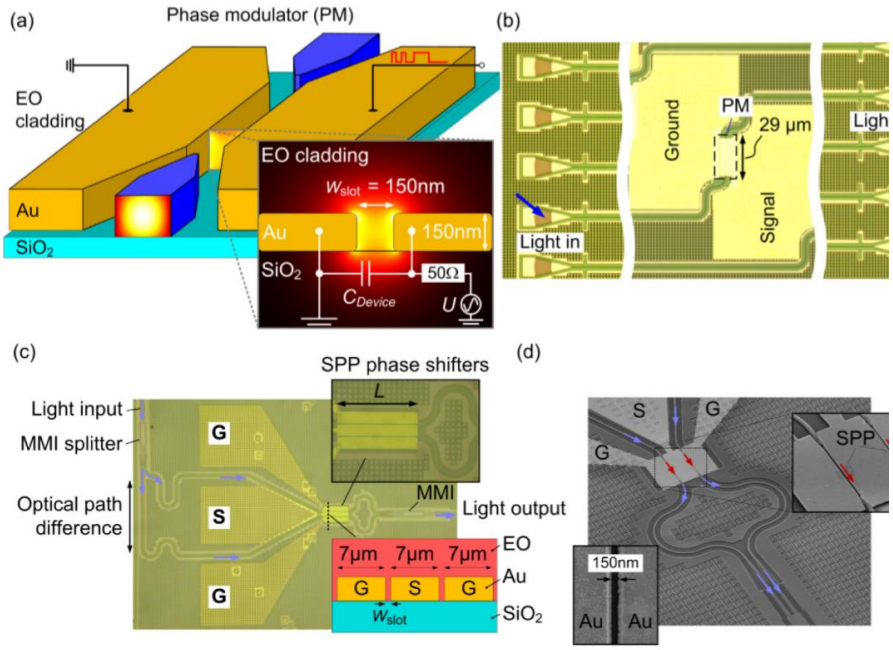

Figure 3.3: Plasmonic-organic hybrid (POH) phase modulator (PM) and Mach-Zehnder modulator fabricated on the silicon-on-insulator (SOI) platform. (a) POH PM including a slot waveguide filled and clad with an electro-optic (EO) material. The photonic mode of a silicon nanowire waveguide is converted to a plasmonic mode through a tapered silicon waveguide. The inset shows a cross section of the device with the optical modal field. (b) Microscope photograph of the fabricated POH PM. Light is launched in and out of the silicon waveguide via diffraction grating couplers. The phase of the optical signal is modulated in the plasmonic modulator section having a length of 29 μm. (c) Optical microscope image of the fabricated MZM. (d) Scanning electron microscope (SEM) picture of the silicon-plasmonic MZM. The modes of the silicon waveguide are coupled to the plasmonic phase PM sections, which modulate the phase of the SPPs. From [82, Fig. 1].

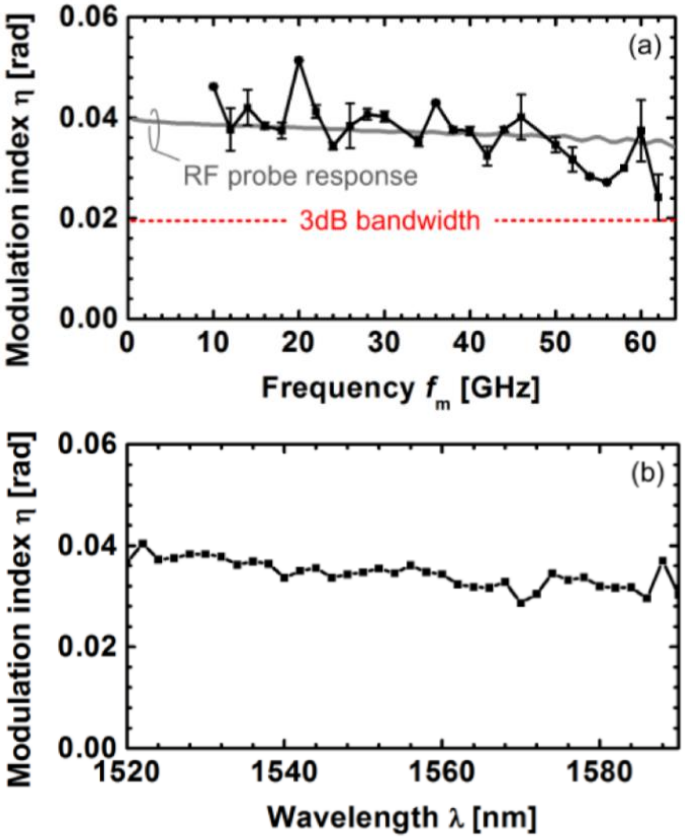

Figure 3.4: Electro-optic response of a PM with $L = 29$ μm. (a) Modulation index as a function of the modulating frequency for a sinusoidal RF modulation signal. The RF power is -10 dBm for a 50 Ω terminating resistor. The black solid line gives the mean of two consecutive measurements, and the error bars indicate the difference between the two. For comparison, the grey solid line shows the transfer function of the coplanar probe from its coaxial input to the probe output as taken from the data sheet. The vertical scale is adjusted to show that for the higher frequencies the drop in modulation index is also due to the frequency response of the probe. The estimated 3dB bandwidth of a MZM comprising the plasmonic PMs is indicated as a red dashed line. (b) Modulation index versus the optical carrier wavelength in a wavelength range of 70 nm for the modulating RF $f_m = 40$ GHz. From [82, Fig. 2].

al. [38], with > 70 GHz modulation bandwidth, 10 μm total length (with a phase shifter length of 5 μm) and a low energy consumption of 25 fJ/bit. The $V_\pi L$ product is as small as 60 V·μm. The phase shifters were designed as MIM plasmonic slot waveguides formed by gold contact pads and a gold island, with the island contacted through a suspended bridge; the slots were filled with DLD-164, a highly nonlinear organic material. The MZM layout and dimensions are shown in Fig. 3.5, while the structure and the power-voltage simulated and experimental curves are reported in Fig. 3.6. From the simulation, an electro-optic coefficient for the EO polymer was estimated as $r_{33} = 180 \pm 20$ pm/V. The operating wavelength is 1534 nm. The access Si waveguides have a cross section of 220 × 450 nm and the plasmonic slot layout is asymmetric, with slot widths of 100 and 90 nm, respectively, with slot thickness of 200 nm. Notice that, due to the asymmetry of the slot widths (90 and 100 nm, respectively), the plasmonic phase velocities will be different in each slot also at zero applied field; as a result, as shown in Fig. 3.6, below, the modulator operates at zero bias close to the half-power point, i.e. with a zero-bias phase shift around $\pi/2$ between the two arms.

The on-off voltage is close to 10 V and the extinction ratio is difficult to estimate due to the limited range of the measurements. A numerical estimate based on 2D simulations for the ER is 26 dB, see [39, Fig. S1 (c)], while an experimental value of 6 dB is suggested, but with reference to a ±3 V swing versus the half power bias point, see [38, Fig. 1b], also reported in Fig. 3.6, below. The experimental modulator optical insertion loss is 8±1 dB, partly due to the couplers, partly to the plasmonic loss of 0.4 dB/μm. The measured modulation bandwidth is in excess of 70 GHz and the modulator was shown to be effective for encoding signals at 54 and 72 Gbps with a BER of 7.3×10^{-5} and 3×10^{-3}, respectively. Some comments are in order on the electrical characterization of the modulator; the bridge capacitance and resistance are estimated as 2.8 fF and 0.36 Ω, respectively. This would lead to a modulation bandwidth in excess of 1 THz in concentrated form; however, the input electrical pad capacitance and resistance make the total C and R the device input equal to an estimate of 32.6 pF and 0.87 Ω, respectively, see [39, p. 14], leading to a 3 dB cutoff of 96 GHz. This bandwidth limitation can be removed by optimizing the the layout of the electrical modulator input, so as to achieve THz bandwidths close to the intrinsic bandwidth of the modulator. The layout and equivalent circuit of the modulator are shown in Fig. 3.7.

On the basis of the compact layout in [38], always in 2015 an IQ ultra-compact modulator was proposed in [41]. The main variation is in the different approach to splitting the input optical power and coupling it with the plasmonic waveguide, see Fig. 3.8, and the reduced slot thickness (150 nm). The devices have shown the ability to encode QPSK and 16-QAM modulation formats with power consumption as low as 27 fJ/bit at 18 Gbps-16QAM.

The research published in 2016-2017 showed some consolidation of results but also the intention to keep under development several device designs, of different

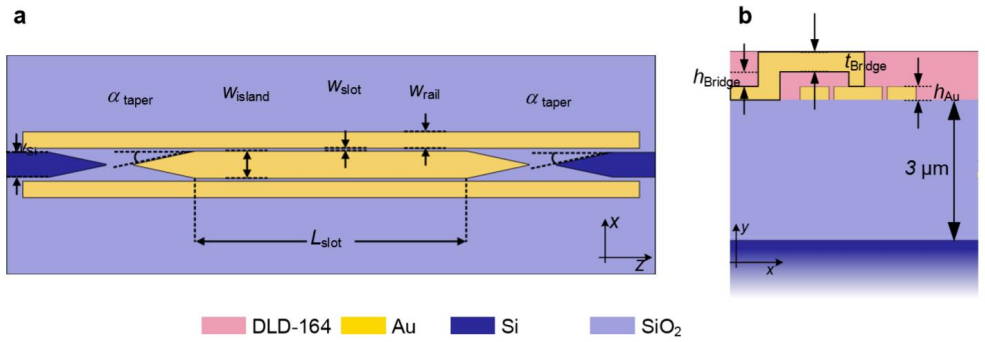

Figure 3.5: Above: Top view, (a) and cross section, (b) of the plasmonic Mach-Zehnder modulator in [38]. The different colors corresponds to the different materials. Below: geometrical parameters of fabricated device. From [39, Fig. S 5 and Table S 1.].

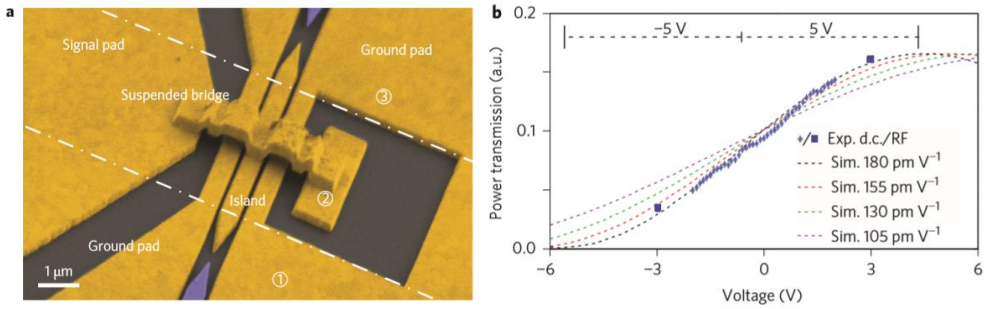

Figure 3.6: Plasmonic circuit realizing the Mach–Zehnder modulator (MZM) from [38]. (a) Colorized SEM image of the MZM components. The suspended bridge enables electrical control of the device. (b) Measured (symbols) and simulated (dashed lines) optical power transfer function versus applied voltage. The simulations indicate a best fit for a material with a nonlinear coefficient of 180 pm/V. From [38, Fig. 1].

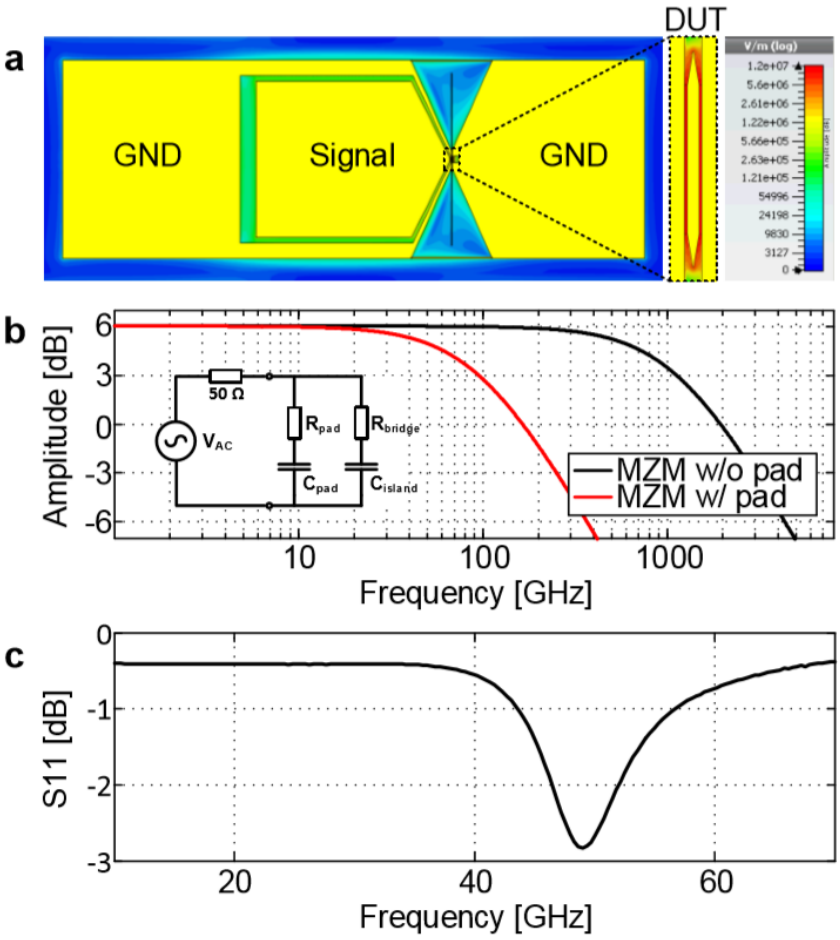

Figure 3.7: Electrical characterization of the modulator in [38]. (a) Numerical calculated electrical field for the modulator and the contact pads (GND-Signal-GND). The signal pad is integrated into the left contact pad (GND) as for reasons of the used GSG-probes. This results in a large pad capacity as can be seen by the electrical field distribution. The influence of the contact pad capacity on the electrical bandwidth is shown in (b); without pads (black) a bandwidth in the THz range is predicted, while with pads the 3 dB cut off is 96 GHz. (c) The electrical reflection coefficient S_{11} shows a dip at 50 GHz, related to the asymmetric contact pads and is not caused by the modulator itself. From [39, Fig. S 7].

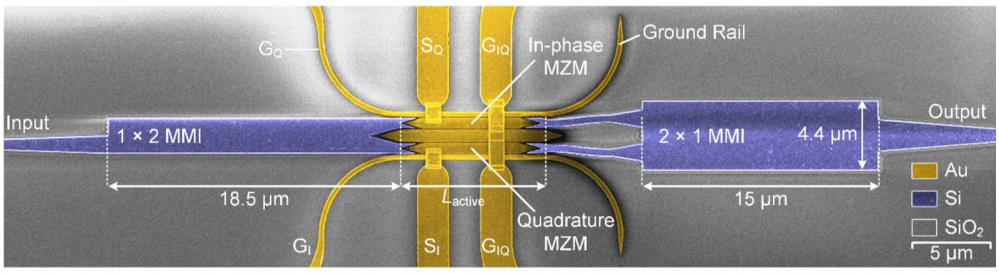

Figure 3.8: Colorized SEM image of the active section consisting of two all-plasmonic MZMs (quadrature MZM and in-phase MZM) integrated within a footprint of less than 15 μm $\times$ 4 μm. Light is guided as SPPs in slots formed by the electrodes. The electrodes (SI, SQ and GIQ) are contacted by suspended bridges. From [41, Fig. 2].

compactness. While the two designs proposed in 2014-2015 (the compact layout with closely spaced slots of [38] and the more relaxed layout derived from the phase modulator in [81]) where optically excited through photonic-plasmonic transitions, a new (third) design appears in 2017 [9] characterized by coupling with optical fibers and by a single metal layer technology.

In January 2016 a modified layout version of the plasmonic MZM was published, see [44] where a less compact push-pull modulator layout somewhat similar to the PM in [81] is proposed with MMI input and output splitters-combiners, see Fig. 3.9. Data modulation is demonstrated experimentally up to 72 Gbit/s (BPSK) and 108 Gbit/s (4-ASK) with driving voltages of $V_\pi = 4$ V and 2.5 V peak-to-peak for modulator lengths of 12.5 and 25 μm, respectively, with a static ER of 25 dB (25 μm long device) and a bandwidth in excess of 70 GHz. The push-pull configuration is obtained by properly poling the EO polymer deposed in the plasmonic waveguide slots. The reduced slot width on 80 nm coupled to the longer modulator length enables to reduce the modulator driving voltage. In [44] a discussion based on simplified analytical models is also reported on the effect of MZM asymmetry and uncertainty of the slot widths on the modulator ER. Since the plasmonic mode attenuation changes both with the slot width and with the applied voltage, with a theoretical linear dependence on the applied voltage (since the EO material is linear), a power unbalance results in the output optical combiner due to both the geometrical arm inbalance and (also for equal arms, i.e. slot widths) from the EO induced attenuation unbalance between the two arms. In [44] only the first effect is actually investigated, i.e. the ER is infinity with equal arms. A summary of the discussion can be provided with reference to Fig. 3.10. Plasmonic (simulated) propagation losses with Au as a metal increase with decreasing slot width, but at the same time the $V_\pi L$ product decreases, allowing for a shorter modulator given the on-off voltage and therefore compensating for the loss increase (Fig. 3.10 (a)); assuming $V_\pi = 3$ V, the device length indeed decreases with decreasing slot width and so does the insertion loss (Fig. 3.10 (b)). Concerning the extinction ratio, a slot width unbalance leads, for a $V_\pi = 3$ V device, to a deterioration of the ER that is more critical for low slot widths, as it would be expected (Fig. 3.10 (c)); this gives an upper bound to the uncertainty in the slot width that may be tolerated in the device design if the ER must be larger than some expected value, e.g. 20 dB. Notice that for equal slots the simulated ER is infinity, i.e. the model does not account for the ER inbalance related to the variation of the absorption due to the applied electric field. Finally, the transfer curve of a modulator with nominal slot width of 80 nm is shown, assuming $\pm$10 nm variation of the second slot with respect to the first (Fig. 3.10 (d)); this shows that such an uncertainty is tolerable if the ER must be kept above 20 dB. Other effects arising in practice that are not included in the model are, however: the possible load unbalance in the input splitter due to the different input impedance of two plasmonic slots having different width; the splitter or combiner unbalance arising from non-ideal alignment of the

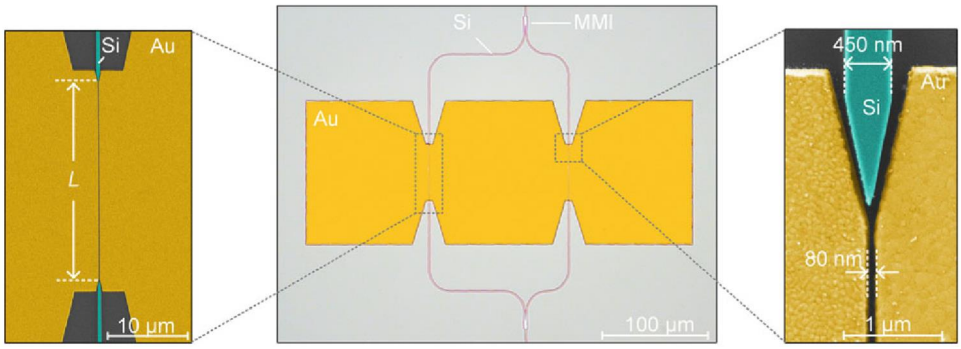

Figure 3.9: (a) Colorized microscope pictures of silicon-plasmonic organic hybrid MZM in [44]. The feeding waveguides and multimode interference couplers (MMIs) are realized in silicon, plasmonic phase modulators (PPMs) are used to modulate the phases in both arms. The arms of the MZI have an imbalance of 100 μm to allow for device characterization by swept laser source measurements. (b) Close-up of a PPM. The plasmonic MIM waveguide of length L is defined by gold sidewalls. The coupling from the silicon single mode waveguides to the plasmonic MIM waveguide is done using on a photonic-plasmonic converter (PPC). (c) Close-up of a PPC. The photonic mode is coupled into an SPP in the MIM waveguide of 80 nm width by means of a short taper. From [44, Fig. 1].

input and output exciting taper tips. Such effect can be investigated through 3D simulations, although mesh artifacts may actually masking the real behavior. In a following paper published in February 2017 a modulator structure similar to the one discussed in [44] (75 nm slot width and 20 μm interaction region length) was demonstrated to have a bandwidth in excess of 170 GHz through the generation of a 100 Gbps NRZ signal, see [49].

The invited Nature paper of 2016 [40] summarizes the results obtained in plasmonic modulators by the research group involved, adding a comparison between different modulator technologies, see Fig. 3.11.

Plasmonic modulators are able to bring down the modulator size from the cm scale (LN-like polymer-based modulators) or the mm scale (SOH modulators) to the μm scale, with a large bandwidth improvement, lower on-off voltages, albeit with larger optical insertion losses. An advantage of plasmonic modulators pointed out in [40] is the excellent overlap integral between the optical and the RF mode, caused by the slot concentration of the optical mode.

Besides summarizing modulator results presented in previous papers (devices A from [38] and C-D-E from [41], see [40, Table 1]) the paper presents a modulator design with ultra-narrow slots (40 and 45 nm, 6 μm length, called device B in [40,

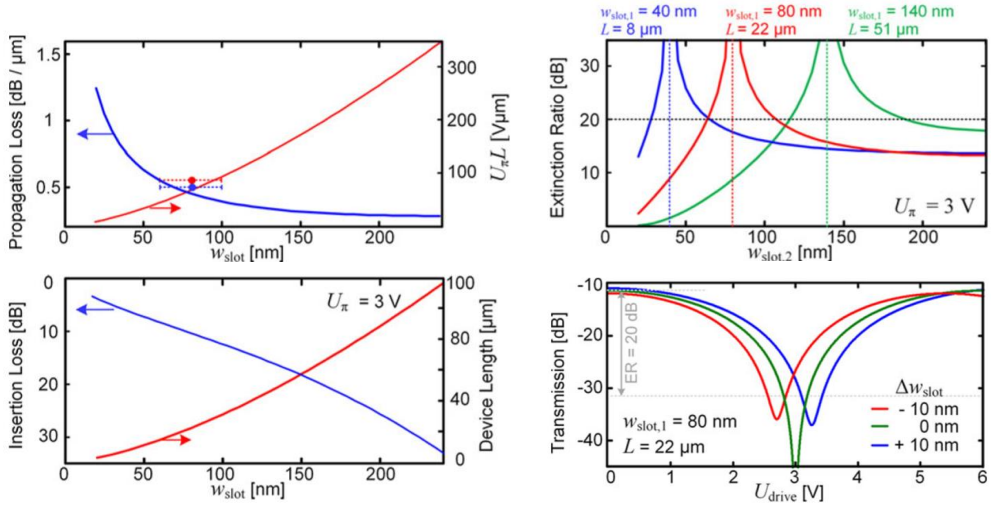

Figure 3.10: Effect of the slot width and of the arm unbalance on the insertion loss and extinction ratio of a MZM (see text). From [44, Fig. 3, 4, 5, 7].

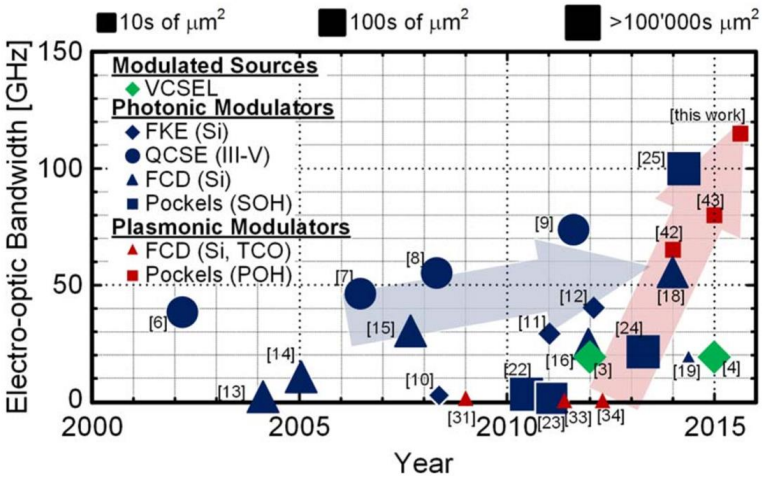

Figure 3.11: Bandwidth and footprint of electro–optical integrated modulators (experimental results only). The plot shows the improvement of the bandwidth over the last 15 years for integrated photonic and plasmonic modulator as well as directly modulated vertical-cavity lasers (VCSELs). The size of the symbol indicates the device footprint and the shape of the symbol indicates the effect it is based on. It can be seen that photonic modulators have experienced a steady but moderate increase in bandwidth over the years (blue arrow). The plot also shows how newer plasmonic modulators are about to outperform the photonic counterparts at a much smaller footprint (red arrow). The expected bandwidths are in excess of 100 GHz. The acronyms mean: FKE = Franz-Keldysh; QCSE = Quantum confined Stark; FCD = Free Carrier Dispersion; TCO = Transparent Conducting Oxides (ITO); POH = Plasmonic-organic hybrid. References are listed in the footnote close to the figure citation. From [40, Fig. 1].

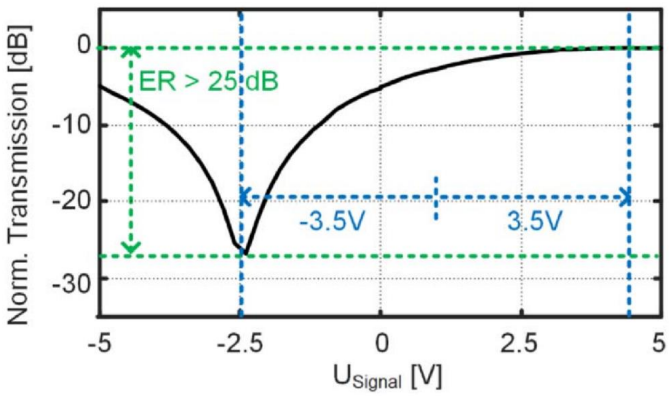

Figure 3.12: Measured response of the B device in [40, Table 1]. From [40, Fig. 9].

Table 1]; the Au thickness is 150 nm). For this device the record $V_\pi L$ product of 40 V·μm was achieved, with an on-off voltage of 7 V and an extinction ratio in excess of 25 dB. The modulator static response is shown in Fig. 3.12.

The paper presents a discussion on the effect of the Au thickness on the modulator performances (that is, indeed, minor) and, again, on the effect of asymmetries, also taking into account a possible splitting unbalance. A discussion is also provided on the optimization of the transition between the photonic and plasmonic waveguides, that enables to reduce the optical insertion losses also for a large thickness of the EO material deposed on the modulator; in particular, two different splitter geometries are compared, this first one being the one used in [38], the second the one in [41]. The performances of the two coupling schemes are compared in Fig. 3.13; the new scheme allows coupling to be almost independent of the thickness of the EO polymer.

The January 2017 paper [45], resulting from a cooperation between ETH and a chemistry group from the University of Washington, Seattle, is devoted to an overview of organic EO materials exploited in modulator design. The paper also includes a discussion on the geometry of the plasmonic modulator slots, showing that the slot walls are not necessarily vertical - this may affect the poling direction but is not expected to lead to catastrophic conferences, since the RF modulating field also follows, in a quasi-static condition, the same pattern as the poling DC field, see Fig. 3.14.

In November 2017 a new (third) plasmonic modulator design was presented in [9], see also the supplementary material in [10]. The distinctive feature of this modulator is the direct coupling (input and output) though an optical multicore fiber through diffraction gratings followed by polarization rotators; moreover, the design is based on a single metal layer deposited on glass. The polarization rotators are

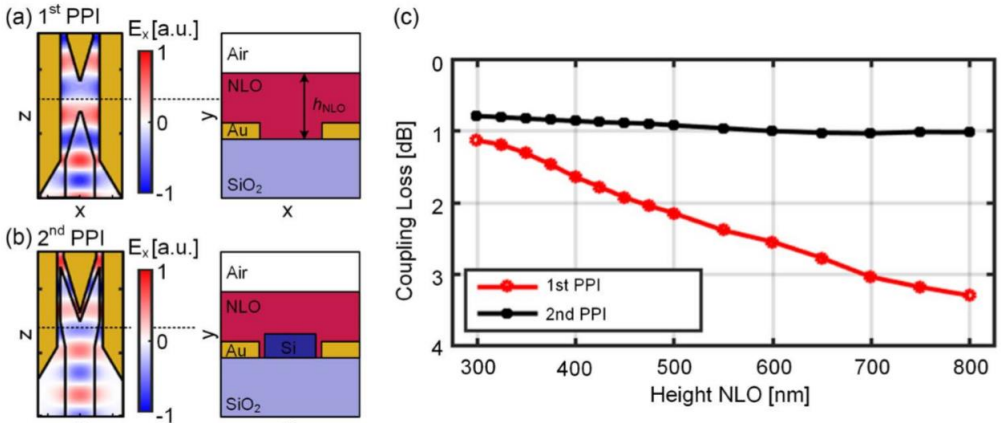

Figure 3.13: Coupling scheme for conversion of light from a silicon waveguide to a slot plasmonic waveguide. (a) Geometry of the coupler used in [38]. (b) Geometry of the improved coupling scheme in [41]. The blue/red fields show simulated field distributions. (c) Coupling losses as a function of the cladding height. The coupling efficiency of the design in (a) strongly varies with the cladding height, while the scheme (b) is almost independent of the cladding height, with coupling losses below 1 dB. From [40, Fig. 11].

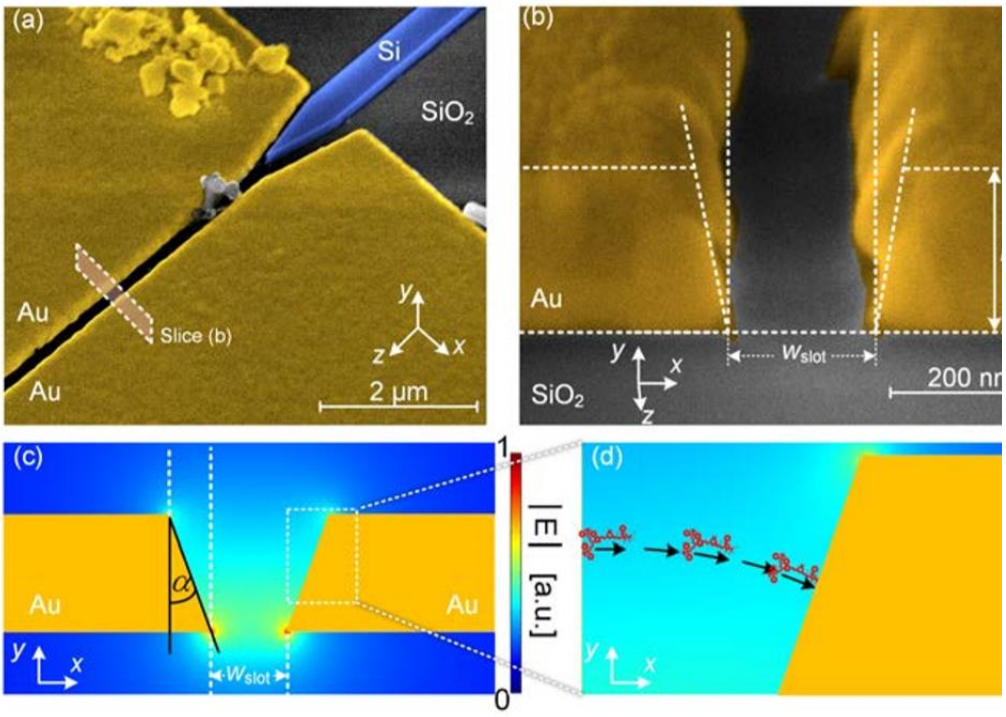

Figure 3.14: (a) Colorized SEM image of a plasmonic slot waveguide and feeding silicon waveguide. (b) Cross section of a plasmonic slot waveguide with a sidewall angle of approximately 10° to 15°. The image was taken with an angle of 52°. (c) Cross section of slot with $\alpha = 10°$ and simulated poling field (color-coded). (d) In case of tilted sidewalls, chromophores may not be ordered parallel to x-axis. From [45, Fig. 10].

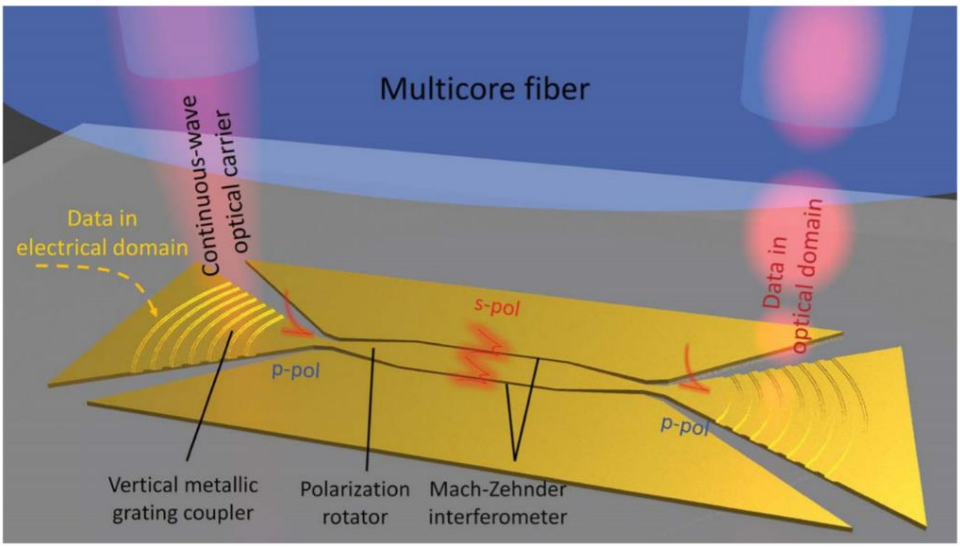

Figure 3.15: Artist impression of the operation principle of an all-metallic modulator in a Mach-Zehnder configuration with vertical metallic grating couplers and polarization rotators. A CW optical carrier is coupled into the device through the vertical metallic grating coupler from one core of the multicore fiber. The polarization of the optical carrier is rotated from p-polarization (p-pol) to s-polarization (s-pol) and split into the arms of the MZ in the polarization rotator section. The electrical information is then encoded by means of a phase shift through the Pockels effect onto the two optical signals in the MZI arms. At the output, the two optical signals from the arms interfere either constructively or destructively, and they are coupled back to another core of the multicore fiber. From [9, Fig. 1].

needed to convert vertically aligned electric fields (p-polarization) into a gap plasmonic modal field with a mostly horizontal $E-$ field distribution (s-polarization). The device has a very small footprint (36 $\times$6 μm) and demonstrated modulation beyond 116 Gbps with a BER less than 1.7×10^{-3}. The on-off voltage is 10 V with an ER around 10 dB; fiber-to-fiber loss was found to be 30 dB, much more than the simulated value of 17 dB; the discrepancy was attributed to technological issues. An artist impression of the modulator is given in Fig. 3.15 while Fig. 3.16 shows details of the structure and of the electrical driving module; the input signal is again fed to the modulator through a coplanar waveguide taper.

During the last two years, the cooperating ETH - University of Washington groups published an impressive amount of new results, partly based on the optimization of already developed designs.

A first line of development concerns the design optimization to lower the driving voltage level, so as to be able to drive the modulator directly with a high-speed

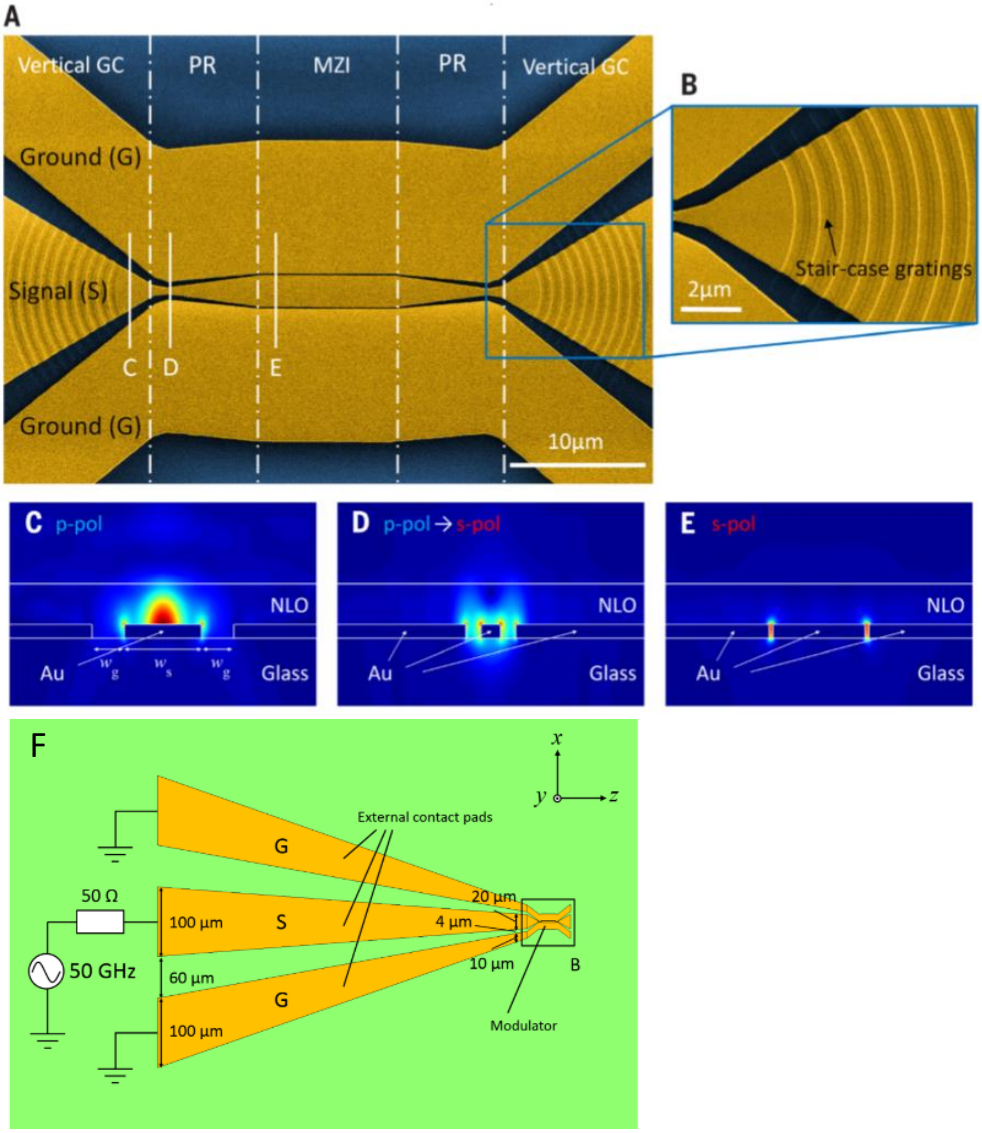

Figure 3.16: (a) Scanning electron micrograph of the device fabricated in a single 200-nm-thick layer of gold deposited on thermally grown glass layer. (b) Magnified image of a vertical metallic grating coupler with staircase gratings; the polarization rotation in the all-metallic device is illustrated by means of the plots of the electric field distributions. (c) A *p*-polarized surface plasmon polariton on the top surface of the device after coupling through the vertical metallic grating coupler. (d) Conversion from *p*-polarized into *s*-polarized plasmonic mode in the polarization rotator section. (e) *s*-polarized plasmonic mode coupled into the metallic slot waveguides. The positions of the cross sections are shown in (a). (f) RF feeding scheme. From [9, Fig. 2] and [10, pg. 6].

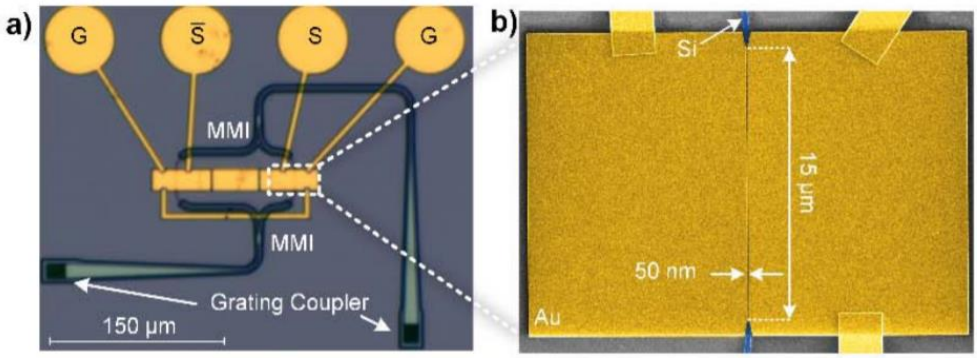

Figure 3.17: Plasmonic Mach-Zehnder modulator with driver-less operation: (a) Microscope picture of the whole structure including grating couplers, multimode-interference couplers (MMIs), ground (G), and signal (S) contact pads. (b) Colorized SEM picture of one of the two plasmonic phase modulators. From [12, Fig. 1].

digital circuit. In the OFC 2018 paper Baeuerle et al. [12] present a modulator design somewhat similar to the one in [44] but optimized with a 50 nm gap and a 15 μm length to achieve 100 Gbps NRZ operation with an on-off voltage less than 1 V peak-to-peak. This allows the modulator to be directly driven by a high-speed digital circuit, without the need to interpose a power-hungry driver amplifier. The layout of the modulator is shown in Fig. 3.17; notice that the Ground-Signal-Signal-Ground configuration enables a dual drive operation of the modulator (in this design the modulator is directly driven by RF probes). Also note that the splitter and the combiner introduce in the two modulator arms unequal phase delays. The modulator fiber-to-fiber insertion loss is estimated as 11-15 dB.

Further progress in reducing the peak-to-peak amplitude of the modulating signal was reported in 2019 with the conference and journal papers [13, 11]. The driving idea of those contributions is the integration and codesign between the modulator and a high-speed (above 100 Gbps) digital driver, leading to extremely compact circuits but also requiring a drastic decrease of the peak-to-peak modulating voltage - high-speed logical circuits based e.g. on SiGe HBT technologies typically have a speed-breakdown trade-off that leads to a decrease of the driving peak voltages for increasing speeds. The idea, already found in [12], was further developed in [13, 11] with the proposal of a (fourth) modulator layout, shown in Fig. 3.18. The modulator is a conventional Mach- Zehnder with two parallel phase modulators of length 15 μm; the photonic-plasmonic mode converters are conventional and the splitter and combiner are realized with a photonic waveguide. From the electrical standpoint, however, the configuration is not Ground-Signal-Ground

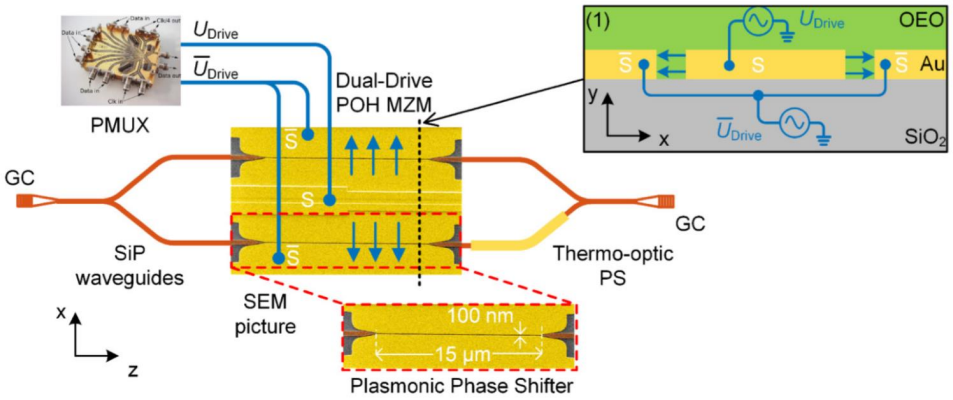

Figure 3.18: Dual-drive plasmonic transmitter. A power multiplexer (PMUX) generates the electrical differential signal (-Signal)-Signal-(-Signal) which is connected via electrodes with the plasmonic organic hybrid MZM. Colorized SEM pictures show the two plasmonic phase shifters incorporated in the MZM structure operated in push-pull mode. Light is coupled via grating couplers to the chip. An additional thermo-optic phase shifter (PS) allows for adaption of the MZM's operation point. Inset (1): Cross section of the plasmonic MZM. From [11].

as in common MZM, but rather (-Signal)-Signal-(-Signal) in a push-pull differential configuration. This allows, with a peak voltage V, to obtain a $2V$ voltage applied to the modulator slot (100 nm in this case). Considering the modulator as a lumped capacitor (the modulator size is small enough to exclude RF propagation effects) but also that the feeding RF connector lengths are of the order of 100 μm (somewhat optimistically considered as a distance along which RF delays are negligible also at 100 Gbps), the authors propose an open-circuit output loading of the modulator and remark that this yields another 2 factor gain with respect to the configuration where the generator and load are 50 Ω. In conclusion, the authors claim a factor 4 gain with respect to the conventional design. An additional feature is the thermo-optic phase shifter at the modulator output, that allows the zero bias point to be conveniently shifted e.g. to the half output power condition. In conclusion, the device proposed has, in the push-pull configuration, $V_\pi = 7.3$ V, on-chip losses around 10 dB and additional fiber-to-chip coupling losses of around 8.5 dB, with a modulation bandwidth in excess of 100 GHz. Transmission experiments at 120 Gbps where then performed in different configurations (back-to-back, 100 m, 500 m) demonstrating that a peak-to-peak drive voltage of 330 mV_{pp} is sufficient to operate the plasmonic transmitter in C band at 120 Gbps NRZ-OOK with a BER performance below the KP4-FEC limit. With a peak-to-peak drive voltage of 178 mV_{pp}, a BER performance is achieved of 2.3×10^{-3}, which is below the HD-FEC.

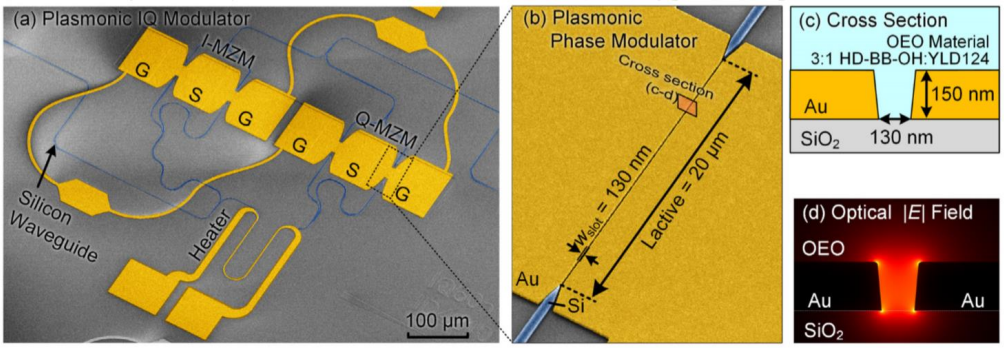

Figure 3.19: Plasmonic IQ Modulator in [46]. (a) Colorized microscope picture. The IQ modulator consists of two plasmonic Mach-Zehnder modulators (inphase (I) and quadrature (Q) MZM) integrated into a silicon photonic Mach-Zehnder interferometer. A thermo-optic phase shifter (heater) is used to adjust the IQ bias. (b) Zoom-in into the active section of the IQ modulator, a plasmonic phase modulator. (c) Schematic cross section of the plasmonic phase modulator. (d) Simulated optical field distribution in the plasmonic slot. From [46, Fig. 1].

A second line in evolutionary modulator design is the development of integrated IQ modulators based on single Mach-Zehnder designs, often with variations or improvements. In the OFC 2019 paper [47] (see also the extended Nature Communications paper [46]) an IQ version of the MZM described in [44] is proposed, for the layout and cross section see Fig. 3.19 that also includes data about the slot size and interaction length. With respect to [44], an additional oxide layer as well as a gold layer were introduced to implement the thermo-optic phase shifter. On-chip device losses were $\approx 13.7\,\mathrm{dB}$ at maximum transmission. The V_π of the MZM is approximately 6.5 V; fiber-to-chip coupling was performed using blazed grating couplers adapted for 10° incidence. The grating couplers contribute with additional $\approx 4\,\mathrm{dB}$ loss per coupler to the total fiber to fiber loss. Concerning performances, 100 GBd QPSK and 16QAM operation was demonstrated with electrical drive voltages of only 0.4 V and 1.5 V (measured at $50\,\Omega$), respectively. These low electrical drive voltages, in combination with a small device capacitance of 3.4 fF enable, the electrical energy consumptions per bit to be as low as 0.6 fJ/bit at 200 Gbps and 2 fJ/bit at 400 Gbps. The extended journal paper [46] also includes a discussion on operation stability of the IQ modulator; stable operation was demonstrated for more than 10 h as well as operation at 75°C, see [46, p. 3].

The already mentioned evolutionary path going from the phase modulator to the MZ to the MZ IQ modulator is confirmed by the design in [9], whose IQ version is presented in the March 2019 JLT paper [8]. Fig. 3.20 shows the overall design of the fiber-coupled modulator, together with the input RF pads connected

to isolated islands. The polarization converters needed to couple the out-of-fiber beam to the plasmonic mode have already been previously described. In fact, the design shown is deceptively simple, but includes a number of subtle features aiming at correctly positioning the zero-voltage transmittance and the phase shift needed between the I and Q sections. Fig. 3.21 shows some simulated results aiming at demonstrating the combination of slot width change Δw and geometrical offset Δy allowing to obtain a $\pi/2$ phase shift between the inputs of the two I and Q modulator sections. In Fig. 3.22 an additional π phase difference is shown to be introduced in each modulator, so that the modulators work for zero applied voltage in the null point; such a phase shift results from the slot width difference (90 and 100 nm) between the arms of each I and Q modulator. The modulator interaction length is 16 μm. The fiber-to-fiber losses across several devices have been measured to be between 28 and 37 dB; from simulation results, the expected total insertion losses for the IQ modulator is of the order of 23.9 dB, of which 5.0 dB are attributed to each of the focusing grating couplers, 2.1 dB to the polarization rotator sections, 6.7 dB to the phase modulators and the inherent 3 dB loss of the IQ modulator. To decrease losses, a number of technological and design expedients are proposed, such as increasing the EO polymer performances, and thus decreasing the modulator length (the polymer is now 75%HD-BB-OH/25%YLD124), eliminating the polarization rotators, improving the metal process. The present realization can be carried out on any substrate but in particular it was done on an oxide coated Si wafer. The IQ modulator achieved 100 Gbps QPSK modulation, resulting in a 200 Gbps data transmission with a BER of 3.64×10^{-3}. The peak amplitude of the driving voltage, mentioned in [8, Sec. IV], is $V_p = 2.5$ V.

A further development line has been the identification of application domains where the remarkable features of plasmonic modulators (in particular, their THZ bandwidth) could be a strong asset for their adoption. An application domain where the plasmonic solution seems to have no competitors are microwave photonic links for 5G systems located at frequencies above 300 GHz. In [18] plasmonic modulators are proposed for such applications, considering that competing technologies (e.g., thin film Lithium Niobate modulators) are anyway limited to 100 GHz. In [18] a detailed analysis of an analog link based on plasmonic modulators is carried out, showing that they may be an enabling technology for 100 GHz bandwidth analog links implemented in the range 200-300 GHz, with a Spurious Free Dynamic Range in excess of 90 dB/Hz$^{1/2}$.

Finally, some attempts were made to exploit materials different from electro-optic polymers in plasmonic modulators. [83] investigates the possibility to adopt ferroelectric materials, taking advantage of the fact that such materials, in particular barium titanate, have a large dielectric constant that enhances the electro-optic effect (this is in fact proportional to $n^3 r$, where n is the mode effective refractive index and r an element of the EO tensor. The proposed technology is based on thin-film $BaTiO_3$ (BTO) rather than lithium niobate, deposited on a layer of Al_2O_3

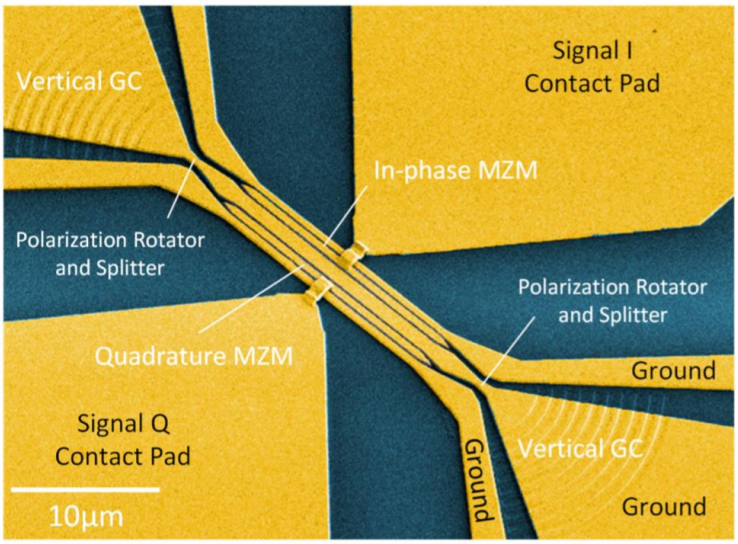

Figure 3.20: Perspective view of a colorized SEM image of the all-metallic IQ modulator in [8]. The modulator can be interconnected to a multicore fiber with a core pitch of 36 μm. The whole device is made of gold (colored in yellow) that is deposited on a smooth glass layer (colored in dark blue). From [8, Fig. 1].

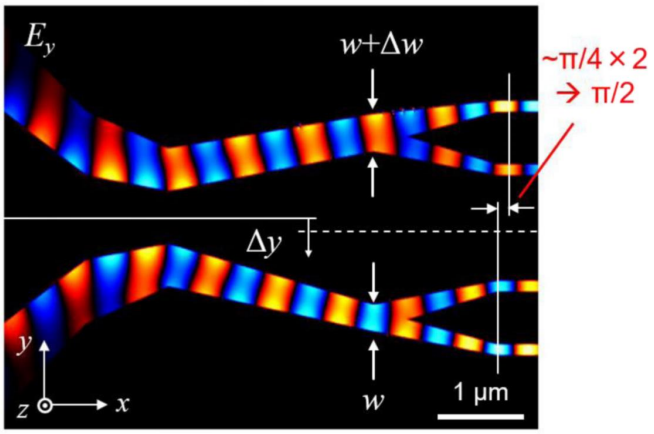

Figure 3.21: Design of the input splitter achieving quadrature between the input beams of the I and Q sections through a change of width and an asymmetrical alignement. The simulated electric field distribution is shown, demonstrating that the upper and lower beams are in phase quadrature. From [8, Fig. 3].

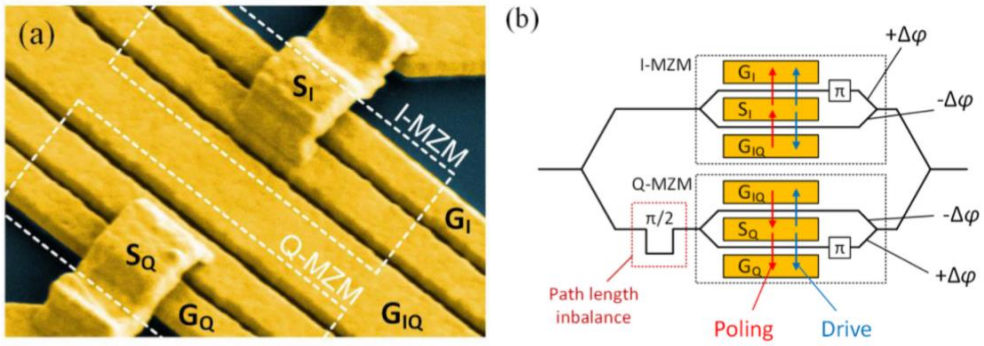

Figure 3.22: (a) Magnified SEM image of the four phase shifters. (b) Representation of the IQ modulator. Driving voltages are applied to the inner contacts, inducing positive and negative phase shifts to each MZM. Path length imbalances on the IQ modulator arms are added to induce a $\pi/2$phase difference between I and Q MZMs. By using different slot widths in the arms of the MZMs the π phase difference is generated to shift the IQ modulator transfer function into the null-point. >From [8, Fig. 4].

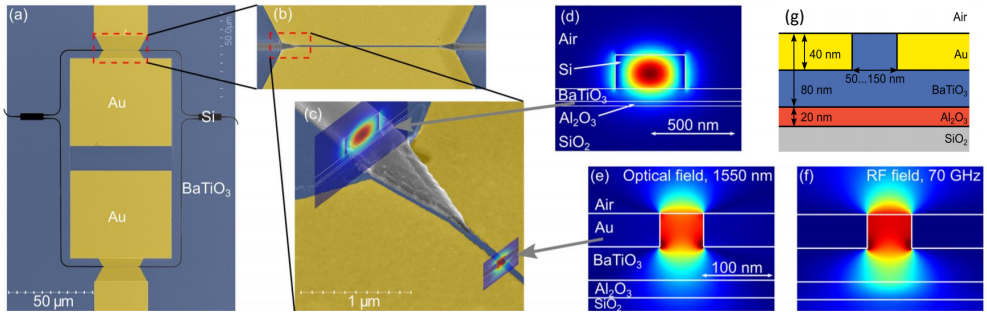

Figure 3.23: Colorized SEM images of (a) Plasmonic ferroelectric Mach-Zehnder modulator; (b) a plasmonic phase modulator. (c) Close-up of a tapered mode converter. The Si bus waveguide and tapered mode converter are used to couple the photonic mode into the Au-BTO-Au plasmonic slot waveguide. Insets: Simulated photonic and plasmonic mode profiles, respectively. (d) Simulated electrical field of the photonic mode in the Si waveguide (TE mode). (e) Simulated electrical field of the plasmonic mode (transverse component). (f) Simulated RF field in the slot waveguide (transverse component).We assume $\epsilon_{r,\mathrm{BTO}} = 1000$. (g) Cross section through the plasmonic ferroelectric phase shifter. 80 nm BTO is wafer-bonded to 3 μm SiO_2 on Si, using a 20-nm-thick Al_2O_3 buffer layer. Two gold electrodes enclose a narrow (50 . . . 150 nm) and 40-nm-tall BTO slab. From [83, Fig. 1, 2].

grown on silicon oxide. The geometry is somewhat similar to EO-polymer based modulators, apart from the reduced metal thickness (40 nm). The plasmonic slot width is 150 nm. The resulting device and device cross section, together with some simulation data, is shown in Fig. 3.23. The operation of the anisotropic BTO is quite complex, due to the presence of many non-null elements of the electrooptic tensor besides r_{33} as in Lithium Niobate; besides, as already noticed BTO has a very large refractive index that increases the EO effect. Experimental data show that the modulator exhibits, as expected, low-frequency dispersion effect connected with the piezoelectric nature of the material, with an effective $V_\pi L$ product between 200 and 250 V·μm. Experimental transmission data showed the feasibility of 58 Gbps PAM-4 data modulation with a line rate of 116 Gbps and 72 Gbps NRZ data modulation with a line rate of 72 Gbps. The experimental modulation bandwith was between 10 MHz and 70 GHz.

3.3 Numerical modelling of plasmonic modulators

To approach the numerical simulation of a plasmonic MZM, we used as reference one of the first compact structure proposed by Haffner et al. [38] whose physical realization is showed in Fig. 3.6.

As already discussed, the modulator is composed by two plasmonic MIM slot waveguides filled with DLD-164, an electro-optic polymer. The metallic elements defining the two branches are obtained by depositing gold on the SiO_2 substrate via a lift-off technique. Two photonic Si waveguides are employed to feed the optical carrier to the modulator where two photonic-plasmonic couplers convert the input mode before the access to the plasmonic section. A detailed scheme with geometry and employed materials is found in Fig. 3.5.

With the advance of the experimental reports, modelling of plasmonic-organic hybrid modulators grew in a similar manner. Analytical and/or semi-analytical models had been employed to quickly design and estimate the modulator's characteristics like extinction ration, insertion loss and frequency response [38, 40, 44].

Assuming an ideal MZM in push-pull operation with identical phase modulators in each arm, the output field E_{out} can be written in term of the input field E_{in} as

$$E_{\text{out}}(w_{\text{ slot}}, V_d) = e^{(j\beta(w_{\text{ slot}})-\alpha(w_{\text{ slot}})/2)L} \cos(\Delta\beta(w_{\text{ slot}}, V_d)L) E_{\text{in}} \tag{3.8}$$

where β is the propagation constant, α the power attenuation, $\Delta\beta$ is the change in propagation constant and L is the modulator's length. β and α depends strongly on the geometrical width of the slot waveguide while $\Delta\beta$ describing the index variation due to the linear electrooptic effect depends on both the slot width and the applied voltage. Despite their simplicity, such models are often completed by experimental measurements (i.e. power splitting coefficients at the photonic-plasmonic coupler) or theoretical quantities like the effective refractive indexes of the fundamental plasmonic mode in the slots determined from an electromagnetic solver. With the aid of commercial tools, Haffner et al. [38] use two-dimensional FEM simulations to determine the operating point and the optimal geometry of the MZM modulator. Then, they determine the coupling efficiency of the coupler using three-dimensional FDTD simulation [40].

In a joint paper from ETH Zürich and the University of Washington [45] the authors address in a systematic way the influence of the electrooptic polymer chemical nature on the macroscopic nonlinearities and how it is reflected on the MZM's performance and characterization. Moving from the experimental evidence of a slot-dependent electrooptic coefficient r_{33}, the authors determine from molecular dynamics simulations a realistic distribution of the organic chromofore. From it we can evaluate several behaviours

- slot filling effects where in very narrow slots (i.e. 50 nm) the nonlinear material may not fill homogeneously the waveguide. This in turn lowers the number of molecules available, reducing the value of the electrooptic coefficient r_{33} with respect to the bulk value.
- the noncovalent interactions of the electrooptic polymer with the Au and SiO_2 surfaces could restrain the motion of the molecules contrasting the action of the poling field.
- the presence of roughness and non-vertical walls from the microfabrication process leads to an inhomogeneous poling field hindering the alignment of the molecules and the macroscopic electrooptic effect.

In this work we concentrate on the simulation of the plasmonic slot waveguides to determine the modal profile of the optical carrier via a commercial electromagnetic simulator [100, 97]. We then study the complete propagation problem in the plasmonic MZM using a finite-difference time domain (FDTD) technique.

3.3.1 Investigation of the plasmonic slot waveguides through modal solver

Basic ingredient in the reference plasmonic MZ modulator pictured in Fig. 3.5, are the two slot waveguides composing the modulator's branches. Since the arms share the same geometry, it is sufficient to study the phase shifter structure obtained from a single slot. As a first step toward the modelling of a single slot waveguide, we aim to reproduce the analytical dispersion relation of surface plasmon polaritons (SPPs) on a metal-dielectric interface using a commercial tool.

To derive the analytical dispersion relation, we consider a one-dimensional structure made out of a single interface consisting of a dielectric with positive dielectric permittivity ϵ_d and a conducting material with dielectric function ϵ_m. We assume that the propagation takes place along z while x is the axis perpendicular to the dielectric-metal interface and y is the axis parallel to the interface.

For the TM modes we have, in each region (metal or dielectric):

$$\begin{aligned} \frac{\partial^2 H_y}{\partial x^2} + \left[k_0^2\epsilon - \beta^2\right] H_y &= 0 \\ E_z &= \mathrm{j}\frac{1}{\omega\epsilon_0\epsilon}\frac{\partial H_y}{\partial x} \\ E_x &= -\frac{\beta}{\omega\epsilon_0\epsilon}H_y. \end{aligned} \tag{3.9}$$

What we look for are solutions of the equation set (3.9) which have a propagating behaviour while being exponentially attenuated away from the interface. This

results in the following trial solution for the spatial field profile of the SPPs:

$$H_y(x,z) = \begin{cases} A_d \exp(-\mathrm{j}\beta z)\exp(-k_m x), & x > 0 \\ A_m \exp(-\mathrm{j}\beta z)\exp(k_d x), & x < 0 \end{cases} \tag{3.10}$$

where k_d and k_m are constants to be determined describing the attenuation of the surface wave in the direction perpendicular to the interface. Imposing the continuity of the transverse H_y field at $x = 0$ we obtain:

$$A_m = A_d$$

but also E_z should be continuous in $x = 0$, yielding:

$$\frac{k_m}{k_d} = -\frac{\epsilon_m}{\epsilon_d}.$$

Since k_m and k_d should be positive (or at least have a positive real part), this relation can be satisfied only if the metal has a permittivity with *negative* real part (we assume the dielectric to be almost lossless and have a positive permittivity). We notice that the solution found also satisfies the continuity of the $D_x = \epsilon E_x$ component, since:

$$\epsilon_m E_x\left(0^+, z\right) = -A_m \frac{\beta}{\omega\epsilon_0}\exp(-\mathrm{j}\beta z) = -A_d \frac{\beta}{\omega\epsilon_0}\exp(-\mathrm{j}\beta z) = \epsilon_d E_x\left(0^-, z\right).$$

From the wave equation in H_y we obtain, substituting:

$$\begin{aligned} k_m^2 + \left[k_0^2\epsilon_m - \beta^2\right] &= 0, \quad x < 0 \\ k_d^2 + \left[k_0^2\epsilon_d - \beta^2\right] &= 0, \quad x > 0 \end{aligned}$$

which leads to the SPP dispersion relation:

$$\beta = k_0\sqrt{\frac{\epsilon_m\epsilon_d}{\epsilon_d + \epsilon_m}}. \tag{3.11}$$

A set of equations similar to (3.9) can be written for TE modes, but from the continuity of the fields H_x, H_y we find zero field amplitudes A_m, A_d, thus showing that SPPs exist only as TM waves.

Eq. (3.11) admits a straightforward interpretation if the metal considered has negligible dissipation. Suppose that the dielectric permittivity ϵ_d be constant with respect to frequency; we have the following propagation regimes according to the value of the metal permittivity, that changes with the operating wavelength:

$$\begin{aligned} &\text{if } \epsilon_m > 0 \rightarrow \text{real } \beta \text{ but no plasmonic mode} \\ &\text{if } \epsilon_m < 0, \quad \epsilon_m + \epsilon_d < 0 \rightarrow \text{real } \beta, \text{ plasmonic mode} \\ &\text{if } \epsilon_m < 0, \quad \epsilon_m + \epsilon_d > 0 \rightarrow \text{imaginary } \beta, \text{ mode under cutoff.} \end{aligned}$$

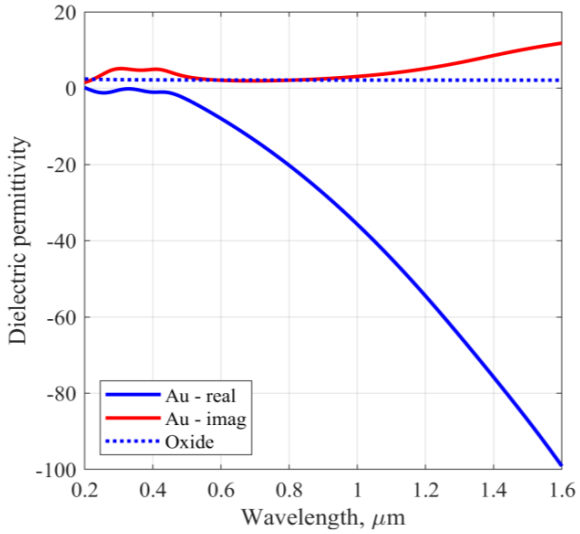

Figure 3.24: Dielectric permittivity for gold and SiO_2 as a function of input wavelength. Data are taken from [74, 58].

In a real metal with negligible losses, the typical propagation characteristic are: for angular frequencies $0 \leq \omega \leq \omega_{sp}$ the plasmonic mode propagates; above ω_{sp} we find a stopband where the mode is attenuated only; at very high frequency the metal permittivity has positive real part and the propagation constant is again real, but the mode is not any more confined to the interface and it radiates in the metal. Consider for instance gold according to the model data in [58] (the SiO_2 data are from [74]); the behavior of the real and imaginary part of the Au permittivity is shown in Fig. 3.24. At the angular frequency ω_{sp} the Au negative real permittivity becomes smaller, in absolute value, than the silica permittivity; this denotes the maximum propagation frequency for the plasmonic mode. At very high frequency (for Au between 1400 and 1500 THz) the metal becomes transparent with positive real part of the permittivity and radiated modes appear.

We are now ready to solve the same problem numerically using a FEM-based modal solver [96]. The test structure is composed by two finite half-spaces in which the metallic medium is gold, mathematically described with a Drude-Lorentz model, while the dielectric one composed by silicon dioxide is assumed to be constant with respect to frequency. By scanning over the input wavelength, we reconstruct the dispersion relation and the comparison with the analytical reference is carried using the effective refractive index. All the results are shown in Fig. 3.25 where the plasmonic dispersion relation is recovered both in terms of propagation and losses.

Now we move to the study of a slot waveguide using a FEM-based modal solver to look for the fundamental plasmonic mode and its depedence from the geometrical

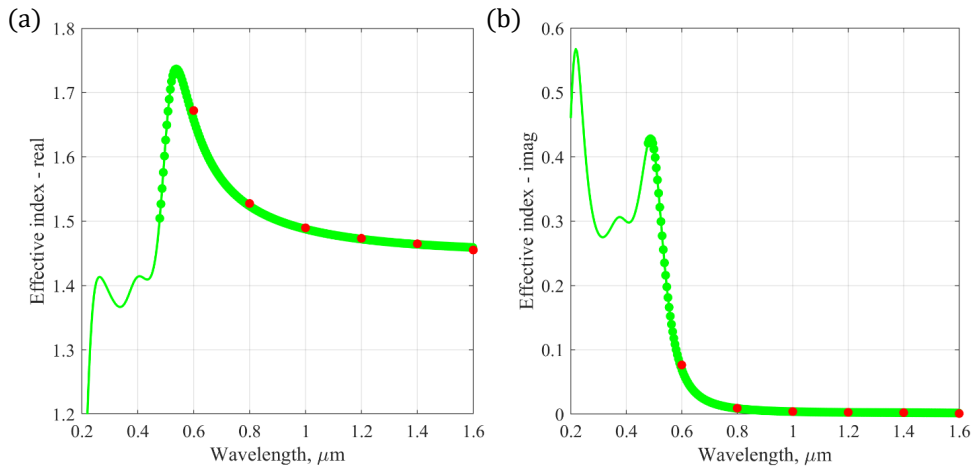

Figure 3.25: Comparison between the real (a) and the imaginary part (b) of the analytical dispersion relation of a SPP with the simulations results for a Au/SiO_2 interface. Dotted line represents SPPs with a real propagation constant.

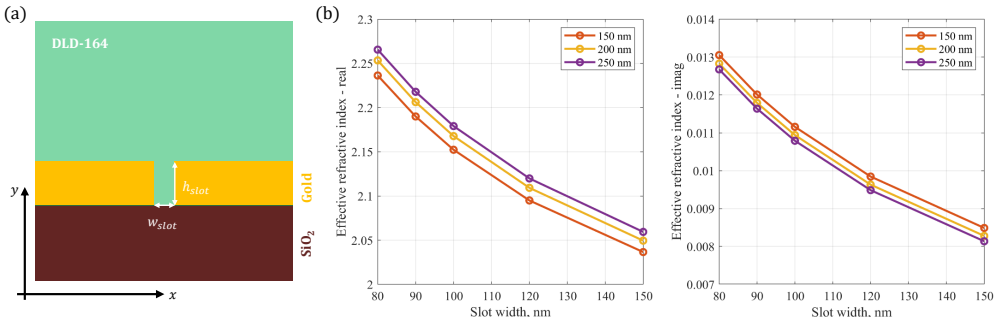

Figure 3.26: (a) Representation of the simulated plasmonic MIM slot waveguide; (b) variation of the effective refractive index of the fundamental plasmonic mode with respect to the slot width w_{slot} for few values of h_{slot}.

dimension h_{slot}, w_{slot}. Looking at the results shown in Fig. 3.26 obtained from the FEM solver, we can appreciate how the effect of different heights of the metallization is less relevant compared to the variation of the slot's width. In this way, it is possible to fix h_{slot} via energy consideration (i.e. targeting fJ/bit operation) or technological considerations (i.e. limits in the aspect ratio of the Au slot).

3.3.2 Design of a plasmonic Mach-Zehnder modulator

One of the objectives in the modelling of the Mach-Zehnder intereferometer is the computation of the transmission characteristic vs. the applied voltage. However, a three-dimensional electromagnetic simulation of the modulator may be time-consuming especially in a design phase. A different approach involves the study of 2D cross-sections to speed-up the exploration of the parameter space. We split the structure in a vertical cross-section to study the operating point via a modal solver and an horizontal cut of the 3D structure to study the propagation problem.

To determine the operating point of the MZM from the horizontal cross-section, we follow the same procedure adopted for the plasmonic slot waveguides. Considering the two slot waveguides as separate, we can determine the on-state operating point by looking at the bias point where the phase difference $\Delta\phi$ between the branches is null

$$\Delta\phi = \beta_1(V_d)l_1 - \beta_2(V_d)l_2 = 0 \tag{3.12}$$

$$\beta_1(V_d)L - \beta_2(V_d)L = 0 \rightarrow \beta_1(V_d) = \beta_2(V_d) \tag{3.13}$$

In Fig. 3.27 and 3.28 we report the simulation results of a symmetrical and an asymmetrical MZM cross-section from the FEM-based mode solver. The solid line indicates the result for the whole structure while the dotted ones show the effective

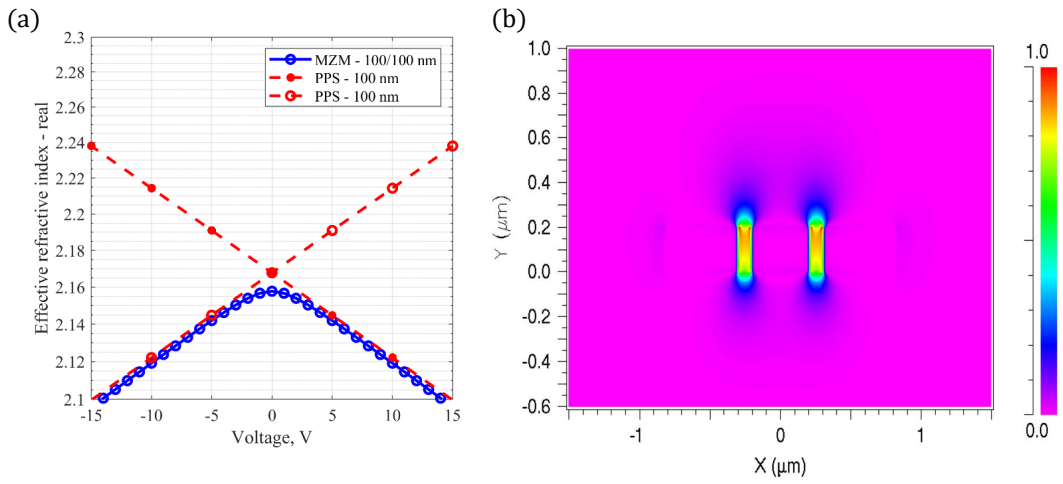

Figure 3.27: (a) Effective refractive index (real part) of the fundamental plasmonic mode as a function of the applied voltage for a symmetrical MZM structure with 100 nm 100 nm wide slots (blue) and the plasmonic phase shifters composing it (red); (b) Simulated profile of the electric field E_x-component of the on-state with $n_{ON} = 2.158 + j0.011$.

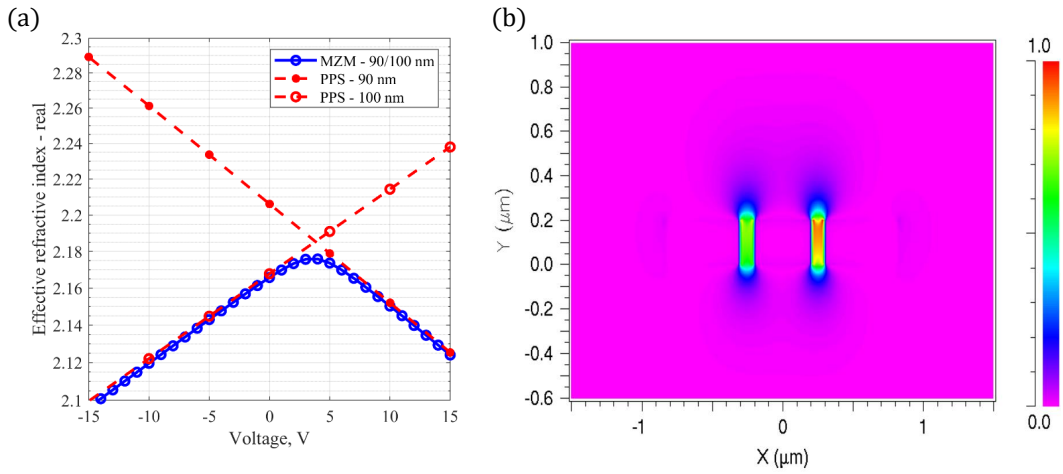

Figure 3.28: (a) Effective refractive index (real part) of the fundamental plasmonic mode as a function of the applied voltage for an asymmetrical MZM structure with 90 and 100 nm wide slots (blue) and the plasmonic phase shifters composing it (red); (b) Simulated profile of the electric field x-component of the on-state on-state with $n_{ON} = 2.176 + j0.011$.

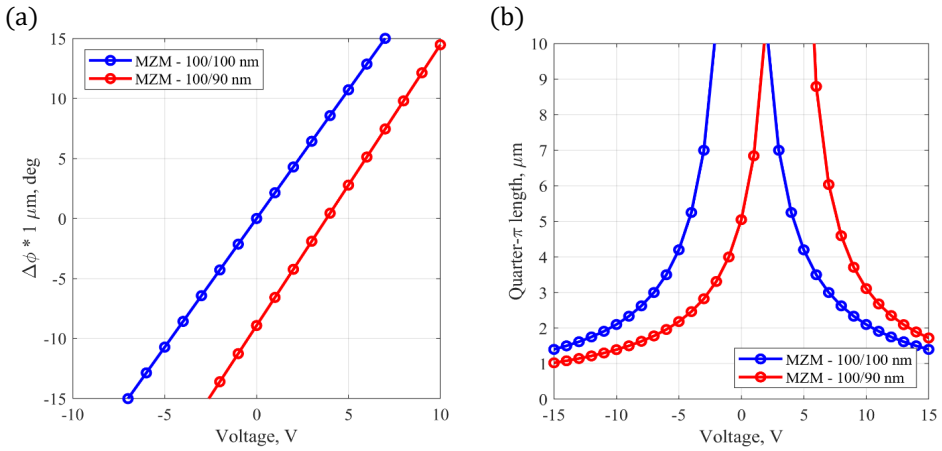

Figure 3.29: (a) Phase difference after 1 μm propagation length as a function of the applied bias for a symmetrical and asymmetrical MZM; (b) Calculated length of the plasmonic MZM to ensure quadrature operation against the applied voltage for a symmetrical and asymmetrical modulator.

index for the two slot waveguides composing the Mach-Zehnder structure. At their intersections, we find the on-state voltage which for asymmetrical structures is found for non-zero bias. From the knowledge of the propagation constants of the two branches, we can compute the length of the modulator's arms by inverting the phase relation with respect to the desired output phase. Since we are interested to operate at the quadrature point, we look for all the lengths which guarantee $\pi/4$ phase shift.

$$(\beta_1 - \beta_2)L = \frac{\pi}{4} \tag{3.14}$$

Looking at the results shown in Fig. 3.29, an asymmetrical structure gives us the possibility to implement quadrature operation with no applied bias using a plasmonic section 5 microns long.

Now we are ready to face the propagation problem, using a 2D horizontal section of the whole device. To simplify the evaluation of the linear electrooptic effect in the slots, we approximate the value of the electric field as the ratio of the applied signal voltage to the slot widths

$$\begin{aligned} \Delta n(V) &= \frac{1}{2} r_{33} n^3(0) E \\ &\approx \frac{1}{2} r_{33} n^3(0) \frac{\Delta V}{w_{\text{slot}}} \end{aligned} \tag{3.15}$$

Our objective is to obtain the static input-output characteristic of the modulator through the computation of the power reflection and transmission coefficients. A

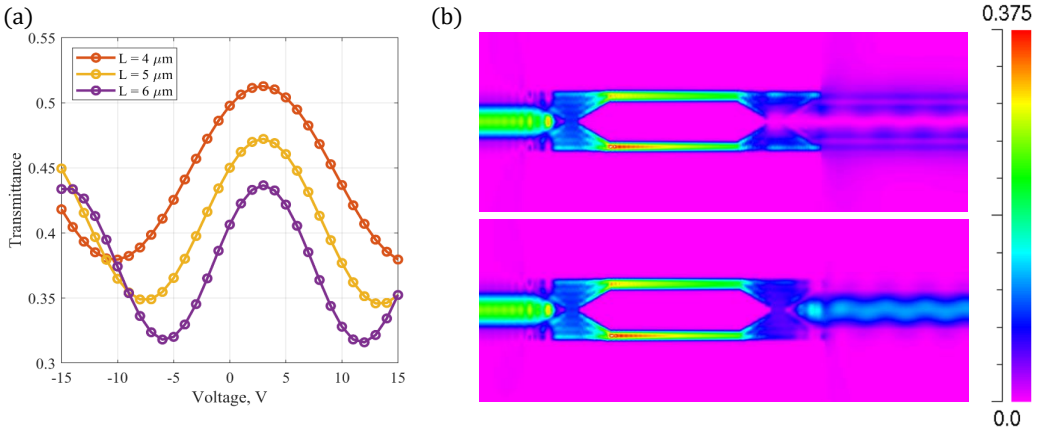

Figure 3.30: (a) Transmittance of an asymmetrical MZM with 100 and 90 nm wide slots against the applied bias for few values of the branches' length; (b) Colormap of the real part of the time-averaged Poynting vector in the off-state (top) and the on-state (bottom) from 2D EME simulations.

full-wave approach to the optical simulation as complete as finite-difference time domain (FDTD) would be the best course of action, but the heavy computational requirements on structure several microns long may hinder its use for large-scale parametric studies. A cheaper alternative is offered by the beam propagation method (BPM) in which the input field (in our case, from the photonic Si waveguide) is propagated in finite steps along the longitudinal direction to compute all the desired observables. Still, the presence of strong jumps in the refractive indexes in the plasmonic section give rise to numerical instabilities in the BPM computation nullifying part of its advantages. A compromise between the two technique is found with the eigenmode expansion (EME) [99, 102]. In EME the structure is sliced in uniform sections and Maxwell's equations are solved in a transmission line approach, where the transverse electric field is expressed through the local eigenvalues' basis and the propagation is kept into account through the usual phase exponentials. By matching the electric field's expansion at each section we are able to compute the unique expansion determining everywhere the solution of the problem.

Results of the simulations are reported in fig. 3.30. From the static characteristics, we can identify the on- and the off-state in for each configuration and the insertion losses, especially for longer arms. Focusing on the structure with the 5 microns long arms, we can look at the colormaps portraying the modulator at the on-, off- and the quadrature operating point. The device is showing proper operation, but in the off-state there is no sharp extinction of the optical power due to the presence of an additional mode in the waveguide to which the light is transferred.

On a technical ground EME proved to be as effective as FDTD simulations,

while reducing the simulation time (a quarter of hour compared to $\approx$ 2 hours of the FDTD simulations). However, we pay in the amount of RAM memory requested for the computation (about 50 GB vs. 6-10 GB from FDTD), making expensive the extension of EME simulation to 3D level.

3.4 Conclusions

In this chapter, we introduced the modulators as fundamental block for the manipulation of optical signals in a photonic integrated circuits. We provided a simple taxonomy of modulators based on the physical process governing the modulation process. Then we focused on plasmonic-organic hybrid modulators as a promising candidate for high-density and high-speed integrated modulator thanks to the localization property of plasmons and the Pockels effect exhibited by the active electro-optic polymer.

After a review on the experimental and modelling state of the art, we explored the design of plasmonic Mach-Zehnder interferometers through 2D simulations handling in an efficient way the modellling. On one hand, we logically decompose the problem in the transverse and propagation direction; on the other hand, we employ much lighter EME simulations to speed-up the exploration process while leveraging on FDTD simulations for the validation of the final design. Still, the presented simulation results neglect eventual imperfections in the structure, such as process variations of the slot waveguide or the inhomogeneous distribution of the electrooptic polymer. A study on the impact of these effects should be performed in order to attain a complete understanding of the device and its eventual weaknesses.

Appendix A

Modelling of the electron transport

A.1 Drift-diffusion equations

From the analysis of semiconductor devices under thermodynamic equilibrium and out-of-equilibrium, we can observe two main effects:

- passage of currents, linked to electric fields and gradients of carrier concentration
- presence of generation and recombination phenomena, due to an inhomogeneous distribution of the electron-hole populations

All those phenomena can be reunited in a self-consistent mathematical model of semiconductors known as the drift-diffusion equations. This model is composed by the Poisson equation, a continuity equation for the electrons and another one for the holes. To close the model, we need a constitutive relation for the current densities $J_{n,p}$ in terms of the electron and hole densities n, p and of the electric field.

A.1.1 Derivation of the transport model

Our entry point for the construction of the drift-diffusion is represented by Maxwell's equations:

$$\nabla \times \mathrm{H} = + \frac{\partial \mathrm{D}}{\partial t} + \mathrm{J} \tag{A.1}$$

$$\nabla \times \mathrm{E} = - \frac{\partial \mathrm{B}}{\partial t} \tag{A.2}$$

$$\nabla \cdot \mathrm{D} = \rho \tag{A.3}$$

$$\nabla \cdot \mathrm{B} = 0 \tag{A.4}$$

where E, D are the electric field and electric displacement; H, B are the magnetic field and magnetic induction; ρ is the charge density and J is the current density. To close this system of equations we need a set of constitutive relations for the electric and magnetic fields, expressed via the dielectric permittivity ϵ and the magnetic permeability μ.

If we introduce a vector potential A such that

$$\mathrm{B} = \nabla \times \mathrm{A}$$

we can immediately satisfy the requirement of the divergence of the magnetic induction, since the divergence of a curl is null for any vector field. Substitution in the Faraday's law (A.2) holds

$$\nabla \times \left(\mathrm{E} + \frac{\partial \mathrm{D}}{\partial t} \right) = 0 \implies \mathrm{E} + \frac{\partial \mathrm{A}}{\partial t} = -\nabla \phi$$

indicating the existance of a scalar field ϕ . Multiplication by ϵ on both sides and taking the divergence of the last equation, we get:

$$\rho + \epsilon \frac{\partial}{\partial t} \nabla \cdot \mathrm{A} = -\nabla \cdot (\epsilon \nabla \phi)$$

By fixing the divergence of A via the Lorentz gauge, we end up with the following expression

$$\rho - \frac{\epsilon}{c^2} \frac{\partial^2 \phi}{\partial t^2} = -\nabla \cdot (\epsilon \nabla \phi)$$

which reduces to the so-called Poisson equation when the propagation velocity of the signal across our device is well below the speed of light c

$$\rho = -\nabla \cdot (\epsilon \nabla \phi) \tag{A.5}$$

It is possible to obtain the same results if one suppose that the time derivative of the vector potential A is negligible: we refers to this approximation as quasi-static approximation. Now we apply the divergence operator to Ampère's law (A.1) and substituting the Gauss' law (A.3) into it, we obtain the continuity equation for the electrical charge:

$$\frac{\partial \rho}{\partial t} + \nabla \cdot \mathrm{J} = 0 \tag{A.6}$$

which can be rewritten in a more compact form introducing the displacement current.

$$\nabla \cdot \mathrm{J} + \frac{\partial \rho}{\partial t} = \nabla \cdot \mathrm{J}_{tot} = 0, \qquad \mathrm{J}_{tot} = \mathrm{J} + \mathrm{J}_D = \mathrm{J} + \frac{\partial \mathrm{D}}{\partial t}$$

At this point, it is possible to express the charge density as a sum of the free carriers and the fixed charges due to dopants.

$$\rho = q(p - n + N_D^+ - N_A^-) \tag{A.7}$$

We will express the total conduction current as the sum of the electron and hole components, splitting the charge continuity equation in one for each population:

$$-q\frac{\partial n}{\partial t} + \nabla \cdot \mathrm{J}_n = +qR \tag{A.8}$$

$$+q\frac{\partial p}{\partial t} + \nabla \cdot \mathrm{J}_p = -qR \tag{A.9}$$

where R is an arbitrary function with the meaning of net recombination rate.

At this point the mathematical model is made of three partial differential equations in the unknowns, but still no constitutive relation for the electron and hole current has been provided. To obtain it, we resort to the so-called moments of Boltzmann transport equation (BTE): as the “master" equation, each moment encompass a conservation equation for different quantities like the number of particles (0th moment), linear momentum density (1st moment) or the energy density (2nd moment). Under several assumptions, including but not limited to thermal equilibrium and parabolic bands for the carrier, we can rework the conservation equation for the linear momentum density to obtain

$$\mathrm{J}_n = qn\mu_n \mathrm{E} + qD_n \nabla n \tag{A.10}$$

$$\mathrm{J}_p = qp\mu_p \mathrm{E} - qD_p \nabla p \tag{A.11}$$

where $\mu_{n,p}$ is the carrier mobility and $D_{n,p}$ is the current diffusivity. In the above equations, the first term proportional to the electric field is the *drift* element while the second term involving the gradient of the carrier concentrations is the *diffusion* contribution.

A.1.2 Physical models

Carrier mobility

An accurate estimate of the carrier transit time is fundamental for evaluating the photodetector electrooptical bandwidth. In this view, carrier velocity saturation caused by the presence of strong electric fields must be accounted for; this has been included here through the electric field dependence of the carrier mobilities proposed by Canali [21]

$$\mu(E) = \frac{\mu_0}{\left[1 + \left(\dfrac{\mu_0 E}{v_{\mathrm{sat},0}}\right)^{\beta}\right]^{\frac{1}{\beta}}}. \tag{A.12}$$

Here μ_0 is the low-field mobility, $v_{\mathrm{sat},0}$ is the saturation velocity, β is a phenomenological parameter and the electric field magnitude E acts as carrier driving force.

Another relevant effect in the devices under investigation is the mobility dependence on the density of doping impurities. For this reason, the low-field mobility

μ_0 has been evaluated with the Masetti model [80]:

$$\mu_0 = \mu_{\min,1} \exp\left(-\frac{P_c}{N}\right) + \frac{\mu_{0,i} - \mu_{\min,2}}{1 + \left(\frac{N}{C_f}\right)^{\alpha}} - \frac{\mu_1}{1 + \left(\frac{C_s}{N}\right)^{\gamma}},$$

where $\mu_{0,i}$ is the low-field mobility of the intrinsic material, $N = N_A + N_D$ is the sum of acceptor and donor concentrations and $\mu_{\min,1}$, $\mu_{\min,2}$, μ_1, P_c, C_f, C_s, α, γ are fitting parameters.

Generation and recombination phenomena

As seen in the introduction, generation and recombination phenomena express the physical mechanisms behind the creation and annihilation of electron-hole pairs.

One of the main recombination phenomena in semiconductors is Shockley-Read-Hall (SRH) recombinations. It describes the generation and recombination of electron-hole pairs mediated by an energy state within the bandgap: such state is often due to defects or dopants within the lattice. In static conditions, the SRH rate is expressed as

$$R_{SRH} = \frac{np - n_i^2}{\tau_n(n + n_i) + \tau_p(p + n_i)} \tag{A.13}$$

where $\tau_{n,p}$ represent the inverse transition probabilities associated to the transitions. Such model is not suitable to study time dependent and/or dynamic effects where a formulation in terms of capture/escape rates for the traps is necessary.

Radiative recombination processes involve emission of a photon due to band-to-band transitions. For this reason emitted photons have an energy grater or equal than the semiconductor's bandgap. Expression of the rate is

$$R_{rad} = B(np - n_i^2) \tag{A.14}$$

where B is the bimolecular recombination coefficient with dimensions $\mathrm{cm^3 s^{-1}}$. In presence of excess carriers, radiative recombination increases indicating strong spontaneous emission of photons as in light emitting diodes (LEDs).

Auger recombinations describe the interaction between three carriers where the energy produced by the recombination of an electron-hole pair is transferred to the third particle. Formula used to evaluate the rate is given by

$$R_{Auger} = (C_n n + C_p p)(np - n_i^2) \tag{A.15}$$

where $C_{n,p}$ are the Auger coefficients with physical dimensions of $\mathrm{cm^6 s^{-1}}$.

A.2 Multiphysics coupling between optical and transport solver

Coupling between the electrical and the optical sub-problems is realized through the physical phenomenon of optical generation. From the knowledge of the electromagnetic fields obtained from the optical solver, we can construct our optical generation rate starting from the Poynting's theorem

$$\frac{\partial}{\partial t}\left[\frac{1}{2}\epsilon\mathbf{E}^2+\frac{1}{2}\mu\mathbf{H}^2\right]+\nabla\cdot\mathbf{S}+\mathbf{J}\cdot\mathbf{E}=0 \tag{A.16}$$

where $\mathbf{S}=\mathbf{E}\times\mathbf{H}$ is the Poynting vector expressing the power flow associated with the electromagnetic fields. Under the hypothesis of time-harmonic behaviour for the fields and absence of free charges, we study a time-averaged version of the electromagnetic energy equation

$$\langle u_{EM}\rangle+\nabla\cdot\langle\mathbf{S}\rangle=0 \tag{A.17}$$

in which the time-averaged density of electromagnetic energy $\langle u_{EM}\rangle$ and the time-averaged Poynting vector are

$$\langle u_{EM}\rangle=\frac{1}{2}\omega\mathrm{Im}\{\epsilon\}|\mathbf{E}|^2 \tag{A.18}$$

$$\langle\mathbf{S}\rangle=\frac{1}{2}\mathrm{Re}\{\mathbf{E}\times\mathbf{H}^*\} \tag{A.19}$$

At this point, we can compute the amount of power absorbed by the structure and we can relate it to the density of absorbed photons through the quantum of energy, resulting in the following expression for the optical generation rate

$$G_{opt}=\eta\frac{\langle u_{EM}\rangle}{\hbar\omega} \tag{A.20}$$

where $\omega=\frac{2\pi}{\lambda}$ and η is the quantum yield. It is usually assumed to have unit value implying we have at least one electron-hole pair per impinging photon. Finally, we plug this additional term in the continuity equations of the drift-diffusion model concluding the derivation.

Bibliography

[1] J. J. Ackert et al. “High-speed detection at two micrometres with monolithic silicon photodiodes”. In: *Nature Photon.* 9.6 (June 2015), pp. 393–396. ISSN: 1749-4893. URL: https://doi.org/10.1038/nphoton.2015.81.

[2] D. Ahn et al. “High performance, waveguide integrated Ge photodetectors”. In: *Opt. Express* 15.7 (Apr. 2007), pp. 3916–3921. DOI: 10.1364/OE.15.003916. URL: http://www.opticsexpress.org/abstract.cfm?URI=oe-15-7-3916.

[3] R. L. Anderson. “Germanium-Gallium Arsenide Heterojunctions [Letter to the Editor]”. In: *IBM J. Res. Develop.* 4.3 (July 1960), pp. 283–287. ISSN: 0018-8646. DOI: 10.1147/rd.43.0283.

[4] S. Assefa, Fengnian Xia, and Yurii A. Vlasov. “Reinventing germanium avalanche photodetector for nanophotonic on-chip optical interconnects”. In: *Nature* 464.7285 (Mar. 2010), pp. 80–84. ISSN: 1476-4687. URL: https://doi.org/10.1038/nature08813.

[5] S. Assefa et al. “CMOS-integrated high-speed MSM germanium waveguide photodetector”. In: *Opt. Express* 18.5 (Mar. 2010), pp. 4986–4999. DOI: 10.1364/OE.18.004986. URL: http://www.opticsexpress.org/abstract.cfm?URI=oe-18-5-4986.

[6] A. H. Atabaki et al. “Integrating photonics with silicon nanoelectronics for the next generation of systems on a chip”. In: *Nature* 556.7701 (2018), pp. 349–354. ISSN: 1476-4687. DOI: 10.1038/s41586-018-0028-z. URL: https://doi.org/10.1038/s41586-018-0028-z.

[7] M. Auf der Maur et al. “Trap-assisted tunneling in InGaN/GaN single-quantum-well light-emitting diodes”. In: *Appl. Phys. Lett.* 105.13 (Jan. 2014), p. 133504. ISSN: 0003-6951. DOI: 10.1063/1.4896970. URL: https://doi.org/10.1063/1.4896970.

[8] M. Ayata et al. “All-Plasmonic IQ Modulator With a 36 μm Fiber-to-Fiber Pitch”. In: *J. Lightwave Technol.* 37.5 (2019), pp. 1492–1497. ISSN: 0733-8724. URL: http://jlt.osa.org/abstract.cfm?URI=jlt-37-5-1492.

[9] M. Ayata et al. "High-speed plasmonic modulator in a single metal layer". In: *Science* 358.6363 (2017), pp. 630–632. ISSN: 0036-8075. DOI: 10.1126/science.aan5953. eprint: https://science.sciencemag.org/content/358/6363/630.full.pdf. URL: https://science.sciencemag.org/content/358/6363/630.

[10] M. Ayata et al. "High-speed plasmonic modulator in a single metal layer - supplemental material". In: *Science* 358.6363 (2017), pp. 630–632. ISSN: 0036-8075. DOI: 10.1126/science.aan5953. eprint: https://science.sciencemag.org/content/358/6363/630.full.pdf. URL: https://science.sciencemag.org/content/358/6363/630.

[11] B. Baeuerle et al. "120 GBd plasmonic Mach-Zehnder modulator with a novel differential electrode design operated at a peak-to-peak drive voltage of 178 mV". In: *Opt. Express* 27.12 (June 2019), pp. 16823–16832. URL: http://www.opticsexpress.org/abstract.cfm?URI=oe-27-12-16823.

[12] B. Baeuerle et al. "Driver-Less Sub 1 Vpp Operation of a Plasmonic-Organic Hybrid Modulator at 100 GBd NRZ". In: *2018 Optical Fiber Commmunication Conference*. OSA Technical Digest (online). San Diego, California: Optical Society of America, Mar. 2018, p. M2I.1. URL: http://www.osapublishing.org/abstract.cfm?URI=OFC-2018-M2I.1.

[13] B. Baeuerle et al. "Dual-Drive Plasmonic Transmitter with Co-Designed Driver Electronics operated at 120 GBd On-Off Keying". In: *2019 Optical Fiber Communications Conference and Exhibition (OFC)*. 2019, pp. 1–3. DOI: https://doi.org/10.1364/OFC.2019.M2F.3.

[14] J. Bai et al. "Study of the defect elimination mechanisms in aspect ratio trapping Ge growth". In: *Appl. Phys. Lett.* 90.10 (Dec. 2007), p. 101902. ISSN: 0003-6951. DOI: 10.1063/1.2711276. URL: https://doi.org/10.1063/1.2711276.

[15] F. Boeuf et al. "Silicon Photonics R D and Manufacturing on 300-mm Wafer Platform". In: *J. Lightwave Technol.* 34.2 (Jan. 2016), pp. 286–295. ISSN: 1558-2213. DOI: 10.1109/JLT.2015.2481602.

[16] N. Boynton et al. "A heterogeneously integrated silicon photonic/lithium niobate travelling wave electro-optic modulator". In: *Opt. Express* 28.2 (Jan. 2020), pp. 1868–1884. URL: http://www.opticsexpress.org/abstract.cfm?URI=oe-28-2-1868.

[17] F. Bufler. *Full-Band Monte Carlo Simulation of Electrons and Holes in Strained Si and SiGe*. Munich: Herbert Utz Verlag, 1998.

[18] M. Burla et al. "500 GHz plasmonic Mach-Zehnder modulator enabling sub-THz microwave photonics". In: *APL Photon.* 4.5 (Jan. 2020), p. 056106. DOI: 10.1063/1.5086868. URL: https://doi.org/10.1063/1.5086868.

[19] M. J. Byrd et al. “Mode-evolution based coupler for Ge-on-Si photodetectors”. In: *2016 IEEE Photonics Conference (IPC)*. 2016, pp. 252–253. DOI: 10.1109/IPCon.2016.7831065.

[20] M. J. Byrd et al. “Mode-evolution-based coupler for high saturation power Ge-on-Si photodetectors”. In: *Opt. Lett.* 42.4 (Feb. 2017), pp. 851–854. DOI: 10.1364/OL.42.000851. URL: http://ol.osa.org/abstract.cfm?URI=ol-42-4-851.

[21] C. Canali et al. “Electron and hole drift velocity measurements in silicon and their empirical relation to electric field and temperature”. In: *IEEE Trans. Electron Devices* 22.11 (Nov. 1975), pp. 1045–1047. ISSN: 1557-9646. DOI: 10.1109/T-ED.1975.18267.

[22] H. Chen et al. “-1 V bias 67 GHz bandwidth Si-contacted germanium waveguide p-i-n photodetector for optical links at 56 Gbps and beyond”. In: *Opt. Express* 24.5 (Mar. 2016), pp. 4622–4631. DOI: 10.1364/OE.24.004622.

[23] H. T. Chen et al. “25-Gb/s 1310-nm Optical Receiver Based on a Sub-5-V Waveguide-Coupled Germanium Avalanche Photodiode”. In: *IEEE Photon. J.* 7.4 (Aug. 2015), pp. 1–9. ISSN: 1943-0647. DOI: 10.1109/JPHOT.2015.2460116.

[24] H. T. Chen et al. “High sensitivity 10Gb/s Si photonic receiver based on a low-voltage waveguide-coupled Ge avalanche photodetector”. In: *Opt. Express* 23.2 (Jan. 2015), pp. 815–822. DOI: 10.1364/OE.23.000815. URL: http://www.opticsexpress.org/abstract.cfm?URI=oe-23-2-815.

[25] H. T. Chen et al. “High-Responsivity Low-Voltage 28-Gb/s Ge p-i-n Photodetector With Silicon Contacts”. In: *J. Lightwave Technol.* 33.4 (Feb. 2015), pp. 820–824. URL: http://jlt.osa.org/abstract.cfm?URI=jlt-33-4-820.

[26] H. T. Chen et al. “Low-voltage Ge avalanche photodetector for highly sensitive 10Gb/s Si photonics receivers”. In: *11th International Conference on Group IV Photonics (GFP)*. Aug. 2014, pp. 106–107. DOI: 10.1109/Group4.2014.6961949.

[27] H. T. Chen et al. “Sub-5V Germanium Waveguide Avalanche Photodiode based 25 Gb/s 1310 nm Optical Receiver”. In: *Asia Communications and Photonics Conference 2015*. Optical Society of America, 2015, AM1B.4. DOI: 10.1364/ACPC.2015.AM1B.4. URL: http://www.osapublishing.org/abstract.cfm?URI=ACPC-2015-AM1B.4.

[28] S. Chen et al. "Electrically pumped continuous-wave 1.3 μm InAs/GaAs quantum dot lasers monolithically grown on on-axis Si (001) substrates". In: *Opt. Express* 25.5 (Mar. 2017), pp. 4632–4639. DOI: 10.1364/OE.25.004632. URL: http://www.opticsexpress.org/abstract.cfm?URI=oe-25-5-4632.

[29] P. Ciccarella et al. "Impedance-Sensing CMOS Chip for Noninvasive Light Detection in Integrated Photonics". In: *IEEE Trans. Circuits Devices II: Express Briefs* 63.10 (Oct. 2016), pp. 929–933. ISSN: 1558-3791. DOI: 10.1109/TCSII.2016.2538338.

[30] *Cisco Global Cloud Index: Forecast and Methodology, 2016–2021*. Tech. rep. Cisco, Nov. 2018.

[31] P. Clauberg and P. von Allmen. "Vectorial beam-propagation method for integrated optics". In: *Electron. Lett.* 27.8 (1991), pp. 654–655.

[32] L. Colace and G. Assanto. "Germanium on Silicon for Near-Infrared Light Sensing". In: *IEEE Photon. J.* 1.2 (Aug. 2009), pp. 69–79. ISSN: 1943-0647. DOI: 10.1109/JPHOT.2009.2025516.

[33] L. Colace et al. "Efficient high-speed near-infrared Ge photodetectors integrated on Si substrates". In: *Appl. Phys. Lett.* 76.10 (Jan. 2000), pp. 1231–1233. ISSN: 0003-6951. DOI: 10.1063/1.125993. URL: https://doi.org/10.1063/1.125993.

[34] L. Colace et al. "Ge/Si (001) Photodetector for Near Infrared Light". In: *Solid State Phenom.* Vol. 54. Solid State Phenom. Aug. 1997, pp. 55–58. DOI: 10.4028/www.scientific.net/SSP.54.55.

[35] C. T. DeRose et al. "Ultra compact 45 GHz CMOS compatible Germanium waveguide photodiode with low dark current". In: *Opt. Express* 19.25 (Dec. 2011), pp. 24897–24904. DOI: 10.1364/OE.19.024897. URL: http://www.opticsexpress.org/abstract.cfm?URI=oe-19-25-24897.

[36] P. De Dobbelaere et al. "Packaging of Silicon Photonics Systems". In: *Optical Fiber Communication Conference*. Optical Society of America, 2014, W3I.2. DOI: 10.1364/OFC.2014.W3I.2. URL: http://www.osapublishing.org/abstract.cfm?URI=OFC-2014-W3I.2.

[37] T. Grasser et al. "A Review of Hydrodynamic and Energy-Transport Models for Semiconductor Device Simulation". In: *Proc. IEEE* 91.2 (2003), pp. 251–274. DOI: 10.1109/JPROC.2002.808150. URL: http://www.iue.tuwien.ac.at/pdf/ib_2003/JB2003_Grasser_1.pdf.

[38] C. Haffner et al. "All-plasmonic Mach-Zehnder modulator enabling optical high-speed communication at the microscale". In: *Nature Photon.* 9.8 (Aug. 2015), pp. 525–528. ISSN: 1749-4893. URL: https://doi.org/10.1038/nphoton.2015.127.

[39] C. Haffner et al. “All-plasmonic Mach-Zehnder modulator enabling optical high-speed communication at the microscale - supplemental material”. In: *Nature Photon.* 9.8 (Aug. 2015), pp. 525–528. ISSN: 1749-4893. URL: https://doi.org/10.1038/nphoton.2015.127.

[40] C. Haffner et al. “Plasmonic Organic Hybrid Modulators–Scaling Highest Speed Photonics to the Microscale”. In: *Proc. IEEE* 104.12 (2016), pp. 2362–2379. ISSN: 1558-2256. DOI: 10.1109/JPROC.2016.2547990.

[41] C. Haffner et al. “Ultra-compact plasmonic IQ-modulator”. In: *2015 European Conference on Optical Communication (ECOC)*. Sept. 2015, pp. 1–3. DOI: 10.1109/ECOC.2015.7341676.

[42] A. R. Hawkins et al. “High gain-bandwidth-product silicon heterointerface photodetector”. In: *Appl. Phys. Lett.* 70.3 (Jan. 1997), pp. 303–305. ISSN: 0003-6951. DOI: 10.1063/1.118399. URL: https://doi.org/10.1063/1.118399.

[43] A. R. Hawkins et al. “Silicon heterointerface photodetector”. In: *Appl. Phys. Lett.* 68.26 (Jan. 1996), pp. 3692–3694. ISSN: 0003-6951. DOI: 10.1063/1.115975.

[44] W. Heni et al. “108 Gbit/s Plasmonic Mach–Zehnder Modulator with > 70-GHz Electrical Bandwidth”. In: *J. Lightwave Technol.* 34.2 (Jan. 2016), pp. 393–400. URL: http://jlt.osa.org/abstract.cfm?URI=jlt-34-2-393.

[45] W. Heni et al. “Nonlinearities of organic electro-optic materials in nanoscale slots and implications for the optimum modulator design”. In: *Opt. Express* 25.3 (Feb. 2017), pp. 2627–2653. URL: http://www.opticsexpress.org/abstract.cfm?URI=oe-25-3-2627.

[46] W. Heni et al. “Plasmonic IQ modulators with attojoule per bit electrical energy consumption”. In: *Nature Comm.* 10.1 (Apr. 2019), p. 1694. ISSN: 2041-1723. URL: https://doi.org/10.1038/s41467-019-09724-7.

[47] W. Heni et al. “Sub-fJ/Bit Operation of 100 GBd Plasmonic IQ Modulators”. In: *2019 Optical Fiber Communications Conference and Exhibition (OFC)*. 2019, pp. 1–3. DOI: 10.1364/OFC.2019.Tu2H.4.

[48] H. J. W. M. Hoekstra. “On beam propagation methods for modelling in integrated optics”. In: *Opt. Quantum Electron.* 29.2 (1997), pp. 157–171. ISSN: 1572-817X. DOI: 10.1023/A:1018549904885. URL: https://doi.org/10.1023/A:1018549904885.

[49] C. Hoessbacher et al. “Plasmonic modulator with >170 GHz bandwidth demonstrated at 100 GBd NRZ”. In: *Opt. Express* 25.3 (Feb. 2017), pp. 1762–1768. URL: http://www.opticsexpress.org/abstract.cfm?URI=oe-25-3-1762.

[50] W. Hofmann et al. “40 Gbit/s modulation of 1550 nm VCSEL”. In: *Electron. Lett.* 47.4 (2011), pp. 270–271. URL: https://digital-library.theiet.org/content/journals/10.1049/el.2010.3631.

[51] D. Huang et al. “High-power sub-kHz linewidth lasers fully integrated on silicon”. In: *Optica* 6.6 (June 2019), pp. 745–752. DOI: 10.1364/OPTICA.6.000745. URL: http://www.osapublishing.org/optica/abstract.cfm?URI=optica-6-6-745.

[52] Z. Huang et al. “25 Gbps low-voltage waveguide Si-Ge avalanche photodiode”. In: *Optica* 3.8 (Aug. 2016), pp. 793–798. DOI: 10.1364/OPTICA.3.000793. URL: http://www.osapublishing.org/optica/abstract.cfm?URI=optica-3-8-793.

[53] Z. Huang et al. “Low voltage high speed Si-Ge Avalanche Photodiodes”. In: *2016 21st OptoElectronics and Communications Conference (OECC) held jointly with 2016 International Conference on Photonics in Switching (PS)*. July 2016, pp. 1–3. URL: https://ieeexplore.ieee.org/document/7718302.

[54] Z. Huang et al. “Operation and analysis of low-voltage three-terminal avalanche photodiodes”. In: *2017 IEEE 14th International Conference on Group IV Photonics (GFP)*. Aug. 2017, pp. 179–180. DOI: 10.1109/GROUP4.2017.8082255.

[55] Y. Ishikawa and K. Wada. “Near-Infrared Ge Photodiodes for Si Photonics: Operation Frequency and an Approach for the Future”. In: *IEEE Photon. J.* 2.3 (June 2010), pp. 306–320. ISSN: 1943-0647. DOI: 10.1109/JPHOT.2010.2046026.

[56] Y. Ishikawa et al. “Strain-induced band gap shrinkage in Ge grown on Si substrate”. In: *Appl. Phys. Lett.* 82.13 (Jan. 2003), pp. 2044–2046. ISSN: 0003-6951. DOI: 10.1063/1.1564868. URL: https://doi.org/10.1063/1.1564868.

[57] K. Ito et al. “Waveguide-integrated vertical pin photodiodes of Ge fabricated on p^+ and n^+ Si-on-insulator layers”. In: *Japan. J. Appl. Phys.* 56.4S (Feb. 2017), 04CH05. DOI: 10.7567/jjap.56.04ch05. URL: https://doi.org/10.7567%2Fjjap.56.04ch05.

[58] P. B. Johnson and R. W. Christy. “Optical Constants of the Noble Metals”. In: *Phys. Rev. B* 6 (12 Dec. 1972), pp. 4370–4379. DOI: 10.1103/PhysRevB.6.4370. URL: https://link.aps.org/doi/10.1103/PhysRevB.6.4370.

[59] M. Jutzi et al. “Ge-on-Si vertical incidence photodiodes with 39-GHz bandwidth”. In: *IEEE Photon. Technol. Lett.* 17.7 (July 2005), pp. 1510–1512. ISSN: 1941-0174. DOI: 10.1109/LPT.2005.848546.

[60] Y. Kang et al. "Epitaxially-grown Ge/Si avalanche photodiodes for 1.3μm light detection". In: *Opt. Express* 16.13 (June 2008), pp. 9365–9371. DOI: 10.1364/OE.16.009365. URL: http://www.opticsexpress.org/abstract.cfm?URI=oe-16-13-9365.

[61] Y. Kang et al. "Ge/Si avalanche photodiodes for 1.3 μm optical fiber links". In: *2007 4th IEEE International Conference on Group IV Photonics*. Sept. 2007, pp. 1–3. DOI: 10.1109/GROUP4.2007.4347746.

[62] Y. Kang et al. "Monolithic germanium/silicon avalanche photodiodes with 340 GHz gain-bandwidth product". In: *Nature Photon.* 3.1 (Jan. 2009), pp. 59–63. ISSN: 1749-4893. URL: https://doi.org/10.1038/nphoton.2008.247.

[63] S. Keyvaninia et al. "Demonstration of a heterogeneously integrated III-V/SOI single wavelength tunable laser". In: *Optics Express* 21.3 (Feb. 2013), pp. 3784–3792. DOI: 10.1364/OE.21.003784.

[64] S. Klinger et al. "Ge on Si p-i-n photodetectors with 40 GHz bandwidth". In: *2008 5th IEEE International Conference on Group IV Photonics*. Sept. 2008, pp. 188–190. DOI: 10.1109/GROUP4.2008.4638140.

[65] S. Koeber et al. "Femtojoule electro-optic modulation using a silicon-organic hybrid device". In: *Light Sci. Appl.* 4.2 (2015), e255–e255. ISSN: 2047-7538. DOI: 10.1038/lsa.2015.28. URL: https://doi.org/10.1038/lsa.2015.28.

[66] C. Koos et al. "Silicon-Organic Hybrid (SOH) and Plasmonic-Organic Hybrid (POH) Integration". In: *Optical Fiber Communication Conference*. Optical Society of America, 2015, Tu2A.1. DOI: 10.1364/OFC.2015.Tu2A.1. URL: http://www.osapublishing.org/abstract.cfm?URI=OFC-2015-Tu2A.1.

[67] C. Koos et al. "Silicon-Organic Hybrid (SOH) and Plasmonic-Organic Hybrid (POH) Integration". In: *J. Lightwave Technol.* 34.2 (Jan. 2016), pp. 256–268. URL: http://jlt.osa.org/abstract.cfm?URI=jlt-34-2-256.

[68] M. Kummer et al. "Low energy plasma enhanced chemical vapor deposition". In: *Mater. Sci. Eng. B* 89.1 (Feb. 2002), pp. 288–295. ISSN: 0921-5107. URL: http://www.sciencedirect.com/science/article/pii/S0921510701008017.

[69] K. Q. Le and P. Bienstman. "Wide-angle beam propagation method without using slowly varying envelope approximation". In: *J. Opt. Soc. Amer. B* 26.2 (2009), pp. 353–356. DOI: 10.1364/JOSAB.26.000353.

[70] J. Leuthold et al. "Plasmonic Communications: Light on a Wire". In: *Opt. Photon. News* 24.5 (May 2013), pp. 28–35. DOI: 10.1364/OPN.24.5.000028. URL: http://www.osa-opn.org/abstract.cfm?URI=opn-24-5-28.

[71] L. Lever et al. "Design of Ge–SiGe Quantum-Confined Stark Effect Electroabsorption Heterostructures for CMOS Compatible Photonics". In: *J. Lightwave Technol.* 28.22 (Nov. 2010), pp. 3273–3281. ISSN: 1558-2213. DOI: 10.1109/JLT.2010.2081345.

[72] L. Lever et al. "Modulation of the absorption coefficient at 1.3 μm in Ge/SiGe multiple quantum well heterostructures on silicon". In: *Opt. Lett.* 36.21 (Nov. 2011), pp. 4158–4160. DOI: 10.1364/OL.36.004158. URL: http://ol.osa.org/abstract.cfm?URI=ol-36-21-4158.

[73] H. Luan et al. "High-quality Ge epilayers on Si with low threading-dislocation densities". In: *Appl. Phys. Lett.* 75.19 (Jan. 1999), pp. 2909–2911. ISSN: 0003-6951. DOI: 10.1063/1.125187. URL: https://doi.org/10.1063/1.125187.

[74] I. H. Malitson. "Interspecimen Comparison of the Refractive Index of Fused Silica∗,†". In: *J. Opt. Soc. Am.* 55.10 (Oct. 1965), pp. 1205–1209. DOI: 10.1364/JOSA.55.001205. URL: http://www.osapublishing.org/abstract.cfm?URI=josa-55-10-1205.

[75] M. Mandurrino et al. "Physics-based modeling and experimental implications of trap-assisted tunneling in InGaN/GaN light-emitting diodes". In: *Phys. Status Solidi A* 212.5 (Jan. 2015), pp. 947–953. ISSN: 1862-6300. DOI: 10.1002/pssa.201431743. URL: https://doi.org/10.1002/pssa.201431743.

[76] D. Marris-Morini et al. "Low loss 40 Gbit/s silicon modulator based on interleaved junctions and fabricated on 300 mm SOI wafers". In: *Opt. Express* 21.19 (Sept. 2013), pp. 22471–22475. URL: http://www.opticsexpress.org/abstract.cfm?URI=oe-21-19-22471.

[77] N. J. D. Martinez et al. "Characterization of high performance waveguide-coupled linear mode avalanche photodiodes". In: *2016 IEEE Optical Interconnects Conference (OI)*. May 2016, pp. 100–101. DOI: 10.1109/OIC.2016.7483029.

[78] N. J. D. Martinez et al. "High performance waveguide-coupled Ge-on-Si linear mode avalanche photodiodes". In: *Opt. Express* 24.17 (Aug. 2016), pp. 19072–19081. DOI: 10.1364/OE.24.019072. URL: http://www.opticsexpress.org/abstract.cfm?URI=oe-24-17-19072.

[79] N. J. D. Martinez et al. "Single photon detection in a waveguide-coupled Ge-on-Si lateral avalanche photodiode". In: *Opt. Express* 25.14 (July 2017), pp. 16130–16139. DOI: 10.1364/OE.25.016130. URL: http://www.opticsexpress.org/abstract.cfm?URI=oe-25-14-16130.

[80] G. Masetti, M. Severi, and S. Solmi. "Modeling of carrier mobility against carrier concentration in arsenic-, phosphorus-, and boron-doped silicon". In: *IEEE Trans. Electron Devices* 30.7 (July 1983), pp. 764–769. DOI: 10.1109/T-ED.1983.21207.

[81] A. Melikyan et al. "High-speed plasmonic phase modulators". In: *Nature Photon.* 8.3 (Mar. 2014), pp. 229–233. ISSN: 1749-4893. URL: https://doi.org/10.1038/nphoton.2014.9.

[82] A. Melikyan et al. "Plasmonic-organic hybrid (POH) modulators for OOK and BPSK signaling at 40 Gbit/s". In: *Opt. Express* 23.8 (Apr. 2015), pp. 9938–9946. URL: http://www.opticsexpress.org/abstract.cfm?URI=oe-23-8-9938.

[83] A. Messner et al. "Plasmonic Ferroelectric Modulators". In: *J. Lightwave Technol.* 37.2 (Jan. 2019), pp. 281–290. ISSN: 1558-2213. DOI: 10.1109/JLT.2018.2881332.

[84] F. Morichetti et al. "Non-Invasive On-Chip Light Observation by Contactless Waveguide Conductivity Monitoring". In: *IEEE J. Select. Topics Quantum Electron.* 20.4 (July 2014), pp. 292–301. ISSN: 1558-4542. DOI: 10.1109/JSTQE.2014.2300046.

[85] M. Morse et al. "Performance of Ge-on-Si p-i-n Photodetectors for Standard Receiver Modules". In: *IEEE Photon. Technol. Lett.* 18.23 (Dec. 2006), pp. 2442–2444. ISSN: 1941-0174. DOI: 10.1109/LPT.2006.885623.

[86] M. Nedeljkovic et al. "Mid-Infrared Silicon-on-Insulator Fourier-Transform Spectrometer Chip". In: *IEEE Photon. Technol. Lett.* 28.4 (Feb. 2016), pp. 528–531. ISSN: 1941-0174. DOI: 10.1109/LPT.2015.2496729.

[87] Y. Okuto and C. R. Crowell. "Energy-Conservation Considerations in the Characterization of Impact Ionization in Semiconductors". In: *Phys. Rev. B* 6 (8 Oct. 1972), pp. 3076–3081. DOI: 10.1103/PhysRevB.6.3076. URL: https://link.aps.org/doi/10.1103/PhysRevB.6.3076.

[88] Y. Okuto and C.R. Crowell. "Threshold energy effect on avalanche breakdown voltage in semiconductor junctions". In: *Solid-State Electron.* 18.2 (1975), pp. 161–168. ISSN: 0038-1101. DOI: https://doi.org/10.1016/0038-1101(75)90099-4. URL: http://www.sciencedirect.com/science/article/pii/0038110175900994.

[89] R. van Overstraeten and H. De Man. "Measurement of the ionization rates in diffused silicon p-n junctions". In: *Solid-State Electron.* 13.5 (1970), pp. 583–608. ISSN: 0038-1101. DOI: https://doi.org/10.1016/0038-1101(70)90139-5. URL: http://www.sciencedirect.com/science/article/pii/0038110170901395.

[90] R. Palmer et al. "High-Speed, Low Drive-Voltage Silicon-Organic Hybrid Modulator Based on a Binary-Chromophore Electro-Optic Material". In: *J. Lightwave Technol.* 32.16 (Aug. 2014), pp. 2726–2734. URL: http://jlt.osa.org/abstract.cfm?URI=jlt-32-16-2726.

[91] A. Palmieri et al. "Effect of Saturation Velocity in Germanium p-i-n Photodetectors". In: *19th Italian National Conference on Photonic Technologies (Fotonica 2017)*. IET, 2017. ISBN: 978-1-78561-757-7. DOI: 10.1049/cp.2017.0190.

[92] A. Palmieri et al. "Energy balance modeling of Ge-on-Si waveguide avalanche photodetectors". In: *Proceedings of the International Conference on Numerical Simulation of Optoelectronic Devices, NUSOD*. IEEE, 2017, pp. 211–212. ISBN: 9781509053230. DOI: 10.1109/NUSOD.2017.8010066.

[93] J.-S. Park et al. "Defect reduction of selective Ge epitaxy in trenches on Si(001) substrates using aspect ratio trapping". In: *Appl. Phys. Lett.* 90.5 (Dec. 2007), p. 052113. ISSN: 0003-6951. DOI: 10.1063/1.2435603. URL: https://doi.org/10.1063/1.2435603.

[94] F. Pavanello et al. "Broadband Digital Fourier Transform Spectrometer for On-Chip Wavelength Monitoring in the 2.3-μm Wavelength Range". In: *IEEE Photon. J.* 11.3 (June 2019), pp. 1–9. ISSN: 1943-0647. DOI: 10.1109/JPHOT.2019.2914013.

[95] R. Rodes et al. "High-Speed 1550 nm VCSEL Data Transmission Link Employing 25 GBd 4-PAM Modulation and Hard Decision Forward Error Correction". In: *J. Lightwave Technol.* 31.4 (Feb. 2013), pp. 689–695. URL: http://jlt.osa.org/abstract.cfm?URI=jlt-31-4-689.

[96] *RSoft FemSIM User Guide, v2017.03*. Synopsys, Inc., Optical Solutions Group. Ossining, NY, 2017.

[97] *RSoft FullWAVE User Guide, v2017.03*. Synopsys, Inc., Optical Solutions Group. Ossining, NY, 2017.

[98] S. Sahni, N. K. Hon, and G. Masini. "The Dual-Heterojunction Ge on Si Photodetector". In: *ECS Transactions* 64.6 (Aug. 2014), pp. 783–789. DOI: 10.1149/06406.0783ecst. URL: https://doi.org/10.1149%2F06406.0783ecst.

[99] S. A. Schelkunoff. "Generalized Telegraphist's Equations for Waveguides". In: *Bell Syst. Tech. J.* 31.4 (1952), pp. 784–801. DOI: 10.1002/j.1538-7305.1952.tb01406.x. eprint: https://onlinelibrary.wiley.com/doi/pdf/10.1002/j.1538-7305.1952.tb01406.x. URL: https://onlinelibrary.wiley.com/doi/abs/10.1002/j.1538-7305.1952.tb01406.x.

[100] *Sentaurus Device User Guide. Version N-2017.09*. Synopsys, Inc. Mountain View, CA, Sept. 2017.

[101] Y. Shen et al. "Deep learning with coherent nanophotonic circuits". In: *Nature Photon.* 11.7 (July 2017), pp. 441–446. ISSN: 1749-4893. URL: https://doi.org/10.1038/nphoton.2017.93.

[102] A. W. Snyder. "Coupling of Modes on a Tapered Dielectric Cylinder". In: *IEEE Trans. Microwave Theory Tech.* 18.7 (July 1970), pp. 383–392. ISSN: 1557-9670. DOI: 10.1109/TMTT.1970.1127247.

[103] R. Soref. "Mid-infrared photonics in silicon and germanium". In: *Nature Photon.* 4.8 (Aug. 2010), pp. 495–497. ISSN: 1749-4893. URL: https://doi.org/10.1038/nphoton.2010.171.

[104] R. Soref. "The Past, Present, and Future of Silicon Photonics". In: *IEEE J. Select. Topics Quantum Electron.* 12.6 (Nov. 2006), pp. 1678–1687. ISSN: 1558-4542. DOI: 10.1109/JSTQE.2006.883151.

[105] R. Soref and J. Larenzo. "All-silicon active and passive guided-wave components for $\lambda = 1.3$ and $1.6\,\mu$m". In: *IEEE J. Quantum Electron.* 22.6 (June 1986), pp. 873–879. ISSN: 1558-1713. DOI: 10.1109/JQE.1986.1073057.

[106] V. Sorianello et al. "Low-temperature germanium thin films on silicon". In: *Opt. Mater. Express* 1.5 (Sept. 2011), pp. 856–865. DOI: 10.1364/OME.1.000856. URL: http://www.osapublishing.org/ome/abstract.cfm?URI=ome-1-5-856.

[107] A. Spinelli and A. L. Lacaita. "Mean gain of avalanche photodiodes in a dead space model". In: *IEEE Trans. Electron Devices* 43.1 (Jan. 1996), pp. 23–30. ISSN: 1557-9646. DOI: 10.1109/16.477589.

[108] A. Spinelli, A. Pacelli, and A. L. Lacaita. "Dead space approximation for impact ionization in silicon". In: *Appl. Phys. Lett.* 69.24 (1996), pp. 3707–3709. DOI: 10.1063/1.117196. eprint: https://doi.org/10.1063/1.117196. URL: https://doi.org/10.1063/1.117196.

[109] A. Tibaldi et al. "Modeling of plasmonic organic hybrid E/O modulators: towards a comprehensive 3D simulation framework". In: *2020 European Conference on Integrated Optics (ECIO)*. June 2020.

[110] E. Timurdogan et al. "An Ultra Low Power 3D Integrated Intra-Chip Silicon Electronic-Photonic Link". In: *Optical Fiber Communication Conference Post Deadline Papers*. Optical Society of America, 2015, Th5B.8. DOI: 10.1364/OFC.2015.Th5B.8. URL: http://www.osapublishing.org/abstract.cfm?URI=OFC-2015-Th5B.8.

[111] M. Vallone et al. “Numerical Modeling of SRH and Tunneling Mechanisms in High-Operating-Temperature MWIR HgCdTe Photodetectors”. In: *J. Electron. Mater.* 44.9 (Sept. 2015), pp. 3056–3063. ISSN: 1543-186X. URL: https://doi.org/10.1007/s11664-015-3767-8.

[112] L. Virot et al. “High-performance waveguide-integrated germanium PIN photodiodes for optical communication applications [Invited]”. In: *Photon. Res.* 1.3 (Oct. 2013), pp. 140–147. DOI: 10.1364/PRJ.1.000140. URL: http://www.osapublishing.org/prj/abstract.cfm?URI=prj-1-3-140.

[113] L. Vivien et al. “42 GHz p.i.n Germanium photodetector integrated in a silicon-on-insulator waveguide”. In: *Opt. Express* 17.8 (Apr. 2009), pp. 6252–6257. DOI: 10.1364/OE.17.006252. URL: http://www.opticsexpress.org/abstract.cfm?URI=oe-17-8-6252.

[114] L. Vivien et al. “Zero-bias 40Gbit/s germanium waveguide photodetector on silicon”. In: *Opt. Express* 20.2 (Jan. 2012), pp. 1096–1101. DOI: 10.1364/OE.20.001096. URL: http://www.opticsexpress.org/abstract.cfm?URI=oe-20-2-1096.

[115] B. Wang et al. “50 Gb/s PAM4 Low-Voltage Si-Ge Avalanche Photodiode”. In: *2019 Conference on Lasers and Electro-Optics (CLEO)*. May 2019, pp. 1–2. DOI: 10.1364/CLEO_SI.2019.SM4J.7.

[116] P. O. Weigel et al. “Bonded thin film lithium niobate modulator on a silicon photonics platform exceeding 100 GHz 3-dB electrical modulation bandwidth”. In: *Opt. Express* 26.18 (Sept. 2018), pp. 23728–23739. URL: http://www.opticsexpress.org/abstract.cfm?URI=oe-26-18-23728.

[117] S. Yanikgonul et al. “2D Monte Carlo simulation of a silicon waveguide-based single-photon avalanche diode for visible wavelengths”. In: *Opt. Express* 26.12 (June 2018), pp. 15232–15246. DOI: 10.1364/OE.26.015232. URL: http://www.opticsexpress.org/abstract.cfm?URI=oe-26-12-15232.

[118] X. Zeng et al. “Low-voltage three-terminal avalanche photodiodes”. In: *Conference on Lasers and Electro-Optics (CLEO)*. Optical Society of America, 2017, SF2I.3. DOI: 10.1364/CLEO_SI.2017.SF2I.3. URL: http://www.osapublishing.org/abstract.cfm?URI=CLEO_SI-2017-SF2I.3.

[119] X. Zeng et al. “Silicon-germanium avalanche photodiodes with direct control of electric field in charge multiplication region”. In: *Optica* 6.6 (June 2019), pp. 772–777. DOI: 10.1364/OPTICA.6.000772. URL: http://www.osapublishing.org/optica/abstract.cfm?URI=optica-6-6-772.

[120] J. Zhang et al. “Transfer-printing-based integration of a III-V-on-silicon distributed feedback laser”. In: *Opt. Express* 26.7 (Apr. 2018), pp. 8821–8830. DOI: 10.1364/OE.26.008821. URL: http://www.opticsexpress.org/abstract.cfm?URI=oe-26-7-8821.

[121] Y. Zhang et al. “A high-responsivity photodetector absent metal-germanium direct contact”. In: *Opt. Express* 22.9 (May 2014), pp. 11367–11375. URL: http://www.opticsexpress.org/abstract.cfm?URI=oe-22-9-11367.

[122] S. Zhu et al. “Waveguided Ge/Si Avalanche Photodiode With Separate Vertical SEG-Ge Absorption, Lateral Si Charge, and Multiplication Configuration”. In: *IEEE Electron Device Lett.* 30.9 (Sept. 2009), pp. 934–936. ISSN: 1558-0563. DOI: 10.1109/LED.2009.2025782.

This Ph.D. thesis has been typeset by means of the TEX-system facilities. The typesetting engine was pdfLATEX. The document class was `toptesi`, by Claudio Beccari, with option `tipotesi=scudo`. This class is available in every up-to-date and complete TEX-system installation.